

SUSTAINABLE ENERGY-GENERATING PADS AS FUTURE ALTERNATIVE
ENERGY SOURCE FOR ROAD INFRASTRUCTURE

A Dissertation

by

KAZI MEHARAJUL KABIR

Submitted to the Office of Graduate Studies of
Prairie View A&M University
in partial fulfillment of the requirements for the degree of

DOCTOR OF PHILOSOPHY

August 2024

Major Subject: Electrical Engineering

SUSTAINABLE ENERGY-GENERATING PADS AS FUTURE ALTERNATIVE
ENERGY SOURCE FOR ROAD INFRASTRUCTURE

A Dissertation

by

KAZI MEHARAJUL KABIR

Submitted to the Office of Graduate Studies of
Prairie View A&M University
in partial fulfillment of the requirements for the degree of

DOCTOR OF PHILOSOPHY

Approved as to style and content by:

Annamalai Annamalai
Chair of Committee

Shuza Binzaid
Co-Chair of the Committee

Mohamed Chouikha
Member

Penrose Cofie
Member

Ziaul Huque
Member

Samir Abood
Member

Annamalai Annamalai
Head of Department (ECE)

Pamela Obiomon
Dean of College of Engineering

Tyrone Tanner
Dean of Graduate Studies

August 2024

Major Subject: Electrical Engineering

ABSTRACT

Sustainable Energy-Generating Pads as Future Alternative Energy Source for Road
Infrastructure
(August 2024)

Kazi Meharajul Kabir, Ph.D. in Electrical Engineering, Prairie View A&M University,

Chair of Advisory Committee: Dr. Annamalai Annamalai

Co-Chair of Advisory Committee: Dr. Shuza Binzaid

The world is experiencing a significant environmental crisis due to its dependence on fossil fuels for energy and transportation, which is leading to global warming and climate change. The global climate crisis demonstrates the urgent need to transition to renewable energy sources, making research on sustainable energy-generating systems increasingly important. PZT cells present an alternative energy-generating source but face challenges such as brittleness, low-frequency operation, and high-temperature sensitivity, which cause performance degradation. Additionally, issues like impedance matching and fluctuations in PZT-based energy systems contribute to significant energy generation losses. Research into composite materials, design optimizations, temperature-stabilized materials, fabrication techniques, and advanced power electronics is essential to enhance system efficiency.

This research focuses on the sustainable energy-generating pad (SEGP), which harnesses energy for lightweight vehicles like bicycles and electric bikes. The SEGP consists of multiple layers of thin-film PZT cells, energy collector circuits, and multi-composite material, effectively converting mechanical vibrations and kinetic energy into

clean electricity. Software simulations show that the first-generation SEGP (SEGP_{1X}) generates 0.59–1.35 W/ride/0.34Sec with up to 450 lbs of force applied, while the second-generation SEGP (SEGP_{2X}) produces 1.42–3.42 W/ride/0.34Sec. However, in prototype testing, SEGP_{1X} generates 0.33–0.41 W per ride, and SEGP_{2X} generates 0.54–0.67 W per ride, based on a rider and bicycle weight of approximately 160 lbs, demonstrating the potential of this technology.

Effective energy storage and collection systems are fundamental requirements for the success of any renewable energy source. To ensure stable operation and maximize energy storage, a smart dual-stage charging system (DSCS) with a round-trip efficiency of around 95% has been developed, particularly for non-sinusoidal and fluctuating energy systems. The SEGP system is integrated with existing PV technology and connected to a grid, forming a grid-tied hybrid energy microgrid system. This setup serves as a test case to evaluate the SEGP's efficiency, feasibility, and potential for real-world implementation. The generated energy can be used for water purification and e-charging, with any surplus energy sold to a utility company. A techno-economic analysis reveals a seven-year return on investment for a ten-year project, highlighting the economic viability of SEGP technology.

Index Terms – SEGP, Thin-film PZT, DSCS, Techno-economic.

DEDICATION

I dedicate the completion of this dissertation to my advisor, mentors, and professors and in loving memory to my deceased father, Kazi MD. Humayun Kabir—peace be upon him. I also extend this dedication to my mother, Mrs. Rehana Begum, and my younger sister, Kazi Farjana Yeasmin, for their boundless love, sacrifices, and unwavering support. Thank you all for being pillars of strength and encouragement throughout this journey.

ACKNOWLEDGMENTS

Firstly, I would like to express my gratitude to Almighty Allah and the people who helped and supported me in completing this dissertation and granted me the courage, strength, and determination to pursue my dream of a doctoral degree.

I sincerely thank Dr. Shuza Binzaid, Dr. John Attia (retired), Dr. Richard Wilkins (deceased), and Dr. Annamalai Annamalai for consistently sharing their spirit of adventure in research and enthusiasm for teaching. This dissertation came to fruition with their unwavering support, guidance, and valuable advice. I would also like to express my gratitude to Dr. Annamalai Annamalai, the head of the Electrical and Computer Engineering Department, and Dr. Pamela Obiomon, the dean of the College of Engineering, for fostering a conducive academic environment at Prairie View A&M University in Texas, USA.

Special thanks to Dr. John Attia for allowing me to work in the Smart Center. I am also grateful to Dr. Mohammad Chouikha, Dr. John Fuller, Dr. Penrose Cofie, Dr. Samir Abood, and Dr. Ziaul Huque for their continuous support and encouragement of this journey. All of this was only possible with the scholarship, assistance, and guidance provided by the administrative staff of the Prairie View Department of Electrical Engineering. Special thanks to the National Science Foundation (NSF) grant no. 2025641 for the funding and support to complete this research successfully. I am very grateful to all.

Finally, I express my deepest gratitude to my mother and sister for their enduring patience, love, support, encouragement, and motivation throughout this journey.

TABLE OF CONTENTS

	Page
ABSTRACT.....	III
DEDICATION.....	V
ACKNOWLEDGMENTS	VI
TABLE OF CONTENTS	VII
LIST OF FIGURES	X
LIST OF TABLES.....	XV
LIST OF ABBREVIATIONS.....	XVII
LIST OF SYMBOLS	XVIII
CHAPTER	
1. INTRODUCTION	1
1.1 Problem Statement	2
1.2 The Benefit of the Study	4
1.3 Expected Contribution.....	5
1.4 Objectives.....	6
1.5 Dissertation Organization.....	6
2. LITERATURE REVIEW	8
3. METHODOLOGY	16
3.1 Basic of PZT Cell.....	16
3.2 Present Status of PZT Technology.....	17
3.3 Present Status of Energy Storage and Collection Technology.....	22
3.4 Techno-economic Evaluation Process.....	24
4. PROPOSED SEGP SYSTEM	27
4.1 Design of a Sustainable Energy Generating Pad (SEGP) System.....	27
4.1.1 Modeling of a Sustainable Energy Generating Pad (SEGP) System.....	27
4.1.2 Theoretical Analysis of the SEGP	29
4.1.3 Simulation and Analysis of a 1X Sustainable Energy Generating Pad (SEGP _{1X}) System	33

4.1.4 Simulation and Analysis of a 2X Sustainable Energy Generating Pad (SEGP _{2X}) System	35
4.2 Design of a Dual-Stage-Charge Collection and Storage (DSCS) System	38
4.3 Summary	41
5. PROTOTYPE DEVELOPMENT & FAILURE ANALYSIS	42
5.1 Prototype AEH Model for PZT Cells Characteristics Analysis	42
5.1.1 Model for the PZT Cell Characteristics Analysis	43
5.1.2 Characteristics Analysis of 1X-Layer of PZT Cell.....	44
5.1.3 Characteristics Analysis of 2X-Layer of PZT Cell.....	45
5.1.4 Characteristics Analysis of 3X-Layer of PZT Cell.....	46
5.2 Materials Analysis for Energy Generating Pad Development	47
5.3 Prototype of a Sustainable Energy Generating Pad (SEGP) System	56
5.3.1 Prototype 1: Energy Generating Pad ₁ (EGP ₁).....	56
5.3.2 Prototype 2: Energy Generating Pad ₂ (EGP ₂).....	57
5.3.3 Prototype 3: Energy Generating Pad ₃ (EGP ₃).....	58
5.3.4 Prototype 4: Energy Generating Pad ₄ (EGP ₄).....	59
5.3.5 Prototype 5: Energy Generating Pad ₅ (EGP ₅).....	60
5.3.6 Prototype 6: Energy Generating Pad ₆ (EGP ₆).....	61
5.3.7 Prototype 7: Energy Generating Pad ₇ (EGP ₇).....	61
5.3.8 Prototype 8: Energy Generating Pad ₈ (EGP ₈).....	62
5.3.9 Prototype 9: Energy Generating Pad ₉ (EGP ₉).....	63
5.3.10 Prototype 10: Energy Generating Pad ₁₀ (EGP ₁₀).....	64
5.3.11 Prototype 11: Sustainable Energy Generating Pad ₁ (SEGP _{1X}).....	66
5.3.12 Prototype 12: Sustainable Energy Generating Pad ₂ (SEGP _{2X}).....	68
5.4 Failure Analysis of the SEGP _{1X} System.....	70
5.5 Prototype of Dual-Stage Charge Storage and Collection System	70
5.5.1 Case Study 1: Impact of Lithium-ion Batteries	71
5.5.2 Case Study 2: Impact Analysis of 18650 Lithium-ion Battery	73
5.6 Emulator Development of the SEGP System.....	73
5.6.1 Design and Simulation of SEHP Emulator.....	75
5.6.2 Prototype and Results of SEHP Emulator	78
5.7 Summary	81
6. POTENTIAL APPLICATIONS & TECHNO-ECONOMIC ANALYSIS	82
6.1 Hybrid (PV-SEGP) Grid-tie EWC Microgrid System	82
6.2 Proposed Site of the Hybrid PV-SEGP Grid-tie EWC Microgrid System.....	84
6.3 Design and Prototype of a Solar PV-Based Rainwater Purification System	85
6.4 Prototype of SEGP System.....	87
6.5 Economic Analysis of the SEGPs	87
6.6 Technoeconomic Analysis of Hybrid Grid-tie EWC Microgrid System	89
6.6.1 Technoeconomic Analysis of Islanded Microgrid-based Hybrid EWC System.....	90

6.6.2	Techonoeconomic Analysis of Grid-tie Microgrid-based Hybrid EWC System.....	100
6.7	Stability Analysis of Grid-Tie Hybrid EWC Microgrid System.....	104
6.7.1	Case Study 1: Unbalanced load flow analysis of Grid-tie EWC Microgrid System.....	110
6.7.2	Case Study 2: Voltage Stability Analysis of Grid-tie EWC Microgrid System.....	112
6.8	Summary	114
7.	RESULTS AND DISCUSSIONS.....	115
7.1	Analysis of PZT Cells Characteristics.....	115
7.1.1	The experimental outcome of the 1X-Layer of AEH	115
7.1.2	The experimental outcome of the 2X-Layer of AEH	118
7.1.3	The experimental outcome of the 3X-Layer of AEH	121
7.1.4	Comparing PZT Energy Vs. PV Energy.....	125
7.2	Analysis of Sustainable Energy Generating Pad (SEGP) System.....	127
7.2.1	Analysis of Energy Generating Pad (EGP).....	127
7.2.2	Analysis of Sustainable Energy Generating Pad ₁ (SEGP _{1X})	131
7.2.3	Analysis of Sustainable Energy Generating Pad ₂ (SEGP _{2X})	133
7.3	Analysis of Dual-Stage Charge Storage and Collection System.....	138
7.3.1	Analysis of the SEGP Connected to the Lithium Batteries	140
7.3.2	Analysis of DSCS Connected to the SEGP in Case Study 1	141
7.3.3	Analysis of DSCS Connected to the SEGP in Case Study 2	143
7.4	Projections of Energy from SEGPs for Various Locations	144
7.5	Comparison of Results	148
7.6	Summary	150
8.	CONCLUSIONS AND FUTURE WORKS.....	151
8.1	Conclusions	151
8.2	Future Works.....	153
	REFERENCES	155
	APPENDICES	167
	PHD RESEARCH OUTCOME & ACHIEVEMENTS.....	189
	CURRICULUM VITAE.....	190

LIST OF FIGURES

FIGURE	Page
Fig. 2.1 Road-Based Piezoelectric Micro-Energy System [59].	10
Fig. 2.2 Lab Experiment-Based Piezoelectric Energy Harvesting System [60].	10
Fig. 2.3 PEH System [61].	11
Fig. 2.4 Cantilever Beem PEH System [62].	11
Fig. 2.5 Thin Film PEH System [63].	11
Fig. 2.6 H. Zhang Et Al. Developed A Peh System [64].	12
Fig. 2.7 A. Sherren Et Al. Simulated A Thin Film Peh System [65].	12
Fig. 2.8 F. Guo Et Al. Developed A Piezoelectric Energy Harvesting (Peh) Shoe [66].	13
Fig. 2.9 N. Zabihi Et Al. Development In Cymbal Harvesters [67].	13
Fig. 2.10 Efficient Hybrid Energy Harvesting Systems Charging [68].	14
Fig. 2.11 A Clockless Synergistic Hybrid Energy Harvesting Technique [69].	14
Fig. 2.12 Installed PEH On The Road [70].	15
Fig. 2.13 Pehs On Road Test [71].	15
Fig. 3.1 Basic Working Principle Of PZT Cell [108].	17
Fig. 3.2 Pzt Transducers System (A) Cross-Section View (B) Top View [79].	19
Fig. 3.3 Piezoelectric Transducers Applications [80].	20
Fig. 3.5 Energy Harvesting Systems Integrate Pzt-Based Devices [82].	22
Fig. 3.6 Different Types Of Energy Storage Technologies [89].	24
Fig. 3.7 Techono-Economical Evaluation Process [93].	25
Fig. 4.1 Proposed SEGP System.	28
Fig. 4.2 Proposed Energy Collection And Storage Process in the SEGP.	28

Fig. 4.3 Equivalent Circuit Of The SEGP System.....	34
Fig. 4.4 Voltage Testing On Max Pressure Of PZT Cell Of 1X-SEGP.....	34
Fig. 4.5 Power Testing On Max Pressure Of PZT Cell Of 1X-SEGP.....	34
Fig. 4.6 Voltage Testing On Max Pressure Of PZT Cell Of 2X-SEGP.....	36
Fig. 4.7 Power Testing On Max Pressure Of PZT Cell Of 2X-SGEP.....	37
Fig. 4.8 Simulation Result Comparison For Both The SEGP.....	37
Fig. 4.9 Proposed 1x-Segp Energy Storage System.	39
Fig. 4.10 Design Of The Dual-Stage Charge Collection And Storage System.	39
Fig. 4.11 Circuit Schematic Of The DSCS System.	40
Fig. 4.12 Proposed Algorithm Of DSCS System.....	40
Fig. 5.1 The Model Of AEH (PZT Cell).....	44
Fig. 5.2 Simulation Schematic Of AEH (PZT Cell) With SCS.....	44
Fig. 5.3 Prototype Of The AEH For Thin-Film 1-Layer PZT Cell.....	45
Fig. 5.4 Prototype Of The AEH For Thin-Film Dual-Layer PZT Cell.....	46
Fig. 5.5 Prototype Of The AEH For Thin-Film Tripple-Layer PZT Cell.....	47
Fig. 5.6 Prototype Of The EGP ₁	57
Fig. 5.7 Prototype Of The EGP ₂	57
Fig. 5.8 Prototype Of The EGP ₃	58
Fig. 5.9 Prototype Of The EGP ₄	59
Fig. 5.10 Prototype Of The EGP ₅	60
Fig. 5.11 Prototype Of The EGP ₆	61
Fig. 5.12 Prototype Of The EGP ₇	62
Fig. 5.13 Prototype Of The EGP ₈	63

Fig. 5.14 Prototype Of The EGP ₉	64
Fig. 5.16 Prototype Of The SEGP _{1x}	66
Fig. 5.17 Prototype Of The SEGP _{2x}	68
Fig. 5.18 Destructive Test And Failure Analysis On The SEGP _{1x}	70
Fig. 5.19 Prototype Of Dscs System Connected With SEHPs Emulator.....	71
Fig. 5.20 The Charging Profile Of A Li-Ion Battery.	71
Fig. 5.21 Estimating The Energy Stored During The Charging Cycle Of The Li-Ion Battery.	72
Fig. 5.22 Volts/Capacity Vs. Time When Charging Lithium-Ion.	73
Fig. 5.23 Analysis Of Standard Adult Bike With Rider.	74
Fig. 5.24 The Conceptual Framework Of The SEHP Emulator.	75
Fig. 5.25 Schematic Of A SEHP Emulator.....	77
Fig. 5.26 The Output Signal Of A SEHP Emulator Like Segp.....	78
Fig. 5.27 Prototype Of SEHP Emulator.....	79
Fig. 5.28 Beginner Level The SEHP Emulator Signal Like Segp.....	79
Fig. 5.29 Intermediate Level Of The SEHP Emulator Signal Like Segp.	79
Fig. 5.30 Advanced Level The SEHP Emulator Signal Like Segp.	80
Fig. 6.1 Proposed Configuration Of The EWC System.....	83
Fig. 6.2 Proposed Project Site At PVAMU.	85
Fig. 6.3 The Prototype Portable Solar-Powered Cro Rainwater Filtration System.	87
Fig. 6.4 Comparison Of Hybrid EWC Microgrid System.	93
Fig. 6.5 Comparison Of Hybrid Grid-Tie EWC Microgrid System.	102
Fig. 6.6 Overall System's Roi Comparison.....	103

Fig. 6.7 Grid-Tie EWC Microgrid System.	110
Fig. 6.8 Analysis Of Unbalanced Load Flow Of Grid-Tie EWC Microgrid System.	111
Fig. 7.1 The 1x-Layer Of Aeh Energy Analysis (Random Sample 1).....	117
Fig. 7.2 The 1x-Layer Of Aeh Energy Analysis (Random Sample 2).....	117
Fig. 7.3 The 2x-Layer Of Aeh Energy Analysis (Random Sample 1).....	119
Fig. 7.4 The 2x-Layer Of Aeh Energy Analysis (Random Sample 2).....	120
Fig. 7.5 The 3x-Layer Of Aeh Energy Analysis (Random Sample 1).....	121
Fig. 7.6 The 3x-Layer Of Aeh Energy Analysis (Random Sample 2).....	122
Fig. 7.7 Comparison Of Aeh Layers.....	124
Fig. 7.7 Analysis Of Solar Panel.....	125
Fig. 7.8 A Three-Foot Egg ss Tested In The Lab.....	128
Fig. 7.9 The Relationship Between Speed And The Voltage Generation.	129
Fig. 7.10 The Correlation Between Speed Vs. Power Generation From The Segp.....	131
Fig. 7.11 Voltage Testing On The Prototype Of Segp _{1x}	132
Fig. 7.12 Current Testing On The Prototype Of Segp _{1x}	132
Fig. 7.13 Current Testing On The Prototype Of Segp _{2x}	133
Fig. 7.14 Voltage Testing On The Prototype Of Segp _{2x}	134
Fig. 7.15 Prototype Result Comparison For Both The Segp.	135
Fig. 7.16 Expected Power Generation Vs. No. Bike For 30 Min Riding.	138
Fig. 7.17 Expected Power Generation Vs. No. Bike For 60 Min Riding.	138
Fig. 7.18 Operational Dscs System.....	139
Fig. 7.19 Current And Voltage Operations In The Dscs Module.	140
Fig. 7.20 Average Generating Voltage From The Segp.	141

Fig. 7.21 Average Generating Current From The Segp.....	141
Fig. 7.22 Initial Voltage Of 18650 Lithium-Ion Battery.	142
Fig. 7.23 Fully Charge Of 18650 Lithium-Ion Battery.....	142
Fig. 7.24 The Mkt/Sp Rails To Trails.	145
Fig. 7.25 The Memorial Park Biking Trails.....	145
Fig. 7.26 George Bush Park.....	146
Fig. 7.27 Bike Lanes in Tamu, College Station [113].	147

LIST OF TABLES

TABLE	Page
Table 4.1 Simulation Analysis of 1X Segp.....	35
Table 4.2 Simulation Analysis of 2X Segp.....	37
Table 5.1 Materials Analysis for Developing EGP	48
Table 5.2 Glued Test Analysis on PZT And Pad Layers.....	53
Table 5.3 Experimental Analysis of The Egp ₁₀	65
Table 5.4 Experimental Analysis of The Segp _{1x}	67
Table 5.5 Experimental Analysis of The Segp _{2x}	69
Table 5.6 Sehp Generated Power Analysis Based On Speed	75
Table 5.7 Sehp Emulator Analysis.....	77
Table 5.8 Prototype SEHP Emulator Analysis	80
Table 6.1 Proposed EWC System.....	83
Table 6.2 The PV-CRO System Component Specifications	86
Table 6.3 Cost Analysis of Segps (A).....	88
Table 6.4 Cost Analysis of Segps (B).....	88
Table 6.5 Cost Analysis of Segps (C).....	88
Table 6.6 Cost Analysis of Segps (D).....	88
Table 6.7 Technical Analysis of The Ewc Microgrid System	92
Table 6.8 Economical Analysis of The Ewc Microgrid System.....	98
Table 6.9 Overall Project Analysis for Hybrid Ewc System	99
Table 6.10 Technical Analysis of The Grid-Tie Ewc System	101
Table 6.11 Economical Analysis of The Ewc Grid-Tie System.....	102

Table 6.12 Overall Analysis for Hybrid Grid-Tie Ewc System.....	104
Table 6.13 Unbalanced Load Flow Of Grid-Tie Ewc System.....	112
Table 7.1 Result Analysis of 1x-Layer Of Aeh	118
Table 7.2 Energy Generation From 1x-Layer Of AEH.	118
Table 7.3 Result Analysis of 2x-Layer Of AEH.....	120
Table 7.4 Energy Generation From 2x-Layer of AEH.	121
Table 7.5 Result Analysis of 3x-Layer Of AEH.....	123
Table 7.6 Energy Generation From 3x-Layer of AEH.	124
Table 7.7 Comparison Of Thin-Film PZT Energy VS. Pv Energy.....	126
Table 7.8 The Experimental Outcome On The Bike Lane EGP.....	128
Table 7.9 Testing Results On The Running Bike Under The EGP.	129
Table 7.10 Result Analysis Of The Segp.....	130
Table 7.11 Tested Results On The Running Segp	130
Table 7.12 Prototype Testing Analysis Of Segp _{1x}	132
Table 7.13 Prototype Analysis Of Segp _{2x}	134
Table 7.14 Expected Generation Analysis from SEGPs.....	135
Table 7.15 Expected Generation on Different Areas from SEGPs.....	147

LIST OF ABBREVIATIONS

Abbreviation	Description
EGP	Energy Generating Pad
SEGP	Sustainable Energy Generating Pad
DSCS	Dual-Stage Charging System
SEHP	Sustainable Energy Harvesting Pad
NSF	National Science Foundation
EWC	Energy, Water, and e-Charging
PEH	Piezoelectric Energy Harvesting
PZT	Lead Zirconate Titanate
PV	Photovoltaic
RO	Reverse Osmosis
HVDC	High Voltage Direct Current
IEEE	Institute of Electrical and Electronics Engineers
CVD	Chemical Vapor Deposition
LPT	Low-Pressure Transfer
ROI	Return on Investment
OPF	Optimal Power Flow
PENGs	Piezoelectric Nanogenerators
AEH	Alternative Energy Harvesting
SCS	Smart Charging System

LIST OF SYMBOLS

Symbol	Description
EGP_1	Sample Pad 1 of EGP
EGP_2	Sample Pad 2 of EGP
EGP_3	Sample Pad 3 of EGP
EGP_4	Sample Pad 4 of EGP
EGP_5	Sample Pad 5 of EGP
EGP_6	Sample Pad 6 of EGP
EGP_7	Sample Pad 7 of EGP
EGP_8	Sample Pad 8 of EGP
EGP_9	Sample Pad 9 of EGP
EGP_{10}	Sample Pad 10 of EGP
$SEGP_{1X}$	Sample Pad 1X-Layer of SEGP
$SEGP_{2X}$	Sample Pad 2X-Layer of SEGP
$SEGP_{HV}$	Sustainable Energy-Generating Pad for Heavy Vehicles
$SEHP$	Emulator of SEGP

CHAPTER 1

INTRODUCTION

In a world grappling with escalating energy demands fueled by technological advancements and evolving consumer needs, the imperative for sustainable and renewable energy solutions has never been more pressing [1]-[2]. The quest for alternatives to fossil fuels, notorious for their adverse environmental effects and geopolitical challenges, has steered global initiatives towards embracing a green and renewable energy future [3]-[4]. Solar, wind, and biomass have gained prominence among the myriad renewable options. However, the potential of piezoelectric energy, particularly harnessed through thin-film lead zirconate titanate (PZT) cells, emerges as a promising contender in the pursuit of clean and efficient energy generation [5]-[7].

The foundational principle of piezoelectric energy involves the conversion of mechanical force into electrical charges, a phenomenon crucially employed in thin-film PZT [8]-[10]. Innovative solutions become paramount as countries worldwide commit to a sustainable future, aiming to transition from conventional to renewable energy sources within 30 years [11]-[12]. A visionary blueprint encompassing diverse energy sources, smart technologies, and traditional power grids is a guiding principle toward a sustainable energy ecosystem [13]-[14]. Within this comprehensive approach, PZT cells stand out as an alternative, boasting higher energy density and specific pressure tolerance properties [15]-[16]. Thin-film PZT, with its unique properties, offers a resilient and efficient method

for power generation, opening avenues for developing novel energy-producing technologies [17]-[18].

Ongoing research and development endeavors are dedicated to harnessing the full potential of PZT energy, marking a new frontier in sustainable energy solutions [19]-[21]. The development of the SEGP, harnessing the piezoelectric effect for lightweight vehicles, signifies a revolutionary stride towards sustainable and eco-friendly transportation [22]-[25]. The efficient conversion of mechanical vibrations and kinetic energy into clean and renewable electricity provides a promising avenue for reducing the environmental footprint of transportation [26]-[29]. Additional studies on The SEGP system's integration with existing solar photovoltaic (PV) technology and its connection to a grid, forming a grid-tie hybrid energy microgrid system, enhance efficiency, feasibility, and real-world implementation potential. Microgrid stability maintains a consistent energy supply and demand balance [30]-[36].

This research envisions a future where PZT-based energy generation, integrated Smart Charging (DSCS) system for road infrastructure, and sustainable transportation converge to create a cleaner, smarter, and more environmentally conscious global landscape. Pursuing sustainable energy solutions through innovative technologies is necessary and a collective responsibility to pave the way for greener and more sustainable future. This study contributes to this joint effort by extending the boundaries of what is feasible in SEGP energy.

1.1 Problem Statement

The problems addressed in this research were:

The imperative for sustainable and renewable energy solutions has become increasingly urgent in a rapidly evolving world characterized by escalating energy demands and growing environmental concerns. Fossil fuels, the backbone of traditional energy systems, are finite resources and contribute significantly to environmental degradation and geopolitical instability. As nations worldwide commit to mitigating these challenges and transitioning towards greener energy sources, innovative approaches are required to address these situations.

The existing renewable energy landscape, primarily comprised of solar, wind, and biomass technologies, has made significant strides in recent years. However, challenges persist, particularly in urban environments where space constraints and infrastructure limitations pose barriers to widespread adoption. Moreover, the intermittent nature of renewable energy sources necessitates efficient storage and distribution systems to ensure a reliable and consistent power supply.

In this context, piezoelectric energy, harnessed through thin-film lead zirconate titanate (PZT) cells, emerges as a promising yet underexplored avenue for clean and efficient energy generation. The unique ability of PZT cells to convert mechanical force into electrical charges presents an opportunity to harness energy from everyday activities, such as pedestrian movement and vehicular traffic. However, it also has some implications, such as materials, design optimizations, temperature-stabilized materials, advanced fabrication techniques, and improved power electronics and storage devices that contribute to energy generation losses. By overcoming those issues, a PZT-based energy-generating system could be a great alternative energy source.

One innovative application is the development of a Sustainable Energy Generating Pad (SEGP) for roads, which can be a potential solution to address all issues. This SEGP, composed of multiple layers featuring thin-film PZT cells, captures mechanical bending stress energy from passing lightweight vehicles, such as bicycles, on dedicated lanes. Simulations indicate significant potential for energy generation, with real-world prototype implementations demonstrating promising results.

Additionally, integrating SEGP technology into road infrastructure offers a unique opportunity to revolutionize urban transportation systems. By establishing SEGP with existing PV technology, combined hybrid energy, water, and e-bike charging (EWC) stations along roadways can be an additional solution to energy, water, and transportation needs. These integrated stations provide renewable energy generation, water production, and electric vehicle charging facilities, promoting sustainable mobility and reducing reliance on fossil fuels.

Despite the immense potential of SEGP systems, several challenges must be addressed to facilitate widespread adoption. These include technological optimization, cost-effectiveness, regulatory frameworks, and public acceptance. Moreover, interdisciplinary collaboration between researchers, engineers, urban planners, policymakers, and stakeholders is essential to ensure the successful implementation and integration of these innovative solutions into existing road infrastructure.

1.2 The Benefit of the Study

This research presents an exhaustive investigation into developing and implementing SEGP technologies within road infrastructure with diverse domains,

including renewable energy, materials science, power electronics, and microgrid systems. The study adopts an interdisciplinary approach.

Innovative solutions such as SEGP and Dual-Stage Charge Collection and Storage (DSCS) systems represent novel contributions to addressing critical issues concerning energy generation, energy storage, and future electric vehicle charging infrastructure. The prototype development and failure analysis processes provide valuable insight into the SEGP system. The additional work on the SEGP combined with the existing PV system also provides valuable insights into its viability, stability, cost-effectiveness, and potential benefits for real-world application implementations.

1.3 Expected Contribution

This research aspires to contribute to a new alternative sustainable energy generation approach with power electronics devices for efficient energy storage. The primary focus is on a novel SEGP system that integrates SEGP technologies with Dual-Stage Charging Systems (DSCS) for road infrastructure, pioneering innovative approaches to address alternative energy and energy storage for the energy and transportation sectors. These contributions span from design and simulations to experimental validations and failure analyses.

Novel technologies like SEGP and DSCS systems are developed to make seminal strides toward harnessing clean energy sources and smart energy storage to enhance efficiency and tackle pressing environmental and green energy production challenges. Case studies for various locations of potential areas of Houston and techno-economic analysis are conducted to determine its potential energy generation, feasibility, cost-effectiveness,

and potential socio-economic benefits. This analysis helped to determine its potential to implement this SEGP technology in the real world.

1.4 Objectives

The objectives of this study are:

- Develop a novel sustainable energy generating pad (SEGP) as an alternative energy source utilizing a thin-film PZT cell.
- Develop and prototype a dual-stage smart energy storage system for efficient energy management for SEGP and lower energy generation systems.
- Develop an emulator of this innovative new technology for students, academicians, researchers, and investors for learning and training purposes.
- Perform techno-economical analyses to determine the Return on Investment (ROI) and make the system economical and convenient.

1.5 Dissertation Organization

The dissertation is organized into eight chapters, as follows:

The study started with an Introduction in Chapter 1 explaining the problem, its importance, and the research goals. It also outlined the benefits of the study and the contributions it aimed to make. Chapter 2 focuses on the Literature Review, providing a detailed overview of previous research related to this research. Chapter 3 discusses the Methodology of the basics of PZT cells, the current technology status and methods for the PZT-based system, energy storage and collection, and an economic evaluation process. Chapter 4 discusses the design and simulation of the proposed SEGP system, including theoretical analysis and simulations for the SEGP system. Chapter 5 covers prototype development and failure analysis, detailing the creation, modification, and testing of different prototypes and their

failures. Chapter 6 looks at the proposed system's potential applications and economic aspects, including hybrid systems combining PV and SEGP technologies and a case study on a possible location to determine these systems' stability and financial feasibility. The Results and Discussions in Chapter 7 discuss the findings in detail, discussing the performance of PZT cells, the SEGP system, and the dual-stage charge storage and collection systems. Finally, the Conclusions and Future Works chapter in Chapter 8 summarizes the study's contributions and outcomes and suggests directions for future research.

CHAPTER 2

LITERATURE REVIEW

In recent years, Piezoelectric Energy Harvesting (PEH) has garnered significant interest as a sustainable solution for generating electricity from mechanical energy, particularly in roadway applications. This review aims to analyze recent advancements in PEH, exploring various sources of piezoelectric energy, feasibility studies, research on roadway PEH systems, comparative analysis, evaluation systems, and cost analysis. Piezoelectric energy can be harvested from diverse sources such as pedestrian movement, footwear vibrations, and vehicular motion [37]-[38]. Notably, Innowattech's pioneering work in developing the first pavement power generation system using piezoelectric technology marked a significant milestone in the field [39]. Feasibility studies have explored the practical applications of piezoelectric sensors in traffic monitoring, tire friction estimation, and vehicle weight measurement [40]-[41]. Additionally, efforts have been made to store vibrational piezoelectric energy for broader sustainable energy applications [42]-[43].

Recent research has focused on embedding piezoelectric modules into roadways to generate electricity, with various designs proposed, including cymbal, pile, stack, and cantilever-based systems [44]-[45]. Recent studies have reported promising results [46]-[71]. Sun et al. developed a simulated piezoelectric unit capable of harvesting 1.785 MW from asphalt concrete pavement [46]. Song et al. designed a PZT-PZNM ceramic PEH that generated 4.91 Wh/m² under typical traffic conditions [47]. Gareh et al. evaluated an APC piezoelectric ceramic cymbal transducer capable of producing 170 kW/km when laid

across a highway [48]. Xiong et al. installed PEHs along US Interstate 81 and reported a transmission efficiency of 14.43 % of mechanical energy from vehicles [49]. Yang et al. designed a PEH for wireless sensor network power supply, achieving a maximum output power of 21.47 W/m² [50]. Shin et al. tested a high-power PVDF-based PEH on Korean highways, generating up to 16 W/m² [51]. Studies have compared various PEH designs, highlighting differences in energy conversion efficiencies and applicability [52]-[53]. Vehicle speed, weight, and environmental temperature significantly impact PEH performance [54]-[55]. Efforts have been made to develop evaluation systems and cost analysis metrics to assess PEH viability and cost-effectiveness [56]-[57]. Papagiannakis et al. estimated LCOE values between \$19 and \$4.8/kWh depending on traffic conditions, indicating the economic feasibility of PEH [58].

C. Wang et al. developed an energy harvesting system that collects power with noticeable effects. The output power ranges from 13.52 to 35.04 mW when subjected to the weight of a randomly selected car, as shown in Fig. 2.1 [59]. A. Jasim et al. developed a laboratory-based piezoelectric energy harvester (PEH) system used in the module with a resistive load of 400 k Ω , as shown in Fig. 2.2. The power outputs of the energy harvester module varied between 26.6 and 30.1 mW under a loading stress of 0.7 MPa at 5 Hz [60]. C. Wang et al. developed another PEH system, as shown in Fig. 2.3 [61], and the optimized piezoelectric device can produce a maximum terminal voltage of 37.6 V and a maximum average output power of 10.036 mW.

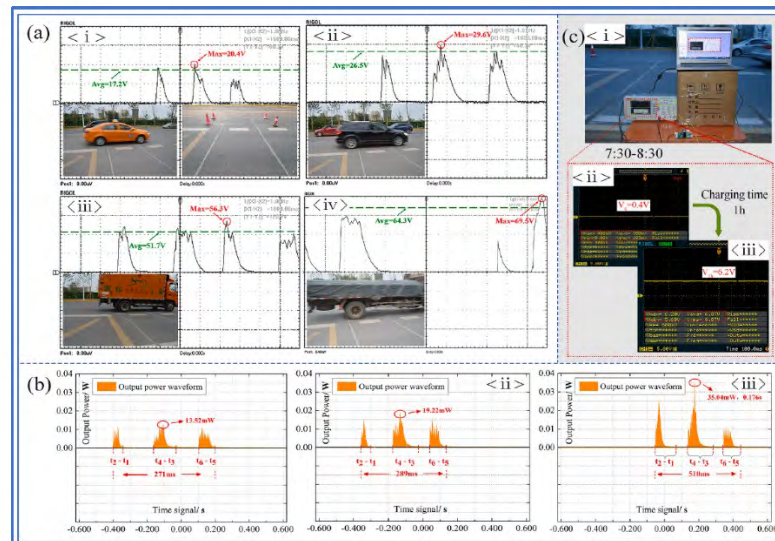


Fig. 2.1 Road-based Piezoelectric Micro-Energy System [59].

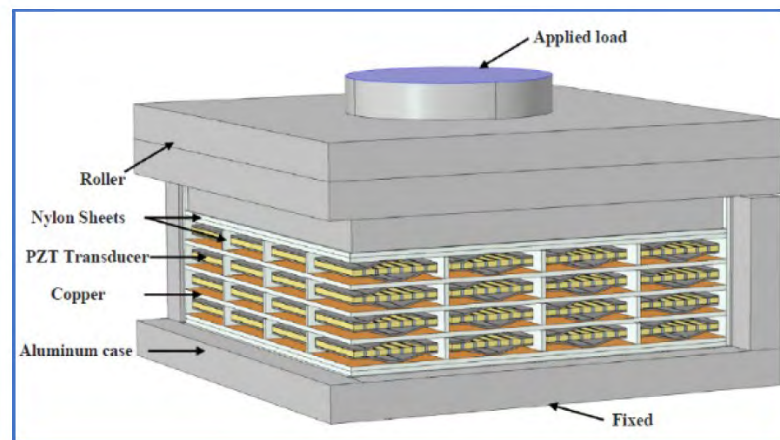


Fig. 2.2 Lab Experiment-based Piezoelectric Energy Harvesting System [60].

B. Lafarge et al. developed a PEH system that activates when a car crosses tramway rails at a speed of 50 km/h. One can clearly observe significant vibrations occurring at $t = 15$ s, resulting in a harvested power peak of 1.97 mW, as shown in Fig. 2.4 [62]. A. Mahajan et al. developed a thin film PEH system, as shown in Fig. 2.5 [63]. The power output of 3.14 mW (under an output voltage of 5.2 V and power density of 0.0063 mW/mm^3) is apparently higher than that of other harvesting mechanisms. H. Zhang et al. developed a PEH system, as shown in Fig. 2.6 [64], where the effective voltage increases with the

overall electrical resistive load and gradually tends to saturate at 16.5 V when the electrical resistance (R_E) is approximately 45 M Ω for an embedded depth of $d = 10$ mm. The peak power value is 1.8 μ W.

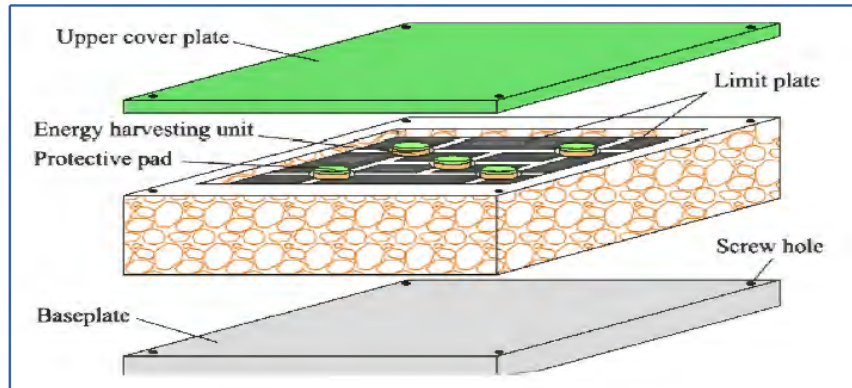


Fig. 2.3 PEH System [61].

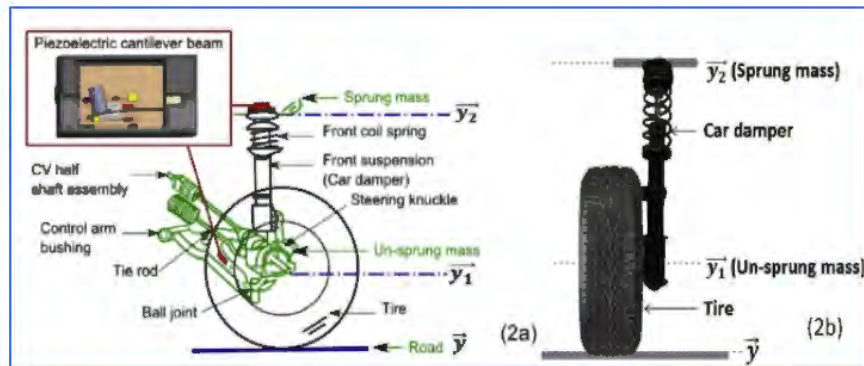


Fig. 2.4 Cantilever Beam PEH System [62].

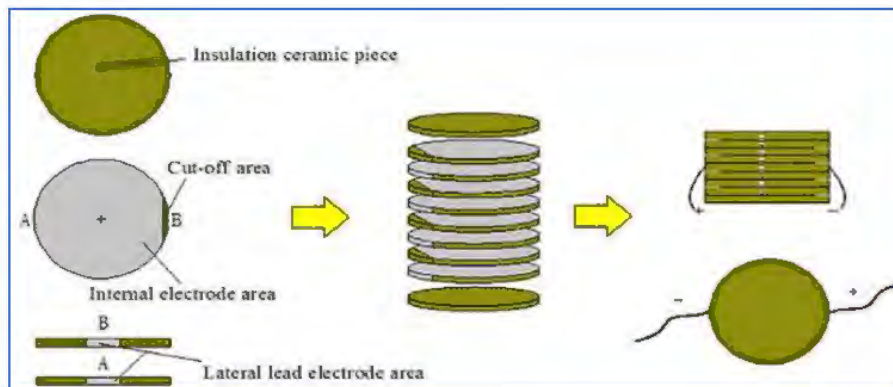


Fig. 2.5 Thin Film PEH System [63].

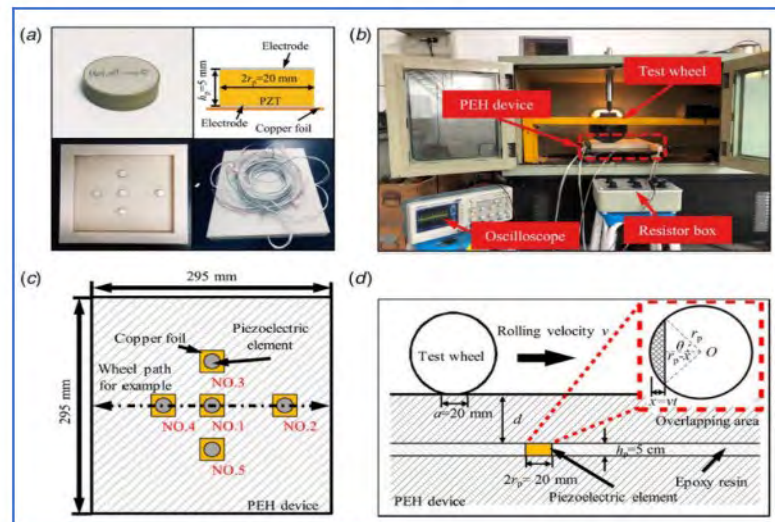


Fig. 2.6 H. Zhang et al. developed a PEH System [64].

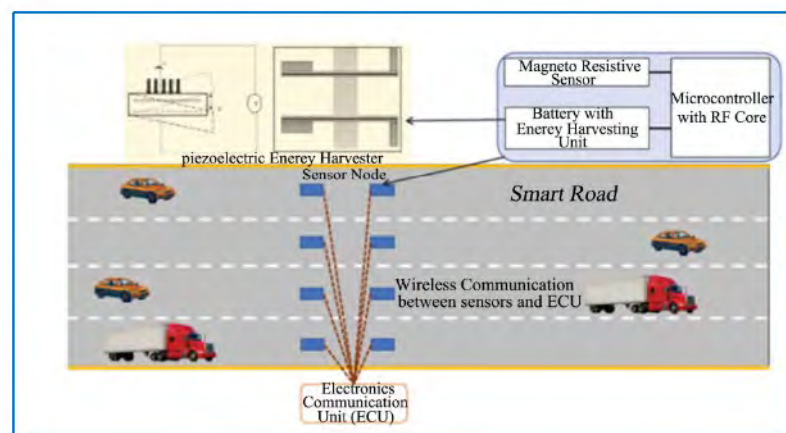


Fig. 2.7 A. Sherren et al. simulated a thin film PEH system [65].

A. Sherren et al. simulated a thin film PEH system for a car, and the power output ranged from 0.2 to 0.4 W, as shown in Fig. 2.7 [65]. F. Guo et al. developed a piezoelectric energy harvesting (PEH) shoe with an effective average voltage of 1.5 V when subjected to finger tapping, as shown in Fig. 2.8 [66]. N. Zabihi recently investigated another development in cymbal harvesters, focusing on its performance under frequencies lower than 30 Hz. An open circuit (OC) power output of nearly 0.2 mW was obtained from the harvester under a load of 500 N and a frequency of 20 Hz, as shown in Fig. 2.9 [67]. I.C.

Chen et al. developed a single-inductor dual-input dual-output (SI-DIDO) DC-DC converter, as shown in Fig. 2.10 [68], for efficient photovoltaic and piezoelectric energy harvesting systems charging.



Fig. 2.8 F. Guo et al. developed a piezoelectric energy harvesting (PEH) shoe [66].



Fig. 2.9 N. Zabihi et al. development in cymbal harvesters [67].

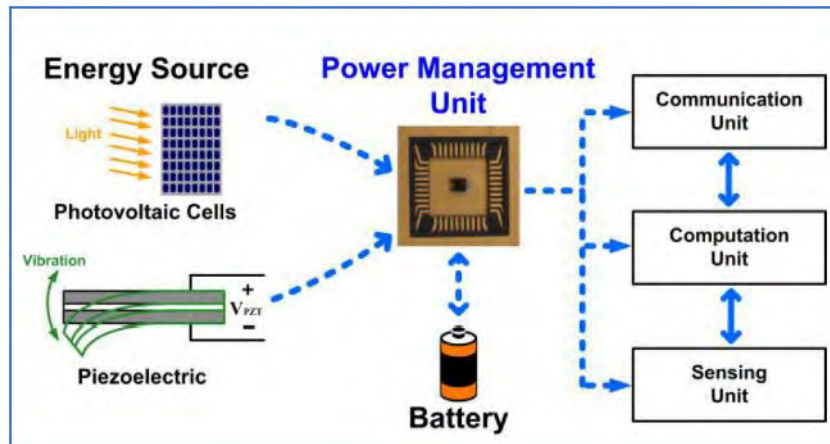


Fig. 2.10 Efficient Hybrid Energy Harvesting Systems Charging [68].

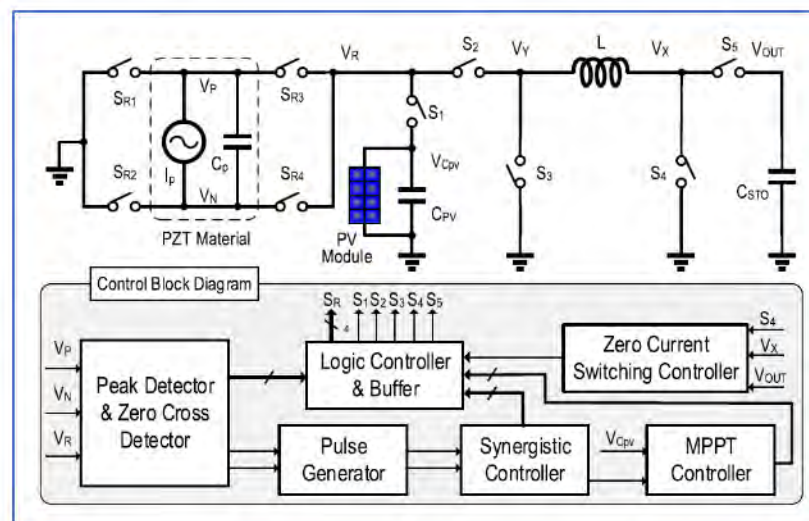


Fig. 2.11 A clockless synergistic hybrid energy harvesting technique [69].

X. Wang et al. developed a clockless synergistic hybrid energy harvesting technique with simultaneous energy injection and sampling for piezoelectric and photovoltaic energy, as shown in Fig. 2.11 [69]. Another prominent research study by H. Xiong et al. on electrical energy generated from piezoelectric energy harvesters (PEHs) is highly relevant to single-axle loading of vehicles, where the average power output strongly depends on the total axle loading. The system is shown in Fig. 2.12 [70]. The average power output of the installed PEH is 3.106 mW. C. Chen et al. reported the representative

open-circuit voltage generated on both sides during a road test at a speed of approximately 40 km/h. The system is shown in Fig. 2.13 [71]. The PEHs produced an open-circuit electric with the maximum voltage observed reaching 484 V and the cumulative energy of 20.29 J.

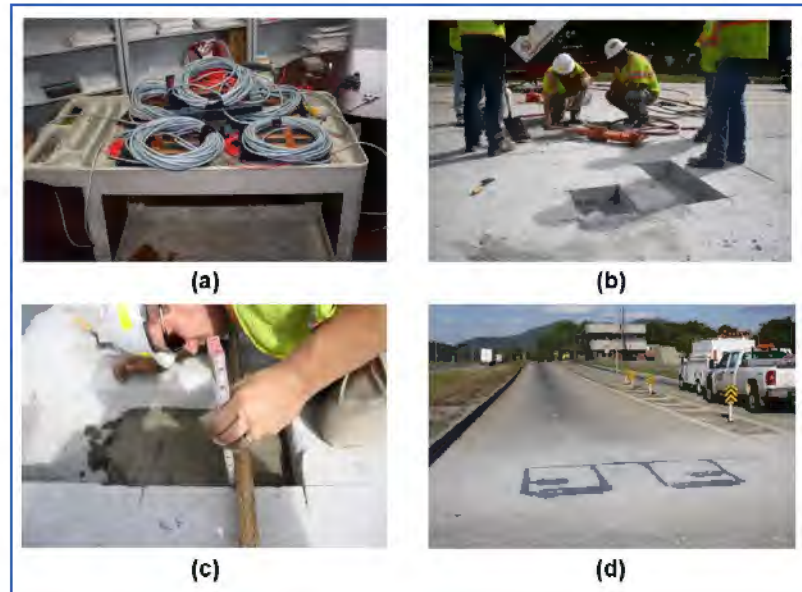


Fig. 2.12 Installed PEH on the Road [70].



Fig. 2.13 PEHS on Road Test [71].

CHAPTER 3

METHODOLOGY

Renewable or Alternative energy technologies have transformed the global energy sector, offering sustainable alternatives to fossil fuels. Piezoelectric materials like lead zirconate titanate (PZT) are gaining traction for energy harvesting applications, promising decentralized and renewable power sources, integrating PZT and battery storage systems, providing resilient energy solutions, enhancing grid stability, and promoting energy independence. Battery storage and charger controller systems are pivotal in optimizing maximum energy efficiency.

3.1 Basic of PZT Cell

PZT is a piezoelectric material, which means it can generate an electric charge in response to mechanical stress (like pressure or vibrations) and vice versa (generate mechanical stress when an electric field is applied), as shown in Fig. 3.1 [108]. It is commonly used in sensors, actuators, transducers, and various electromechanical devices. Working principle: When mechanical stress is applied to PZT, it causes a displacement of positive and negative ions within the material, leading to the generation of an electric potential difference or voltage across its surfaces. This phenomenon is known as the piezoelectric effect.

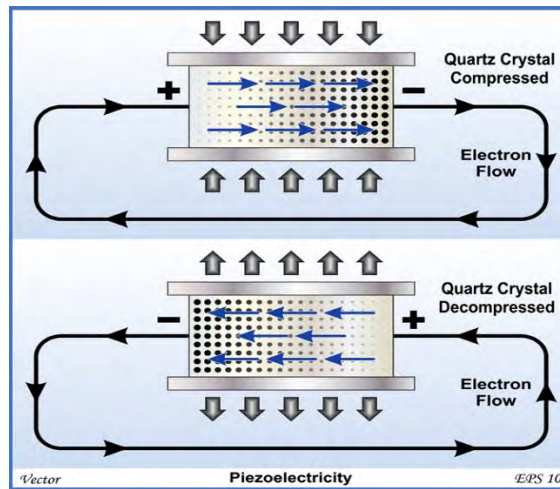


Fig. 3.1 Basic Working Principle of PZT Cell [108].

3.2 Present Status of PZT Technology

Lead zirconate titanate (PZT) technology plays a significant role in the field of energy harvesting, particularly in converting mechanical vibrations or movements into electrical energy. Here is an overview of the present status of PZT technology, including its operation, working principle, energy harvesting status, and types of PZT-based energy harvesting devices [76]-[78]: The development of lead zirconate titanate (PZT) materials and thin-film PZT cells for energy harvesting has seen advancements, though not as extensively documented or as mainstream as solar cell technology. Nonetheless, here is a general overview of the progress in this field:

Early Research (Before 2000): research on PZT materials and their potential for energy harvesting begins. However, efficiency levels are generally low, and practical applications are limited.

2000s: research efforts focus on improving the efficiency and manufacturability of PZT-based energy harvesting devices. Thin-film deposition techniques were explored to

create PZT layers with controlled properties. 2010s: advancements in thin-film deposition technologies, such as chemical vapor deposition (CVD) and sputtering, enabled better control over the properties of PZT films. Efforts were made to optimize the crystal structure, composition, and processing conditions to enhance energy harvesting performance. 2015: Researchers achieved notable improvements in the efficiency of thin-film PZT energy harvesting devices, with some prototypes demonstrating conversion efficiencies exceeding 10%. 2017: further advancements led to the development of PZT-based energy harvesters with improved power output and broader frequency bandwidth, making them suitable for a wider range of applications. 2020s: research continues to focus on enhancing the performance, reliability, and scalability of thin-film PZT energy harvesters. Efforts are made to address challenges such as material degradation, mechanical robustness, and compatibility with target applications.

Energy Harvesting Status:

PZT-based energy harvesting has seen significant advancements and applications in recent years. It is used in various sectors, such as aerospace, automotive, industrial machinery, wearable devices, and structural health monitoring systems. The technology has proven effective in capturing ambient mechanical energy and converting it into usable electrical power, contributing to the development of self-powered and energy-efficient systems. These advancements focus on enhancing material properties, optimizing device architectures, and integrating systems to maximize energy output under varying conditions. As a result, PZT-based energy harvesters are increasingly being tailored for specific applications, ranging from wearable electronics to large-scale industrial systems, demonstrating significant potential for sustainable energy solutions.

Types of PZT-Based Energy Harvesting Devices:

- a. **Piezoelectric Transducers:** piezoelectric transducers convert mechanical energy into electrical energy and vice versa, relying on the piezoelectric effect exhibited by certain materials like quartz, ceramics, and some biological substances. When subjected to mechanical stress or vibrations, these materials generate electrical charges across their surfaces, which can be harnessed for various applications such as sensors, actuators, and energy harvesting systems. The PZT transducer system is shown in Fig. 3.2.

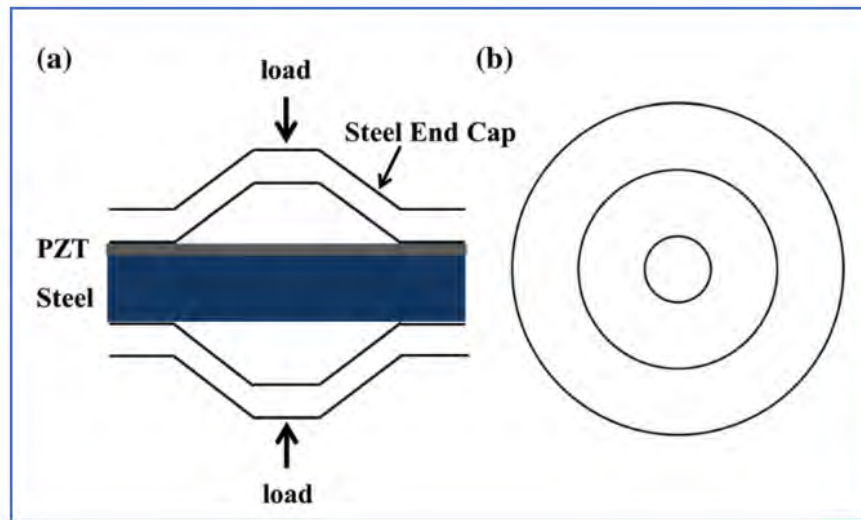


Fig. 3.2 PZT Transducers System (a) Cross-section View (b) Top View [79].

- b. **Piezoelectric Sensors:** piezoelectric sensors find extensive applications in measuring minute forces and strains, particularly in dynamic environments involving vibrations, accelerations, and oscillations. These sensors operate by repositioning the crystalline bulk dipole density, also known as the polarization vector, in response to applied stress, resulting in an effective charge density on the crystal surface, thereby generating an electrical signal. A common conceptual

model for piezoelectric sensors is that of a capacitor connected in parallel with a current source, where the output typically represents the derivative of the charge produced. This charge output is commonly amplified, leading to a voltage output proportional to the captured charge. Notably, piezoelectric sensors are categorized as 'active' sensors, eliminating the need for external power sources and mitigating potential heating concerns often associated with 'passive' piezoresistive sensors. Some applications of the piezoelectric sensors are shown in Fig. 3.3. The sensors are often integrated into structures or machinery to monitor performance while simultaneously harvesting energy.

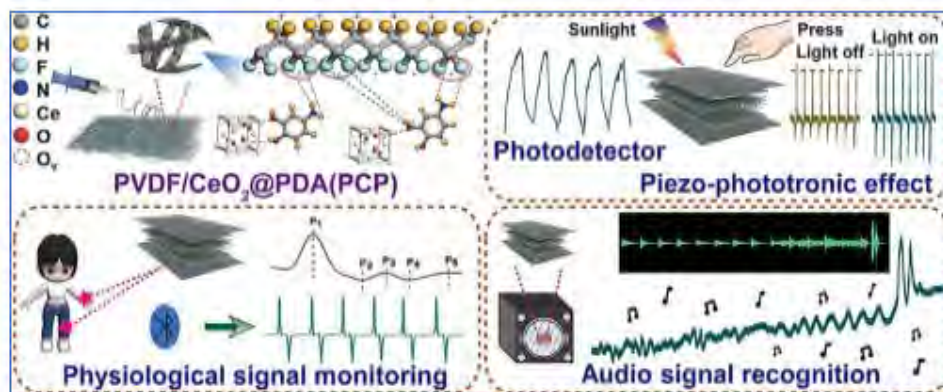


Fig. 3.3 Piezoelectric Transducers applications [80].

- c. Piezoelectric Nanogenerators (PENGs): the concept and design principles of the Magneto-Mechanical Piezoelectric Nanogenerator (MM-PENG) is integrated to modify its mechanical behavior, with plans to grow a piezoelectric layer on these MM components. The design and concept of the MMPENG are shown in Fig. 3.4, where the piezo-MM plates are firmly held within the rigid MM-PENG container using top and bottom fixtures. These plates are strategically positioned between bilateral constraints that allow unhindered longitudinal movement. Under axial

excitations, the container induces inertia in the sliding cell, causing buckling instability in the plates. The bilateral constraints then facilitate post-buckling snap-through in the piezo-MM plates, enabling transitions in buckling modes to activate the piezoelectric layer for electrical power generation.

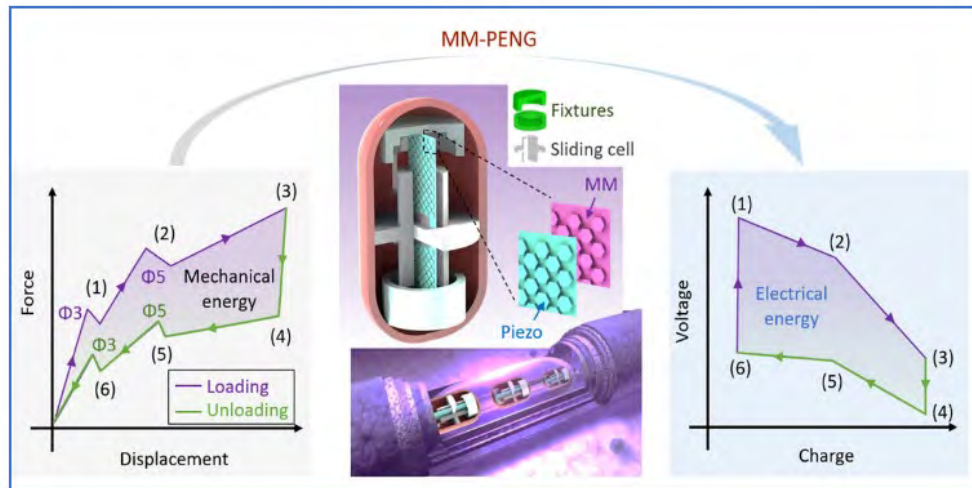


Fig. 3.4 Design, Processes, and Conversion of the MM-PENG. [81].

- d. **Integrated PZT Systems:** technologies designed to harvest energy from vehicle traffic on streets can also be used to capture energy from human movement. Key energy sources for these applications include solar radiation, environmental heat, mechanical stress, wind, and vehicle vibrations. Vibrations and mechanical stress are particularly effective as they can be tapped using electromagnetic, piezoelectric, and triboelectric technologies. Solar and geothermal energy systems primarily depend on solar radiation and heat. An integrated PZT-based system is shown in Fig. 3.5. The system generally consists of three key components: the transducer, an electric circuit, and a load. The transducer's role is to convert the energy source into electrical power; the circuit then regulates this electricity, and the load utilizes it. The harvested energy can be used for various applications, such as powering

streetlights, traffic devices, and in situ sensors like accelerometers, displacement sensors, force sensors, resistance strain gauges, optical fibers, and structural health monitoring systems. Furthermore, this energy can be used to protect road surfaces from ice and heat. The energy generated can differ based on the energy harvesting circuit used. Ongoing research focuses on optimizing energy conversion efficiency, increasing power output, and enhancing the durability and performance of PZT-based energy harvesting devices.

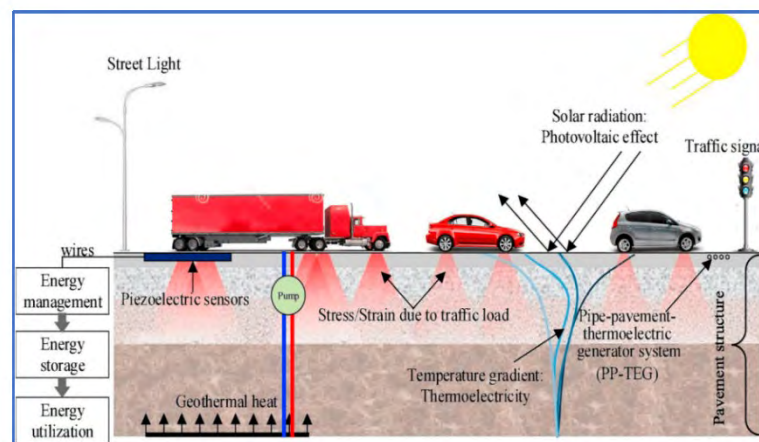


Fig. 3.5 Energy harvesting systems integrate PZT-based devices [82].

3.3 Present Status of Energy Storage and Collection Technology

Efficiency and performance improvements for energy storage and charge controller technologies [85]-[88]: from the 1950s to the 1960s, lead-acid batteries had an efficiency of around 70%, with significant energy losses during charging and discharging cycles. These batteries were relatively affordable compared to other options. Charge controllers during this period had an efficiency of about 50%, primarily regulating charging voltages and preventing overcharging. They were cost-effective but basic in functionality.

In the 1970s to 1980s, lead-acid battery efficiency slightly improved but remained around 70%. The costs of these batteries stayed relatively low, making them a common choice for energy storage. Charge controllers saw an efficiency increase to around 60%, with a slight rise in cost due to added features such as temperature compensation.

From the 1990s to the 2000s, lead-acid batteries maintained an efficiency of around 70%, with modest improvements in cycle life. They continued to be low-cost compared to newer battery technologies. Nickel-metal hydride (NiMH) batteries, introduced during this period, offered higher efficiency than lead-acid batteries but came with higher costs due to their improved performance. Lithium-ion batteries emerged with an efficiency of around 90%, although they were significantly more expensive initially due to advanced technology and materials. Charge controllers' efficiency increased to around 80%, with costs rising accordingly due to enhanced features and capabilities.

In the 2010s, lithium-ion battery efficiency further improved to around 95%, with costs gradually decreasing as manufacturing processes matured and economies of scale were achieved. Charge controllers reached an efficiency of around 90%, with costs remaining relatively stable as advanced features became more standardized. These improvements made lithium-ion batteries a more attractive option for a wider range of applications, including electric vehicles and renewable energy storage. As a result, the adoption of these technologies accelerated, driving further innovation and contributing to the global shift towards more sustainable energy solutions.

In the 2020s, lithium-ion batteries have maintained an efficiency of around 95%, with costs continuing to decrease due to technological advancements, increased production volumes, and market competition. Charge controllers during this period have maintained

an efficiency of about 90%, with costs staying relatively stable as demand for renewable energy systems grows and production scales up. While newer energy storage and charge controller technologies may initially have higher costs than traditional options, ongoing advancements and economies of scale drive down prices, making them increasingly competitive in the market. These cost reductions and improved efficiency and performance contribute to the widespread adoption of renewable energy systems. Different types of energy storage are shown in Fig. 3.6.

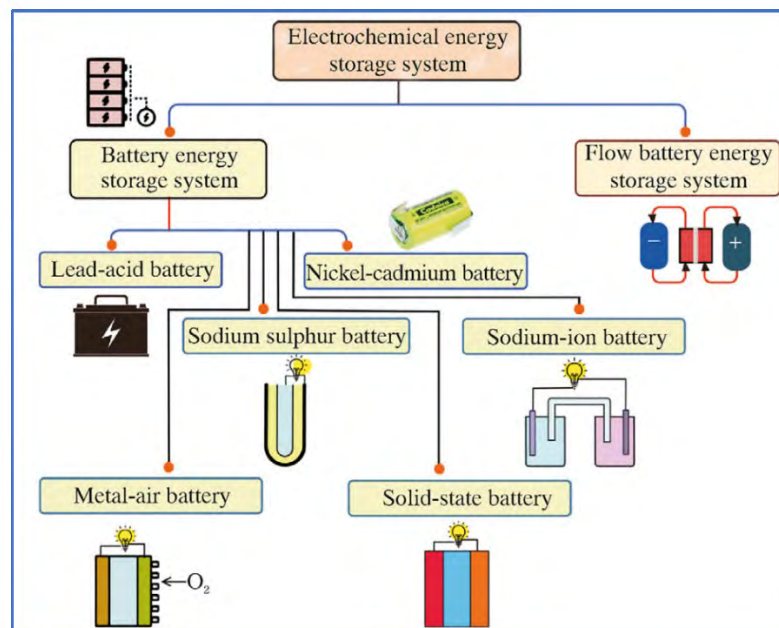


Fig. 3.6 Different Types of Energy Storage Technologies [89].

3.4 Techno-economic Evaluation Process

The techno-economic evaluation process follows a structured sequence of steps to comprehensively assess a renewable energy project's feasibility and economic viability, as shown in Fig. 3.7. Here is an outline of the procedure, along with key evaluation criteria and details [90]-[92]:

Project Definition and Scope: define the objectives, scope, and key performance indicators (KPIs). Identify the renewable energy technology: solar PV, wind, biomass, and project location.

Resource Assessment: conduct a thorough assessment of renewable energy resources available at the project site, that is, solar irradiance, wind speed, biomass, SEGP, quantities of running bike availability. Utilize data from meteorological stations, satellite imagery, and other sources to characterize resource availability.

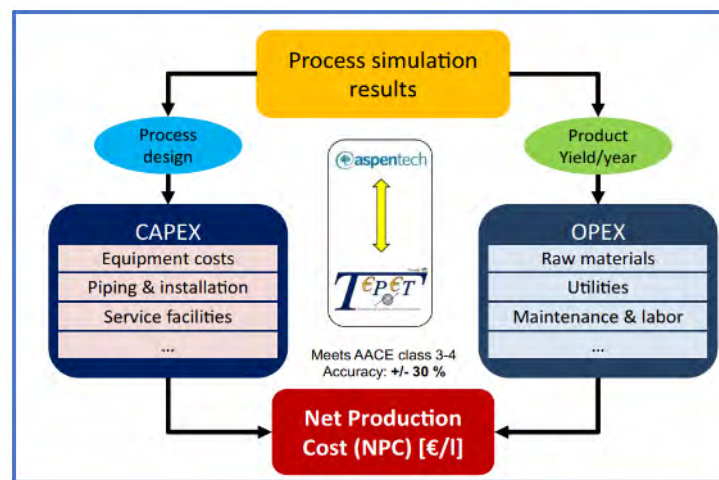


Fig. 3.7 Techno-economical Evaluation Process [93].

Technology Selection: evaluate renewable energy technologies based on resource availability, project requirements, and technological maturity. Consider system efficiency, reliability, scalability, and environmental impact.

System Design and Sizing: develop a detailed design of the renewable energy system, including components such as solar panels, wind turbines, energy storage, and balance of system (BOS) equipment. Size the system to meet the project's energy demand while optimizing cost-effectiveness and performance.

Cost Estimation: estimate the capital costs associated with equipment procurement, installation, and commissioning. Consider operational and maintenance (O&M) costs, including labor, materials, and periodic servicing. Evaluate financing options, incentives, and subsidies available for renewable energy projects.

Financial Analysis: calculate the levelized cost of energy (LCOE) to assess the lifetime cost of energy production and compare it with conventional energy sources. Perform cash flow analysis, including net present value (NPV), internal rate of return (IRR), and payback period calculations. Return on investment (ROI) and sensitivity analysis are economic metrics that can be used to account for uncertainties and risks.

Risk Assessment: identify and quantify potential risks and uncertainties associated with the project, including technical, financial, regulatory, and market risks. Develop risk mitigation strategies to address identified risks and enhance project resilience.

Policy and Regulatory Compliance: ensure compliance with relevant policies, regulations, and standards governing renewable energy project development, permitting, and operation. Evaluate the impact of incentives, tax credits, feed-in tariffs, and renewable energy certificates (RECs) on project economics. Compile the findings of the techno-economic evaluation into a comprehensive report for stakeholders, including investors, policymakers, and project developers.

CHAPTER 4

PROPOSED SEGP SYSTEM

The growing need for sustainable and renewable energy solutions has driven significant research and innovation in various energy harvesting technologies. Among these, Sustainable Energy Generating Pads (SEGPs) have emerged as a promising method for capturing ambient mechanical energy. This chapter delves into the comprehensive design, modeling, theoretical analysis, and simulation of SEGP systems, highlighting their potential to convert mechanical vibrations and stresses into electrical energy using piezoelectric materials. Using PZT cells, SEGP systems can effectively harness mechanical energy from everyday activities, such as walking or vehicle movements, to generate electrical power. This chapter is structured to provide a detailed exploration of the SEGP system, starting with its design's foundational concepts and modeling techniques, followed by a theoretical analysis of PZT cells within the SEGP system. In addition, the design of a Dual-Stage-Charge Collection and Storage (DSCS) system is discussed, emphasizing its role in optimizing energy collection and storage [95]–[107].

4.1 Design of a Sustainable Energy Generating Pad (SEGP) System

This section consists of two subsections: modeling the system, mathematical analysis, and simulation, as well as results analysis of the system.

4.1.1 Modeling of a Sustainable Energy Generating Pad (SEGP) System

The proposed SEGP consists of three main parts: top, center, and bottom parts, as shown in Fig. 4.1. The bottom consists of three layers: 1, 2, and 3. The bottom part is made of polyester and microfleece fabric coated with acrylic and adhesive mixture fluids. The

center part of the EGP constitutes the energy generation source that was made of PZT cells, which were coated with a special PVC polymer.

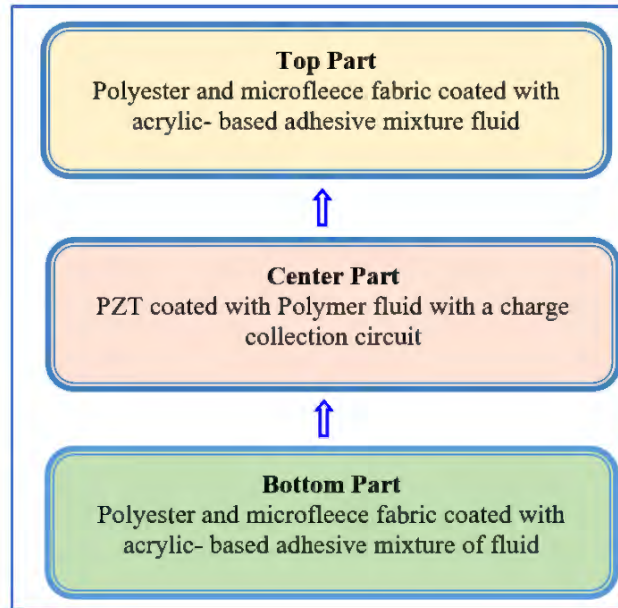


Fig. 4.1 Proposed SEGP System.

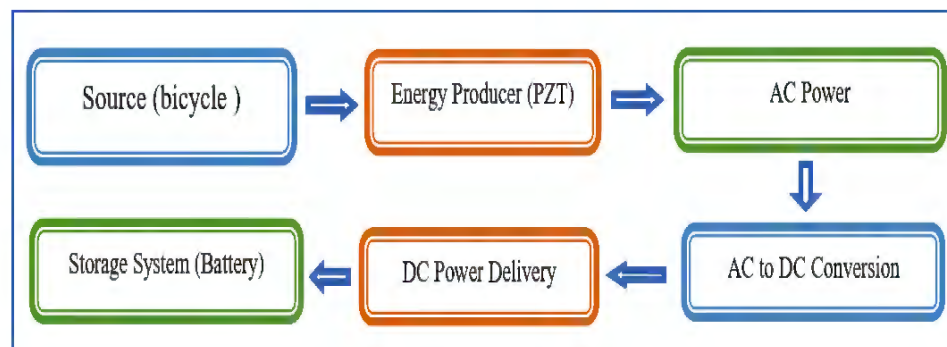


Fig. 4.2 Proposed Energy Collection and Storage Process in the SEGP.

This part of the EGP circuit had charge collection components and the DCPR. The Energy storage process is shown in Fig. 4.2. The top consists of three layers: 5, 6, and 7. The top part was made of polyester and micro-fleece fabrics coated with acrylic and adhesive mixture fluids.

4.1.2 Theoretical Analysis of the SEGP

The mathematical model for estimating power generation from a PZT material by a bike with a rider at a specific speed is discussed below [103], [109],

1. Energy Harvesting from PZT Material:

The power generated (P) by a piezoelectric material can be estimated using the equation:

$$\int P \, dv = \int \frac{1}{2} C f \eta v^2 \, dv \quad (4.1)$$

$$P = \frac{1}{6} C f \eta v^3 \, dv + A \quad (4.2)$$

Where,

P is the power generated (W), C is the capacitance of the PZT material (F), V is the voltage generated (V), f is the frequency of vibration (Hz), η is Mechanical-to-electrical conversion efficiency, A is constant of integration.

2. Rider's Work Done:

The power generated (P_{rider}) by the rider can be estimated as:

$$P_{rider} = \frac{W_{rider}}{t_{ride}} \quad (4.3)$$

Where,

P_{rider} is the power generated by the rider (W), W_{rider} is the work done by the rider (J), which can be estimated as the change in kinetic energy of the rider and bike, t_{ride} is the duration of the ride (s).

3. Work Done and Kinetic Energy:

The work done by the rider (W_{rider}) can be estimated as:

$$W_{rider} = \frac{1}{2}mv^2 \quad (4.4)$$

Where,

m is the mass of the rider and bike (lbs), v is the bike's speed (m/s).

4. Voltage, Current, and Power Relationship:

The power (P) in an electrical circuit can be calculated using the equation:

$$P = VI \quad (4.5)$$

Where,

P = the power (in watts, W), V = the voltage (in volts, V), I = the current (in amperes, A).

5. The PZT cell is a current source with internal resistance and capacitance. For the SEGP, the calculation of the current source is determined using this equation:

$$I_i = I_1 + I_2 + I_3 + \dots + I_{i_n} \quad (4.6)$$

Where, I_1, I_2, \dots, I_{i_n} are the current in PZT cells 1 to n

6. The total internal resistance of the SEGP is determined using this equation:

$$R_{ith} = R_{1th} + R_{2th} + R_{3th} + \dots + R_{ith_n} \quad (4.7)$$

Where $R_{th1}, R_{th2}, \dots, R_{ith_n}$ is the internal resistance of the PZT cells 1 to n .

Internal Resistance (R_{th}) for a Single PZT Cell:

$$R_{ith} = NR = NR_{ith} \quad (4.8)$$

Where R_{ith} is the total internal resistance of the SEGP and N is the number of cells.

7. The total capacitance of the SEGP is determined using this equation:

$$C_i = C_1 + C_2 + C_3 + \dots + C_{i_n} \quad (4.9)$$

Where C_1, C_2, \dots, C_{i_n} is the internal resistance of the PZT cells 1 to n.

Capacitance (C_i) for a Single PZT Cell:

Since the total capacitance (C_i) is the sum of the capacitance of each cell,

The capacitance of a single cell:

$$C_i = NC = NC_t \quad (4.10)$$

Where,

C_t is the total capacitance of the SEGP, and N is the number of cells.

8. Power Generation for a Single PZT Cell:

$$P_{cell} = C_i V_{DC} (V_i - V_{DC} - 2V_{D_i}) F_i \quad (4.11)$$

C_i = the capacitance of the PZT cell, V_{DC} = the voltage produced by the PZT cell,

V_i = the input voltage of the conversion circuit, V_{D_i} = the total voltage drop of the

diode, F_i = the bending frequency of the PZT cell.

9. The following equation describes the total power generation from the SEGP:

$$P_{SEGP} = NC_i V_{DC} (V_i - V_{DC} - 2V_{D_i}) F_i \quad (4.12)$$

The sum of the power generated by individual PZT cells:

$$P_{SEGP} = \sum_{i=0}^n NC_i V_{DC} (V_i - V_{DC} - 2V_{D_i}) F_i \quad (4.13)$$

10. Speed Calculation:

The simplified mathematical equation for estimating power generation from a PZT material on a bike with a rider at a specific speed:

$$\int P dv = \int \frac{1}{2} CA\rho v^3 dv \quad (4.14)$$

P is the power generated (W), C is the piezoelectric coefficient, A is the effective area of the PZT material, ρ is the density of the material, and v is the velocity of the bike and rider in meters per second.

However, including PZT bending limit based on Weight (pressure). This is a piecewise function:

$$\int P dv = \int \frac{1}{2} CA\rho v^3 dv \quad \text{if Weight} \leq 450 \text{ lbs} \quad (4.15)$$

$$0, \quad \text{Weight} > 450 \text{ lbs}$$

Total power generated during the entire journey is integrated into the power function over the range of velocities (v) and time (t) it takes to cover a certain distance (s):

$$P_{total} = \frac{1}{8} CA\rho v^4 + A \quad (4.16)$$

Where P_{total} is the total power generated during the journey. $v(t)$ is the bike and rider's velocity as a time function. $P(v)$ is the instantaneous power function with the weight limit.

11. The mathematical model has been developed,

$$V_{P_{cell}} = a_v \times W + b_v \times d + c_v \times s \quad (4.17)$$

$$I_{P_{cell}} = a_i + b_i \times \frac{W-150}{450-150} \quad (4.18)$$

$$b_i = c_i - a_i \quad (4.19)$$

$$P_{cell} = V_{P_{cell}} \times I_{P_{cell}} \quad (4.20)$$

$$P_{1XSEGP} = \sum_{i=1}^N P_{cell} \quad (4.21)$$

$$P_{2XSEGP} = \sum_{i=1}^N P_{cell} \quad (4.22)$$

Where,

W = The Weight of the bike and rider in pounds (lbs). d = The diameter of the PZT in millimeters (mm). s = The speed of the bike in miles per hour (mph). N = The number of PZT cells. Coefficients: $a_v = 0.709667$, $b_v = 0.00007072$, $c_v = -0.00038036$; $a_i = 0.00018$, $c_i = 0.00041$.

4.1.3 Simulation and Analysis of a 1X Sustainable Energy Generating Pad (SEGP_{1X}) System

Proteus software is used to simulate the SEGP. Proteus is also one of the best electronic circuit simulation tools, like other popular software such as NI Multisim, Orcad, and LTSpice. In the modeling section, Layer 3 is designated as the energy-generating layer, fashioned with PZT cells of the 5A type, each having a 20 mm diameter.

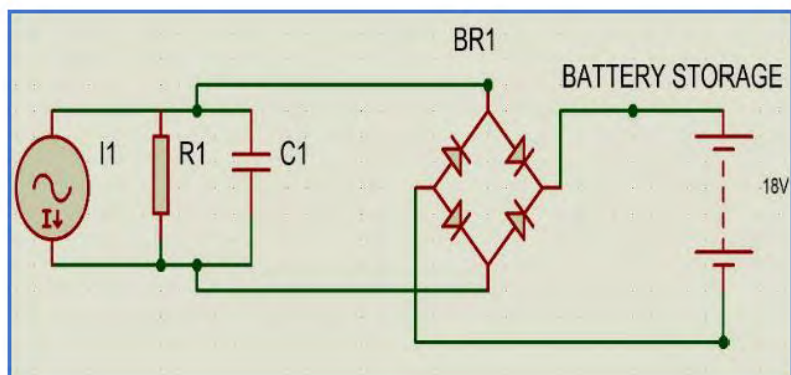


Fig. 4.3 Equivalent Circuit of the SEGP System.

To construct a 1-foot width and 5-foot long 1X-SEGP, a grid configuration of 30 columns and six rows of PZT cells is utilized, having each cell connected to an AC-to-DC conversion circuit. A simple rectification circuit is used here for this modeling.

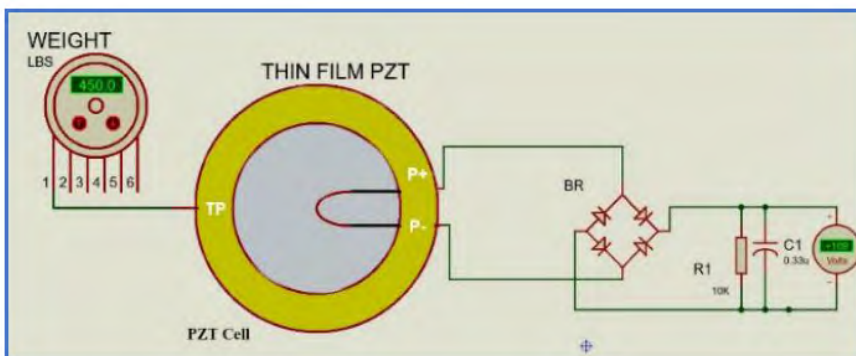


Fig. 4.4 Voltage Testing on Max Pressure of PZT cell of 1X SEGP.

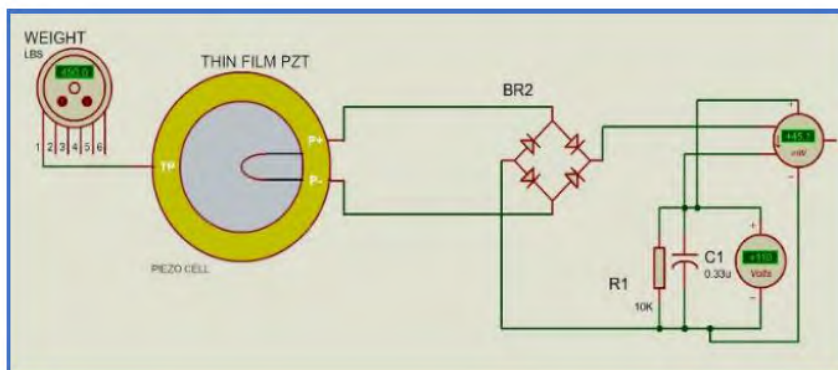


Fig. 4.5 Power Testing on Max Pressure of PZT cell of 1X SEGP.

TABLE 4.1

SIMULATION ANALYSIS OF 1X SEGP

<i>Weight (lbs)</i>	<i>PZT-5A (mm)</i>	<i>Voltage (V_{max})</i>	<i>R kΩ</i>	<i>C μF</i>	<i>Current (mA)</i>	<i>PZT Cell Power (mW)</i>	<i>1X-SEGP Power (W/ride)</i>
150	25	110	10	0.33	0.18	19.8	0.594
250	25	110	10	0.33	0.25	28.2	0.847
350	25	110	10	0.33	0.33	36.6	1.100
450	25	110	10	0.33	0.41	45.1	1.353
>450	25	-----	10	0.33	-----	-----	-----

The simulation of the equivalent circuit of the PZT cell in Proteus software, as shown in Fig. 4.3, is conducted to examine the voltage and current characteristics in response to the applied force on individual PZT cells. The results demonstrated that power generation by the SEGP increased with greater mechanical loads. For example, at 150 lbs, a voltage of 110 V and a current of 0.18 mA is generated, as shown in Figure 4.4 and Figure 4.5, resulting in 19.8 mW of PZT cell power and 0.594 W of 1X-SEGP power. As the weight incrementally increased, the energy generation increased by around 25 % until it reached the maximum limit, as discussed in Table 4.1. However, it is worth noting that at 450 lbs, a significant increase in power generation was observed. The SEGP generated 110 V voltage and 0.41 mA current, as shown in Table 4.1, resulting in 45.1 mW of PZT cell power and 1.353 W of 1X-SEGP power.

4.1.4 Simulation and Analysis of a 2X Sustainable Energy Generating Pad (SEGP_{2X}) System

For the simulation of the 2X-SEGP, the construction process remains identical to that of the 1X-SEGP, with the only variation being the placement of two 1X-SEGP, one

stacked atop the other. Consequently, the total number of PZT cells utilized for the 5-foot-long 2X-SEGP is doubled. This results in the incorporation of 360 PZT cells with the same grid configuration, comprising $(30 \text{ columns and } 6 \text{ rows}) \times 2$. The Proteus software is employed for the simulation to measure both voltage and current characteristics, as illustrated in Fig. 4.6 & 4.7.

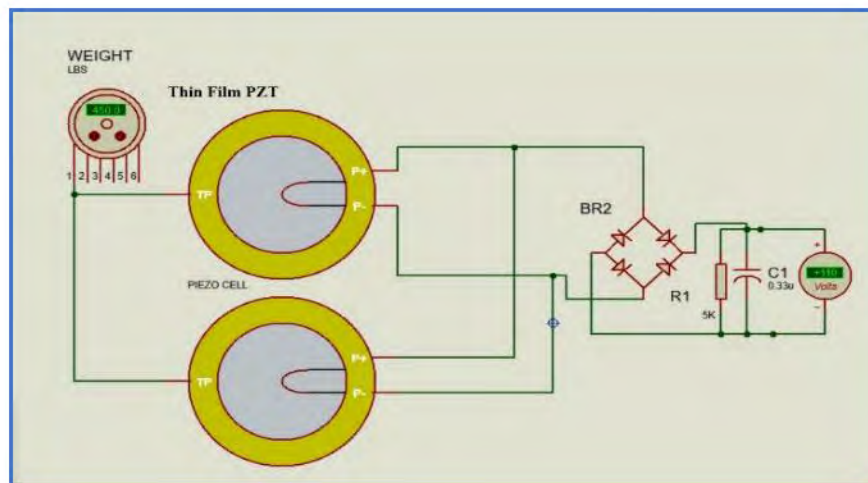


Fig. 4.6 Voltage Testing on Max Pressure of PZT cell of 2X-SEGP.

The result shows that power generation by the SEGP increases with greater mechanical loads. For instance, at 155 lbs, it generates 110 V voltage and 0.43 mA current, as shown in Table 4.2, resulting in 51.7 mW of PZT cell power and 1.425 W/ride of 2X-SEGP power. At 450 lbs, the voltage remains stable at 110 V, while the current increases to 0.98 mA, producing 108.2 mW of PZT cell power and 3.427 W/ride of 2X-SEGP power. Beyond 450 lbs, power generation ceases, attributed to PZT cell failure above this pressure threshold. This study investigated the performance of 1X-SEGP for energy harvesting applications, specifically the 1X-SEGP and 2X-SEGP. In simulation studies, both SEGPs exhibited increased power generation with higher mechanical loads, with the 2X-SEGP outperforming the 1X-SEGP, as shown in Fig. 4.8. The results confirmed the 2X-SEGP's

superior power output. Notably, it demonstrated a substantial increase in power generation, 250 % - 480 %, compared to the 5-foot 1X-SEGP.

TABLE 4.2
SIMULATION ANALYSIS OF 2X-SEGP

Weight (lbs)	PZT-5A (mm)	Voltage (V_{max})	R k Ω	C μ F	Current (mA)	PZT Cell Power (mW)	2X-SEGP Power (W/ride)
150	25	110	5	0.33	0.43	47.5	1.425
250	25	110	5	0.33	0.61	61.6	2.032
350	25	110	5	0.33	0.80	88.0	2.64
450	25	110	5	0.33	0.98	108.2	3.247
>450	25	-----	5	0.33	-----	-----	-----

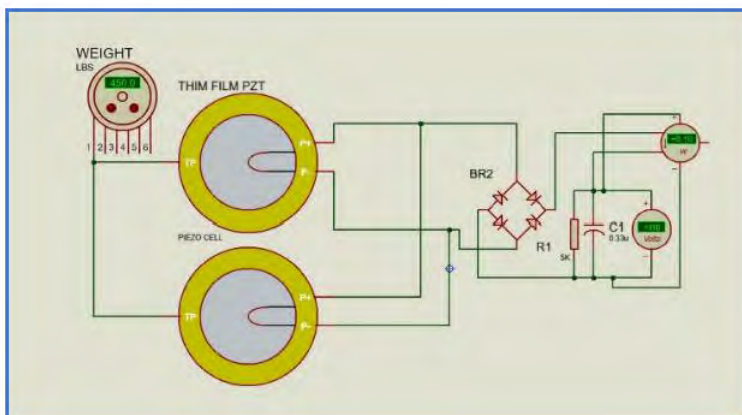


Fig. 4.7 Power Testing on Max Pressure of PZT cell of 2X SEGP.

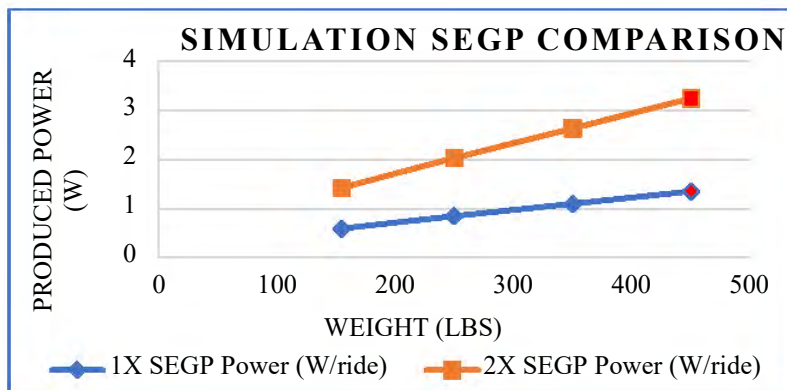


Fig. 4.8 Simulation Result Comparison for Both the SEGP.

The multiple linear regression equation for the given data from Fig. 4.8 is:

$$P_{1XSEGP} = 0.253w + 0.341 \quad (4.23)$$

$$P_{2XSEGP} = 0.6074w + 0.8175 \quad (4.24)$$

Where: Weight (lbs) is the independent variable (w). 1X-SEGP Power (W/ride) is the dependent variable (P_{1XSEGP}). 2X-SEGP Power (W/ride) is the dependent variable (P_{2XSEGP}).

4.2 Design of a Dual-Stage-Charge Collection and Storage (DSCS) System

The SEGP produced high peak acyclic signals, and regular available energy storage chargers may not be efficiently collected to maximize energy extraction. Standard electrical energy storage devices include Nickel, Lead-acid, Supercapacitors, and Lithium-ion Batteries. Among these options, energy storage in lithium-ion batteries emerges as the optimal choice in contemporary times. This preference is due to several factors, including their extended lifespan, high energy density, and minimal energy loss during shelf-discharging. Therefore, designing a DSCS system is crucial for collecting maximum energy from the SEGP and ensuring the system's sustainability. So, A DSCS is designed for the SEGP, as shown in Fig. 4.10. The SEGP has 7 layers. An energy generation unit is inside the SEGP, which is layer 5, as shown in Fig. 4.9. The energy generation unit consists of sources, which are PZT cells and AC to DC converters. Finally, The power produced from the SEGP is stored in the li-ion batteries by a DSCS. The SEGP's design with the DSCS system is shown in Fig. 4.9. An unbalanced peak AC power (UPAP) signal was converted into DC power through full-wave rectification. A specialized DSCS electronic

module is designed and simulated to maximize energy utilization for alternative energy applications, as shown in Fig. 4.10 (design) & 4.11 (circuit schematic by proteus software). Fig. 4.11 shows the model of this DSCS Electronic Module, which comprises a DSCS Unit integrated with a microcontroller-based control system programmed for enhanced performance and efficiency. The algorithm and the operational flowchart of the DSCS module are discussed in Fig. 4.12, depicting the sequence of actions and interactions within the system. The CCSU is structured as a dual-stage system, with the first stage (CCSU#1) serving as a rapid voltage-boosting charging mechanism called Storage V_{boost} .

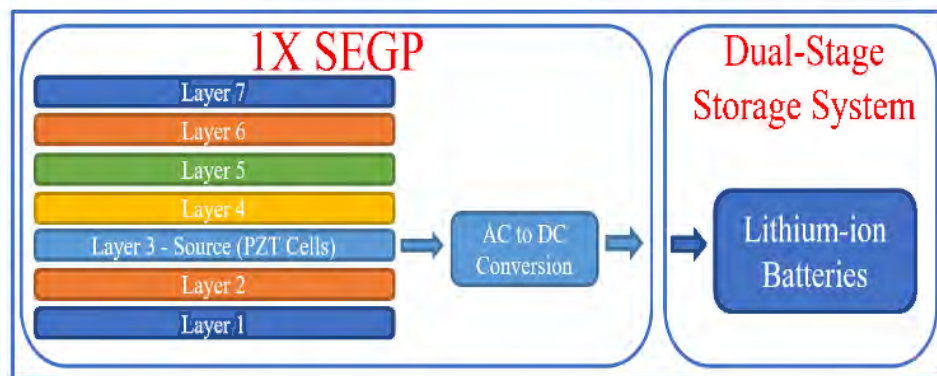


Fig. 4.9 Proposed 1X-SEGP Energy Storage System.

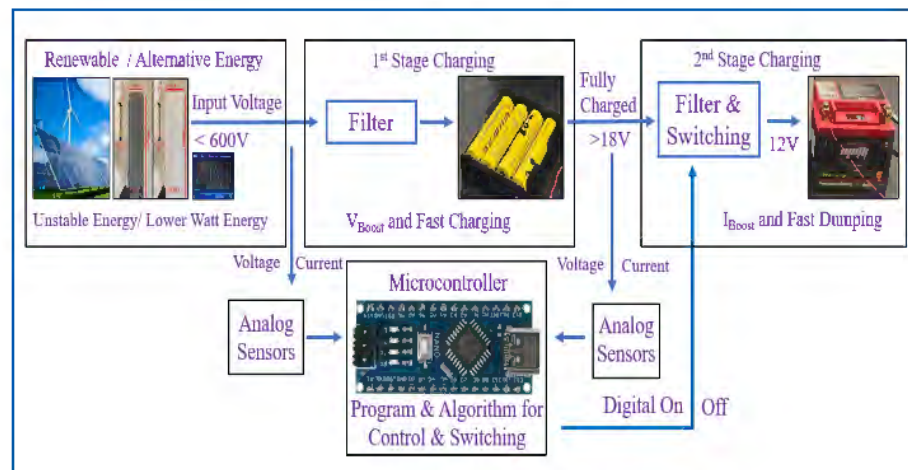


Fig. 4.10 Design of the Dual-Stage Charge Collection and Storage System.

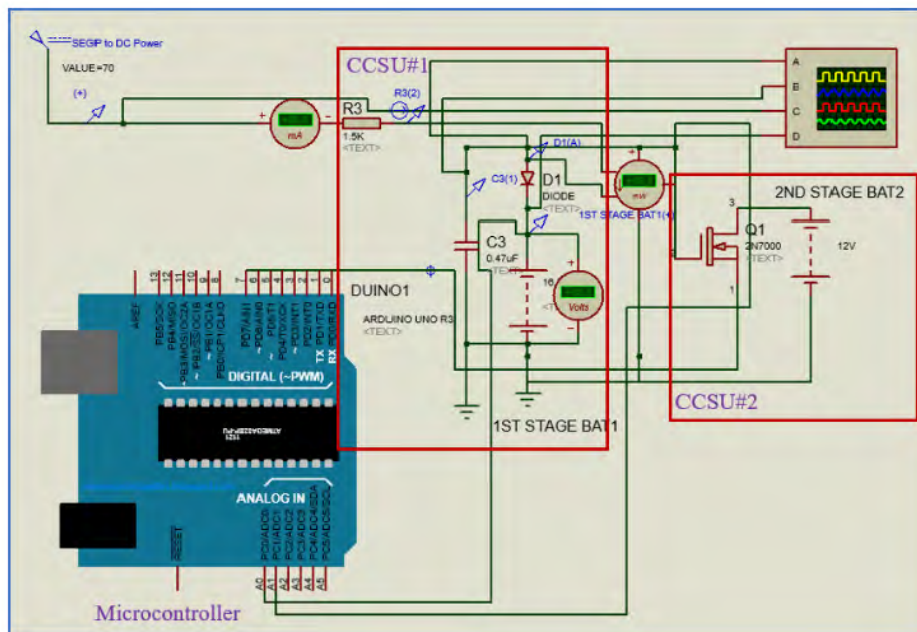


Fig. 4.11 Circuit Schematic of the DSCS System.

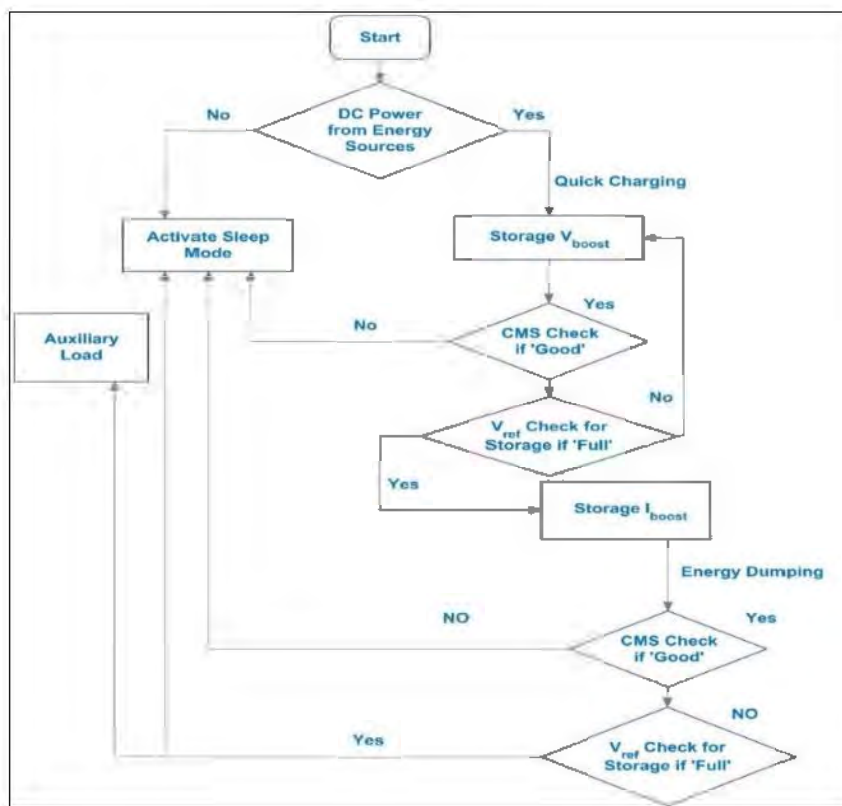


Fig. 4.12 Proposed Algorithm of DSCS System.

The second stage (CCSU#2) acts as a current-boosting Energy Dumping System (EDS) called Storage I_{boost} . A Charge Management System (CMS) was developed to manage the charging process effectively with a custom-coded program and algorithm implemented on the microcontroller. The CMS continuously monitors the health status of the storage devices, including factors such as temperature, overload conditions, and more.

4.3 Summary

This chapter provided an in-depth description of SEGPs and their potential for converting mechanical energy into electrical energy using piezoelectric cells. It began with a detailed modeling and theoretical analysis of PZT cells in the SEGP. The chapter presented simulation studies of the first generation of SEGP_{1X} and second Generation of SEGP_{2X} configurations, showcasing their performance. The design and functionality of a DSCS system were also discussed, highlighting its significance. This chapter underscored the viability of SEGP systems as a sustainable energy solution and set the stage for future research and practical implementations of SEGP technologies.

CHAPTER 5

PROTOTYPE DEVELOPMENT & FAILURE ANALYSIS

The development of prototypes plays a crucial role in innovation and product design, serving as a bridge between conceptualization and real-world implementation. This chapter focuses on prototype development and failure analysis, highlighting the iterative nature of design processes and the importance of learning from setbacks. Prototypes serve as tangible representations of ideas, allowing designers and engineers to test functionality, gather feedback, and refine designs before final production. However, not all prototypes succeed, and failure analysis becomes instrumental in understanding what went wrong, identifying areas for improvement, and ultimately driving innovation forward. This chapter delves into the methodologies, challenges, and lessons learned from prototype development and failure analysis, offering valuable insights into the SEGP Technologies [94]-[107].

5.1 Prototype AEH Model for PZT Cells Characteristics Analysis

An alternative energy harvesting (AEH) system has been developed to investigate thin-film energy in diverse multi-layered composite PZT cells, integrating a Smart Charging System (SCS) for efficient energy storage in lithium batteries. The main goal is to utilize energy from thin-film PZT cells as a prospective alternative energy source for generating power on roadways. Each layer of the composite thin-film PZT undergoes individual evaluation to assess its unique characteristics and energy generation potential, resulting in unstable acyclic lower energy, which is very complicated to store. So, a smart charging system requires managing the charging process and ensuring efficient energy

storage. This study focused on improving the efficiency and reliability of multi-layered energy harvesting from thin-film PZT cells. Various analytical techniques are employed to assess parameters such as energy generation capacity, pressure, speed, and overall system effectiveness.

5.1.1 Model for the PZT Cell Characteristics Analysis

An AEH utilizing a Thin-film PZT cell, as shown in Fig. 5.1, has been designed and fabricated to quantify the energy output from thin-film PZT material. This AEH employs a lever mechanism to flex the thin-film PZT via two plungers, each applying a force of 20 N during peak load conditions. The system incorporates a control unit to regulate the plunger speed. When force is exerted on different layers of the thin-film PZT, it undergoes deformation, generating an alternating current (AC) signal. The AEH includes an AC-to-DC converter system to harness this AC energy to transform the generated signal into direct current (DC). Further, a variable resistor and capacitor in the load circuitry are used to smooth the DC output. The energy is then directed to a Lithium-ion battery via a dual-stage charging system optimized called SCS for efficient energy collection and storage due to the relatively low energy produced. The simulation of a thin-film PZT cell to energy stores in the Battery via a SCS using proteus software is shown in Figure 5.2. For detailed energy analysis, the system is connected to an oscilloscope. This analytical process involves examining voltage, current, resistance, and time data gathered during experimentation. The Prototype development and experimental results sections discuss and analyze the energy output from different layers of thin-film PZTs, showcasing the system's capabilities.

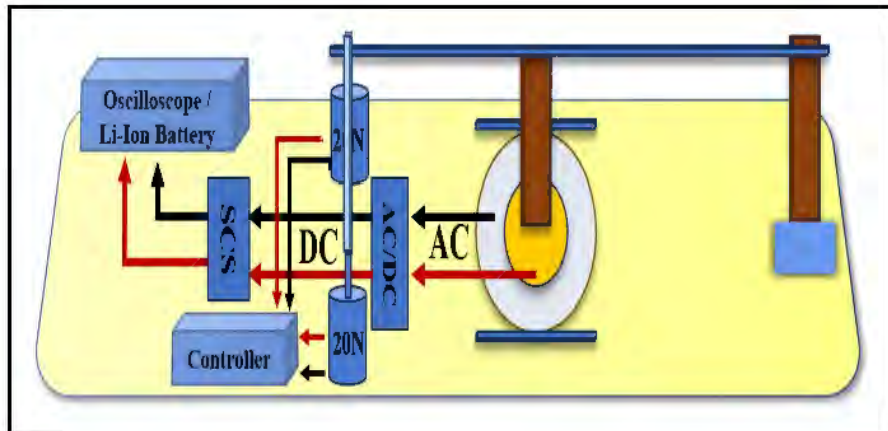


Fig. 5.1 The Model of AEH (PZT Cell)

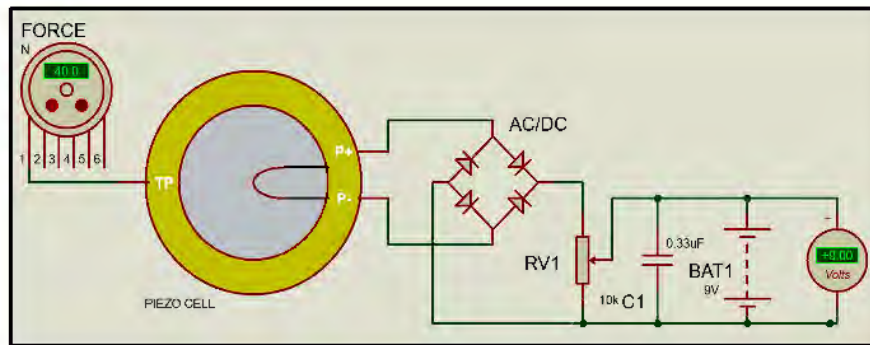


Fig. 5.2 Simulation Schematic of AEH (PZT Cell) with SCS.

5.1.2 Characteristics Analysis of 1X-Layer of PZT Cell

The experimental prototype model of the 1X-Layer AEH, illustrated in Fig. 5.3, has been devised and constructed to analyze the behavior of the 1X Layer of thin-film PZT when subjected to force within the PZT cell. This experimental setup applies approximately 40 Newtons of force to the PZT via the system lever, generating an acyclic AC signal by the single thin-film PZT cell. The AC-DC conversion system, equipped with a parallelly connected 10 k Ω resistor and a 0.33 μ F capacitor for energy smoothing, transforms the generated AC energy into DC energy, which is then stored in the battery using the SCS charging system. Additionally, it is connected to an oscilloscope to analyze the produced

signal and ascertain parameters such as average voltage and power over specific time intervals. The outcomes of these experiments are discussed in the result analysis sections.

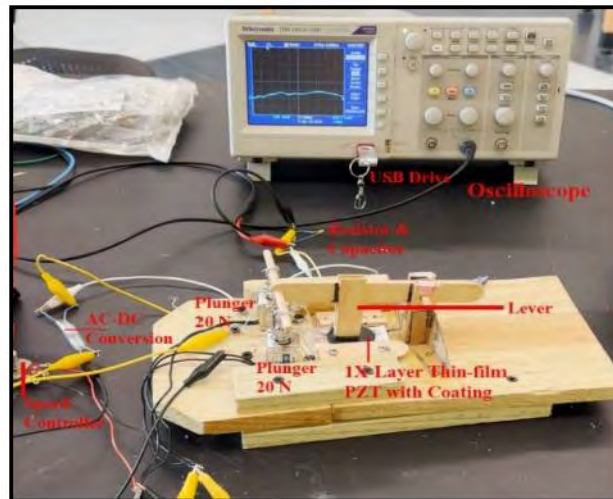


Fig. 5.3 Prototype of the AEH for Thin-Film 1-layer PZT Cell.

5.1.3 Characteristics Analysis of 2X-Layer of PZT Cell

The experimental prototype model of the 2X-Layer AEH, depicted in Fig. 5.4, has been developed to investigate the behavior of the 2X Layer of thin-film PZT when subjected to force within the PZT cell. This experimental setup applies in the same way as 1X-Layer around 40 Newtons of force to the PZT through the system lever, generating an acyclic AC signal by the single thin-film PZT cell. The AC-DC conversion system is configured with a parallelly connected 5 k Ω resistor and a 0.33 μ F capacitor to smooth the energy, converting the generated AC energy into DC energy. This DC energy is then stored in the battery using the SCS charging system. Furthermore, the system is linked to an oscilloscope for signal analysis, determining parameters like average voltage and power across specific time intervals. The results analysis sections also discuss the outcomes of these 2X-Layer experiments.

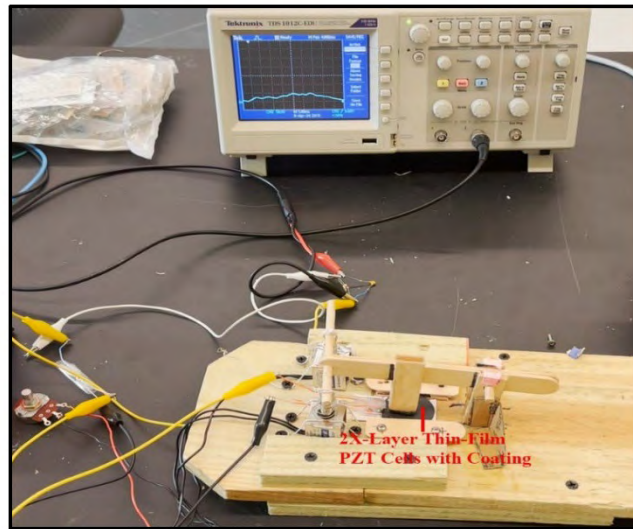


Fig. 5.4 Prototype of the AEH for Thin-Film Dual-layer PZT Cell.

5.1.4 Characteristics Analysis of 3X-Layer of PZT Cell

The experimental prototype model of the 3X-Layer AEH, depicted in Fig. 5.5, has been custom-built to investigate the behavior of the 3X Layer of thin-film PZT under applied force within the PZT cell. This experimental setup applies an approximate force of 40 Newtons to the PZT via the system lever, leading to the generation of an acyclic AC signal by the 3X Layer of the thin-film PZT cell. The AC-DC conversion system is incorporated and parallelly connected with a 3.3 k Ω resistor and a 0.33 μ F capacitor to ensure energy smoothing, facilitating the conversion of the generated AC energy into DC energy. This converted energy is then stored in the battery through the SCS charging system. Furthermore, the setup is connected to an oscilloscope for signal analysis, allowing for the determination of parameters such as average voltage and power over specific time intervals, which also delves into the findings from these 3X-Layer experiments.

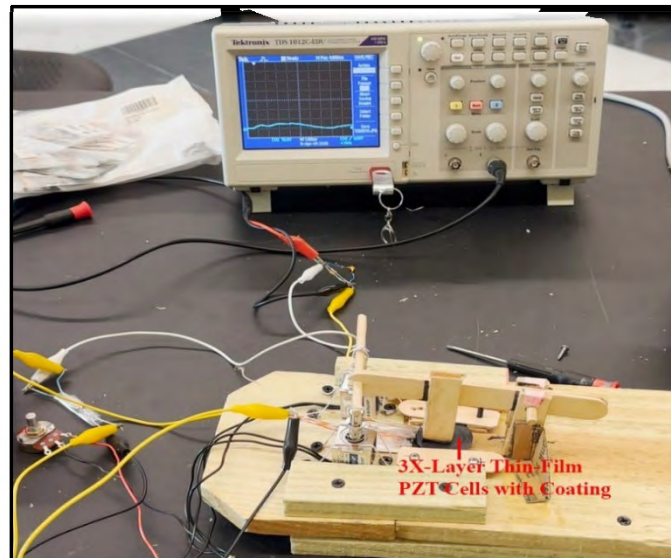






Fig. 5.5 Prototype of the AEH for Thin-Film Tripple-layer PZT Cell.





5.2 Materials Analysis for Energy Generating Pad Development





Table 5.1 evaluates the performance of various paint mixtures applied to cloth and fleece, assessing their adhesion, flexibility, waterproof properties, and durability underwater. Ash Paint (AP) and Red Paint (RP) on cloth and fleece showed proper initial adhesion but failed after 48 hours underwater. Grey Paint (GP) on both cloth and fleece maintained adhesion and waterproof properties, making them viable options. Mixtures incorporating silicon and flax were flexible and waterproof initially but failed after drying. Using specific combinations, GR_cF and GR_c were used to blend paints and other materials, including R_cP (a multi-composite paint), which remained properly glued and waterproof after 48 hours underwater, suggesting their potential for flexible and durable applications. However, other mixed paint samples, such as AG_1 , AG_2 , GR_1 , GR_2 , AR_1 , and AR_2 , did not maintain adhesion underwater and were rejected. The study concludes that GP mixtures on both cloth and fleece offer the best performance for the tested conditions.





TABLE 5.1

MATERIALS ANALYSIS FOR DEVELOPING EGP

Sample Type	Mixture & Process	1 Layer	2 Layer	Nonflexible	Flexible	Waterproof	Observation	Remarks	Image
Ash Paint (AP)	Cloth with AP 100% & initially Wet	Ok	Ok	Yes	No	No	Properly glued	Properly glued, but after 48 hours underwater, both layers of water separated. So, Rejected	
Grey Paint (GP)	Cloth with GP 100% & initially Wet	Ok	Ok	Yes	No	Yes	Properly glued	Properly glued, but after 48 hours underwater, both layers were glued and waterproof. So, Considered	
Red Paint (RP)	Cloth with RP 100% & initially Wet	Ok	Ok	Yes	No	Yes	Properly glued	Properly glued, but after 48 hours underwater, both layers of water separated. So, Rejected	
Ash Paint (AP)	Fleece with AP 100% & initially Wet	Ok	Ok	Yes	No	No	Did not glue properly	Properly glued, but after 48 hours underwater, both	

								layers of water separated. So, Rejected	
Grey Paint (GP)	Fleece with GP 100% & initially Wet	Ok	Ok	Yes	No	Yes	Properly glued	Properly glued, but after 48 hours underwater, both layers were glued and waterproof. So, Considered	
Silicon (SP)	Cloth with GP 70%, 30% Silicon & initially Wet	Ok	Ok	No	Yes	Yes	Separate both materials	Flexible & Waterproof. However, it failed because all layers were separated after drying.	
Flax (FP)	Cloth with GP 70%, 30% Flax & initially Wet	Ok	Ok	No	Yes	Yes	Separate both materials	Flexible & Waterproof. However, it failed because all layers were separated after drying.	
AG1	Cloth with AP 50%, 50% GP & L1 AP over L1 GP	Ok	Ok	Yes	No	No	Semi glued	Properly glued, but after 48 hours underwater, both layers	

								of water separated. So, Rejected	
AG2	Cloth with AP 50%, GP & mixed properly and paint	Ok	Ok	Yes	No	No	Semi glued	Properly glued, but after 48 hours underwater, both layers of water separated. So, Rejected	
GR1	Cloth with RP 50%, GP & L1 AP over L1 GP	Ok	Ok	Yes	No	No	Properly glued	Properly glued, but after 48 hours underwater, both layers of water separated. So, Rejected	
GR2	Cloth with RP 50%, GP & mixed properly and paint	Ok	Ok	Yes	No	No	Properly glued	Properly glued, but after 48 hours underwater, both layers of water separated. So, Rejected	
AR1	Cloth with RP 50%, AP & L1 AP over L1 GP	Ok	Ok	Yes	No	No	Semi glued	Properly glued, but after 48 hours underwater, both layers of water separated. So,	

								Rejected	
AR2	Cloth with AP 50%, 50% AP & mixed properly and paint	Ok	Ok	Yes	No	No	Semi glued	Properly glued, but after 48 hours under water, both layers of water separated. So, Rejected	
GScRc	Cloth with AP 50%, 25% ScP, 25% Rc & mixed properly and paint	Ok	Ok	No	Yes	Yes	Properly glued	Flexible & Waterproof. However, it failed because all layers were separated after drying. Rejected	
GRcF	Cloth with AP 50%, 25% RcP, 25% FP & mixed properly and paint	Ok	Ok	No	Yes	Yes	Properly glued	Properly glued, and after 48 hours under water, both layers are still glued and waterproof. So, Considered	
GRc	Cloth with AP 50%, 25% RcP, & mixed properly and paint	Ok	Ok	No	Yes	Yes	Properly glued	Properly glued, and after 48 hours under water, both layers	





								are still glued and waterproof. So, Considered	
Arc	Cloth with AP 70%, 30% RcP, & mixed properly and paint	Ok	Ok	No	Yes	No	Properly glued	Properly glued, but after 48 hours underwater, both layers of water separated. So, Rejected	

Table 5.2 assesses the performance of various paint mixtures applied to cloth combined with PZT layers, evaluating adhesion, flexibility, waterproof properties, and durability underwater. Samples using Ash Paint (AP₁, AP₂) and Red Paint (RP₁, RP₂) exhibited proper initial adhesion but failed to maintain integrity after 48 hours underwater. In contrast, samples using Grey Paint (GP₁, GP₂) and Flex Paint (FP₁, FP₂) demonstrated both adhesion and waterproof properties, remaining intact after the 48-hour underwater test, making them suitable for consideration. This study indicates that Grey Paint and Flax Paint mixtures, regardless of the PZT coating, offer the best performance in terms of adhesion and waterproofing, while Ash Paint and Red Paint mixtures were less successful under similar conditions.


TABLE 5.2

GLUED TEST ANALYSIS ON PZT AND PAD LAYERS

Sample Type	Mixture & Process	1 Layer	2 Layer	Nonflexible	Flexible	Waterproof	Observation	Remarks	Image
Ash Paint (AP1)	Cloth with AP 100%, PZT without Coated & initially Wet	Cloth with AP 100%,	PZT without Coated	yes	No	No	Properly glued	Properly glued, but after 48 hours underwater, both layers of water separated. So, Rejected.	
Grey Paint (GP1)	Cloth with GP 100%, PZT without Coated & initially Wet	Cloth with GP 100%,	PZT without Coated	yes	No	Yes	Properly glued	Properly glued, but after 48 hours underwater, both layers were glued and waterproof. So, Considered	

Red Paint (RP)1	Cloth with AP 100%, PZT with Coated & initially Wet	Cloth with RP 100%,	PZT witho ut Coate d	yes	No	No	Properly glued	Properly glued, but after 48 hours underwat er, both layers of water separated . So, Rejected	
Flax Paint (FP1)	Cloth with FP 100%, PZT without Coated & initially Wet	Cloth with GP 100%,	PZT witho ut Coate d	yes	No	Yes	Properly glued	Properly glued, but after 48 hours underwat er, both layers were glued and waterpro of. So, Consider ed	
AP2	Cloth with AP 100%, PZT without Coated &	Cloth with AP 100%,	PZT with Coate d	yes	No	No	Properly glued	Properly glued but after 48 hour under water,	

	initially Wet							both layer water separated . So, Rejected	
GP2	Cloth with GP 100%, PZT without Coated & initially Wet	Cloth with GP 100%,	PZT with Coate d	yes	No	Yes	Properly glued	Properly glued, but after 48 hours underwat er, both layers were glued and waterpro of. So, Consider ed	
RP2	Cloth with AP 100%, PZT with Coated & initially Wet	Cloth with RP 100%,	PZT with Coate d	yes	No	No	Properly glued	Properly glued, but after 48 hours underwat er, both layers of water separated . So, Rejected	

FP2	Cloth with FP 100%, PZT without Coated & initially Wet	Cloth with GP 100%,	PZT with Coated	yes	No	Yes	Properly glued	Properly glued, but after 48 hours underwater, both layers were glued and waterproof. So, Considered	
-----	--	---------------------	-----------------	-----	----	-----	----------------	--	---

5.3 Prototype of a Sustainable Energy Generating Pad (SEGP) System

Based on the developed design and simulation analysis results in Chapter 4, Different types of prototype models are developed and tested in the laboratory to make the SEGP efficient and economical.

5.3.1 Prototype 1: Energy Generating Pad₁ (EGP₁)

EGP₁ experimented with different configurations involving hard paper layers and various arrangements of PZT elements, as shown in Fig. 5.6. The outcome was a successful generation of almost 65 VDC voltage. However, a drawback emerged as the PZT started to crack after approximately 150 times of bike running on the pad. Therefore, while the voltage generation was achieved, the durability of the PZT components needs improvement to ensure long-term functionality.



Fig. 5.6 Prototype of the EGP₁.

5.3.2 Prototype 2: Energy Generating Pad₂ (EGP₂)

EGP₂ utilized a polyester fabric with PVC coating and Ash paint, as shown in Fig. 5.7, achieving a 60-65 VDC voltage, passing flexibility but failing stress and waterproof tests. Despite successful operation, drawbacks included non-waterproofing and layer detachment due to the PVC material.



Fig. 5.7 Prototype of the EGP₂.

5.3.3 Prototype 3: Energy Generating Pad₃ (EGP₃)

EGP₃ developed with different layers, as shown in Fig. 5.8. Layer 1 consisted of 100 % polyester fabric with PVC coating and AP, resulting in a voltage output of 0 VDC. While this layer passed the flexibility test, it failed both the stress and waterproof tests.



Fig. 5.8 Prototype of the EGP₃

One notable issue was that layers 1 and 7 did not attach to the other layers due to the PVC material. This failure was due to the non-functioning AC, likely causing temperature and humidity changes that affected the bonding process. Layers 2 and 3 utilized 100% polyester microfleece coated with AP. Layer 4 incorporated 2L of yellow hard paper attached with wooden glue below the PZT rail strips. Layer 5 featured PZT with a charge collector circuit, with the upper layer of PZT coated with Black sticky materials and connected vertically. Layers 6 and 7 utilized 100% polyester micro fleece coated with a mixture of AP 80% and RC 20%. Lastly, Layer 8 utilized 100 % polyester fabric with PVC coating on the backside.

5.3.4 Prototype 4: Energy Generating Pad₄ (EGP₄)

The EGP₄ involved the use of different materials and configurations across multiple layers, as shown in Fig. 5.9. Layer 1 utilized 100% polyester fabric with a PVC coating and AP, achieving a voltage output of 30-40 VDC while passing flexibility and stress tests but failing the waterproof test. This layer also faced challenges with detachment and non-waterproofing, attributed to factors like environmental conditions and material properties. Layers 2 and 3 employed 100% polyester microfleece coated with AP. Layer 4 introduced 2L yellow hard paper with AP beneath PZT rail strips, likely for reinforcement and insulation purposes. Layer 5 featured PZT with a charge collector circuit, including an upper layer coated with sticky black materials that is vertically connected. Layers 6 and 7 utilized 100% polyester microfleece coated with a mixture of AP 80% and RC 20%, potentially aiming for improved adhesion and durability. Layer 8 employed 100% polyester fabric with PVC coating on the backside, possibly addressing previous waterproofing and detachment issues through material choice.



Fig. 5.9 Prototype of the EGP₄.

5.3.5 Prototype 5: Energy Generating Pads (EGP₅)

The EGP₅ involved the use of various materials and configurations across different layers, as shown in Fig. 5.10. Layer 1 featured a fabric material coated with GP 100%, achieving a voltage output of 60-62 VDC. This layer demonstrated semi-flexibility in the flexibility test, passed the stress test, and proved to be waterproof, successfully running with the drawback from Sample 1 resolved.



Fig. 5.10 Prototype of the EGP₅.

However, it was noted that the pad was very hard, requiring more flexibility to improve its lifetime. Layer 2 utilized fabric coated with GP 100%, although specific outcomes were not detailed. Layer 3 introduced PZT with a charge collector circuit, with the upper PZT layer coated with sticky Black materials and connected vertically. Layer 4 consisted of 100% polyester microfleece coated with a mixture of GP 50%, RC 25%, and Flex 25%. Layers 5 and 6 both utilized fabric coated with GP 100%.

5.3.6 Prototype 6: Energy Generating Pad₆ (EGP₆)

The EGP₆ used different materials and configurations across multiple layers, as shown in Figure 5.11. Layer 1 utilized 100% fabric coated with GP 100%, resulting in a voltage output of 12 VDC. While this layer demonstrated semi-flexibility in the flexibility test and passed the stress test, it failed due to a possible internal shortage issue. Layer 2 also used fabric coated with GP 100%. Layer 3 introduced PZT with a charge collector circuit, featuring an upper PZT layer coated with Black sticky materials and horizontally connected PZT rails. Layer 4 consisted of 100% fabric coated with a mixture of GP 50%, RC 25%, and Flex 25%. Layers 5 and 6 utilized 100% polyester microfleece coated with GP 100%.



Fig. 5.11 Prototype of the EGP₆.

5.3.7 Prototype 7: Energy Generating Pad₇ (EGP₇)

The EGP₇ utilized a variety of materials and coatings across different layers, as shown in Fig. 5.12. Layer 1 employed 100% fabric coated with GP 100%, achieving a voltage output of 60-68 VDC. This layer demonstrated semi-flexibility, passed the stress

test, and proved to be waterproof, running successfully. However, a drawback noted was that the pad was very shiny and slippery. Layer 2 featured fabric 100% placed under the rail strips and coated with GP 100%. Layer 3 introduced a foam layer under the PZT rails, likely as cushioning or support. Layer 4 is comprised of PZT with a charge collector circuit connected vertically. Layers 5 and 6 both utilized 100 % fabric coated with a mixture of GP 50%, RC 25%, and Flex 25%. Layer 7 was composed of 100% fabric coated with AP 100%.



Fig. 5.12 Prototype of the EGP₇.

5.3.8 Prototype 8: Energy Generating Pad₈ (EGP₈)

The EGP₈ utilized a variety of materials and coatings across different layers, as shown in Fig. 5.13. Layer 1 consisted of 100% fabric coated with GP 100%, achieving a voltage output of 60-68 VDC, as described in Table 5.10. This layer demonstrated semi-flexibility, passed the stress test, and proved to be waterproof, running successfully. However, a drawback was that the pad was very shiny and slippery, with a natural drying

time of 7 days. Layer 2 featured fabric 100% placed under the rail strips and coated with GP 100%. Layer 3 introduced a foam layer under the PZT rails, likely as cushioning or support. Layer 4 is comprised of PZT with a charge collector circuit connected vertically. Layers 5 and 6 both utilized 100% fabric coated with a mixture of GP 80% and RC 20%. Layer 7 was composed of 100% fabric coated with GP 100%.



Fig. 5.13 Prototype of the EGP₈.

5.3.9 Prototype 9: Energy Generating Pad₉ (EGP₉)

Layer 1 of EGP₉ utilized 100% fabric coated with GP 100%, achieving a voltage output of 60-68 VDC, as described in Figure 5.14. This layer demonstrated semi-flexibility, passed the stress test, and proved to be waterproof, running successfully. However, a drawback noted was that the pad was very shiny, slippery, and foamy, which led to its rejection despite its overall success. Layer 2 featured fabric 100% placed under the rail strips and coated with GP 100%. Layer 3 introduced a foam layer under the PZT rails,

likely as cushioning or support. Layer 4 comprised PZT with a charge collector circuit connected horizontally. Layer 5 utilized 100% polyester microfleece coated with a mixture of AP 80% and RC 20%. Layer 6 consisted of 100% fabric coated with a mixture of AP 40%, GP 40%, and RC 20%. Layer 7 is composed of 100% fabric coated with AP 100%.



Fig. 5.14 Prototype of the EGP₉

5.3.10 Prototype 10: Energy Generating Pad₁₀ (EGP₁₀)

The EGP₁₀ used various materials and configurations across different layers, as described in Figure 5.15. Layer 1 utilized 100% fabric coated with GP 100%, achieving a voltage output of 60-62 VDC. This layer demonstrated semi-flexibility, passed the stress test, and proved to be waterproof, running successfully. It was noted that the pad was semi-hard and flexible, indicating room for improvement in terms of flexibility to enhance its lifetime. Layer 2 also utilized fabric 100% coated with GP 100%. Layer 3 introduced PZT with a charge collector circuit, featuring an upper layer coated with sticky Black materials and vertically connected PZT rails. Layer 4 consisted of 100% polyester microfleece coated

with a mixture of GP 50%, RC 25%, and Flex 25%. Layers 5, 6, and 7 all utilized fabric 100% coated with GP 100%.

TABLE 5.3
EXPERIMENTAL ANALYSIS OF THE EGP₁₀

No	Bottom layer	Middle layer	Upper layer	Outcome	Remarks
1	Material – fabric 100%. Coated with Gray paint (GP) – 100%	-----	-----	Voltage: 60-62 VDC Flexibility test - Semi-flexible Stress test – passed Waterproof- proved	Successfully run. Sample 1 drawback was solved, and 1 st Complete was successful. Process- One by one, layers 1 to 7 joined together. At that time, all layers were in semi-wet condition. The completely natural drying time was 3 days. The pad was very semi-hard and flexible. More flexibility will needed to improve the lifetime of the pad. Comments : The most preferable pad and will try to improve the pad's efficiency and flexibility. Remarks: This the same as EGP ₅ except Layer 7.
2	Material – fabric 100%. Coated with Gray paint (GP) – 100%	-----	-----		
3	-----	PZT with charge collector circuit The upper layer of PZT is coated with sticky black materials. PZT rails were connected Vertically	-----		
4	-----		Material – polyester micro fleece. Coated with a mixture of Grey paint (GP) 50%, Rubber Cement (RC) – 25%, and Flex -25%		
5	-----	-----	Material – fabric 100%. Coated with Gray paint (GP) – 100%		
6	-----	-----	Material – fabric 100%. Coated with Gray paint (GP) – 100%		
7	-----	-----	Material – fabric 100%. Coated with Gray paint (GP) – 100%		



Fig. 5.15 Prototype of the EGP₁₀.

5.3.11 Prototype 11: Sustainable Energy Generating Pad₁ (SEGP_{1X})

The Sustainable Energy Generating Pad₁ was developed based on the EGP₅ and EGP₁₀ and achieved a voltage output of 65-85 VDC, as shown in Fig. 5.16. This layer demonstrated semi-flexibility, passed the stress test, and proved to be waterproof, successfully running.



Fig. 5.16 Prototype of the SEGP_{1X}.

Table 5.4

EXPERIMENTAL ANALYSIS OF THE SEGP_{1X}

No	Bottom layer	Middle layer	Upper layer	Outcome	Remarks
1	Material – fabric 100%. Coated with Gray paint (GP) – 100%	-----	-----	Voltage: 65-85 VDC Flexibility test - Semi-flexible Stress test – passed Waterproof- proved	Successfully run. 1 st Generation EGP is developed called SEGP _{1X} .
2	Material – fabric 100%. Coated with Gray paint (GP) – 100%	-----	-----		
3	-----	PZT with charge collector circuit The upper layer of PZT is coated with sticky black materials. PZT rails were connected Vertically	-----		
4	-----		Material – 100% polyester micro fleece. Coated with a mixture of Grey paint (GP) 50%, Rubber Cement (RC) – 25%, and Flex -25%		
5	-----	-----	Material – fabric 100%. Coated with Gray paint (GP) – 100%		
6	-----	-----	Material – fabric 100%. Coated with Gray paint (GP) – 100%		
7	-----	-----	Material – fabric 100%. Coated with Gray paint (GP) – 100%		

The outcome led to the development of the 1st Generation EGP called SEGP_{1X}.

Layer 1 utilized 100% fabric coated with GP 100%. Layer 2 also utilized fabric 100%

coated with GP 100%. Layer 3 introduced PZT with a charge collector circuit, featuring an upper layer coated with sticky Black materials and vertically connected PZT rails. Layer 4 consisted of 100% polyester microfleece coated with a mixture of GP 50%, RC 25%, and Flex 25%. Layers 5, 6, and 7 all utilized fabric 100 % coated with GP 100%.

5.3.12 Prototype 12: Sustainable Energy Generating Pad₂ (SEGP_{2X})

The SEGP_{2X} involved the development of different layers with specific materials and coatings, resulting in the creation of the 2nd Generation EGP called SEGP_{2X}, which produced 2.2 times more electricity than SEGP_{1X}. This layer demonstrated solid flexibility hardness similar to tiles, passed the stress test, and proved to be waterproof, successfully running.



Fig. 5.17 Prototype of the SEGP_{2X}.

The outcome led to the development of the 2nd Generation EGP called SEGP_{2X}, as shown in Fig. 5.17. Layer 1 utilized 100% fabric coated with GP 100%, achieving a voltage output of 55-68 VDC, as described in Table 5.14. Layer 2 also utilized fabric 100% coated

with GP 100%. Layer 3 and Layer 4 both involved PZT with a charge collector circuit featuring an upper layer coated with sticky Black materials and vertically connected PZT rails. Layers 5 and 6 utilized fabric 100% coated with AP 100%.

TABLE 5.5

EXPERIMENTAL ANALYSIS OF THE SEGP_{2X}

No	Bottom layer	Middle layer	Upper layer	Outcome	Remarks
1	Material – fabric 100%. Coated with Gray paint (GP) – 100%	-----	-----	Voltage: 55-68VDC Flexibility test – Solid, Hard, like tiles Stress test – passed Waterproof- proved	Successfully run. 2 nd Generation EGP is developed called SEGP _{2X} , which is produced more 2.2-time electricity than SEGP _{1X}
2	Material – fabric 100%. Coated with Gray paint (GP) – 100%	-----	-----		
3	-----	PZT with charge collector circuit The upper layer of PZT is coated with sticky black materials. PZT rails were connected Vertically	-----		
4	-----	PZT with charge collector circuit The upper layer of PZT is coated with sticky black materials. PZT rails were connected Vertically	-----		
5	-----	-----	Material – fabric 100%. Coated with Ash paint (AP) – 100%		
6	-----	-----	Material – fabric 100%. Coated with Ash paint (AP) – 100%		

5.4 Failure Analysis of the SEGP_{1X} System

A destructive test and failure analysis were conducted on the SEGP_{1X}, revealing significant findings regarding its durability and performance under extreme conditions. The test subjected the SEGP_{1X} to high pressure, hard impacts, and twisting in order to assess its flexibility and durability. The results indicated that 30% of the PZT cells, out of a total of 18 cells, were damaged during the testing process, as shown in Fig. 5.18. This analysis underscores the importance of rigorous testing and evaluation in determining the robustness and reliability of energy generation pads like the SEGP_{1X}. The findings highlight areas for improvement, particularly in enhancing the pad's resistance to high pressure, hard impacts, and twisting motions to ensure greater flexibility and durability in real-world applications.



Fig. 5.18 Destructive Test and Failure Analysis on the SEGP_{1X}.

5.5 Prototype of Dual-Stage Charge Storage and Collection System

The Dual-Stage Charge and Collection System prototype has been developed in the lab to improve the efficiency of this system, especially all types of renewable or lower-watt energy generation systems, as shown in Fig. 5.19. In this research, two different experiments on lithium batteries were conducted by two companies chosen for the case

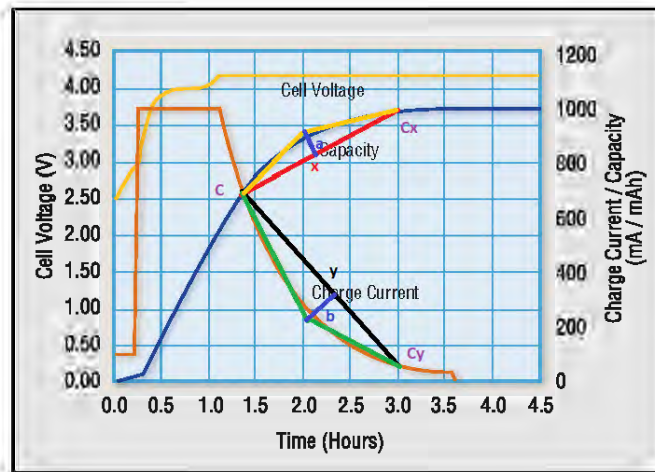


Fig. 5.21 Estimating the energy stored during the charging cycle of the Li-ion battery.

After analyzing Fig. 5.21, the following equations were developed to determine the stored energy in the Li-ion battery.

$$V = \frac{\sqrt{(Ycompofx)^2 + (Xcompofx)^2}}{\frac{a}{2}} \quad (5.1)$$

$$I = \frac{\sqrt{(Ycompofy)^2 + (Xcompofy)^2}}{\frac{b}{2}} \quad (5.2)$$

$$E = \{V \times I \text{ in the range of } (3 - 0.75)\} \text{ watts.hour} \quad (5.3)$$

$$E = (Vcomp \times Icomp) \text{ watts/hour} \quad (5.4)$$

V = Voltage, I = Current, V_{comp} = Comparison Value of Voltage, I_{comp} = Comparison value of Current, E = Store Energy in the Li-ion Battery.

Again, assuming the linearity by data points in Fig. 5.21,

$$V_{comp} = \frac{(3.7+3.35+2.62)}{3} = 3.223 \text{ V}(avg) \quad (5.5)$$

$$I_{comp} = \frac{(650+175+100)}{3} = 308.33 \text{ mA}(avg) \quad (5.6)$$

$$E = (3.223 \times 0.308) = 0.9934 \text{ Whr}(avg) \quad (5.7)$$

5.5.2 Case Study 2: Impact Analysis of 18650 Lithium-ion Battery

In this study, tests were done by Samsung and Toshiba companies on the type of 18650 lithium-ion batteries, and tested data is shown in Fig. 5.22. After analyzing the curve in Fig. 5.22, the charging voltage is higher (4.6 V) than the battery max settle Voltage (4.2 V) in the curve, which is very normal. This is set to max charging mode at the capacity of 100%. The SMART Center's SEGP is also set to charge at max energy from PZT cells. It also reduces the charging time significantly.

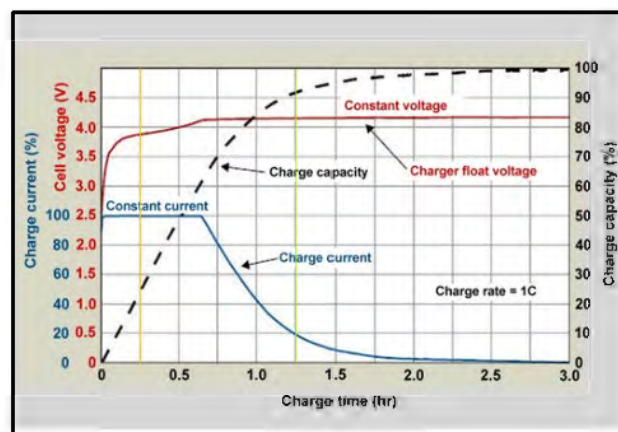


Fig. 5.22 Volts/capacity vs. time when charging lithium-ion.

5.6 Emulator Development of the SEGP System

An exciting technology has been developed to generate electricity using SEGPs. The potential for generating sustainable energy varies based on a cyclist's skill level [109]: Beginner Level: novice riders typically maintain speeds ranging from 8 to 12 mph, as shown in Fig. 5.23; while their contribution to electricity generation is present, it is modest due to their lower speeds. Intermediate Level: cyclists at the intermediate level maintain speeds ranging from 12 to 18 mph. Their proficiency in pedaling at moderate speeds significantly enhances their contribution to the sustainable energy source. Advanced Level:

advanced riders are capable of reaching speeds from 18 to 25 mph or even higher. This innovative technology promotes eco-friendliness while encouraging cyclists to push their limits, generating more electricity as they progress from one skill level to another. Additionally, to facilitate academic and research understanding of prototype SEGP technology on a test bench environment, an electronic module called the Sustainable Energy Harvesting Pad (SEHP) emulator has been developed, making it an invaluable tool for studying and advancing sustainable energy solutions. Addressing the data and results from the Prototypes of SEGP, the SEHP emulator with a 36Wh lithium-ion battery charging system has been developed. All emulators are developed in the following conceptual framework, as shown in Fig. 5.24.



Fig. 5.23 Analysis of Standard Adult bike with rider.

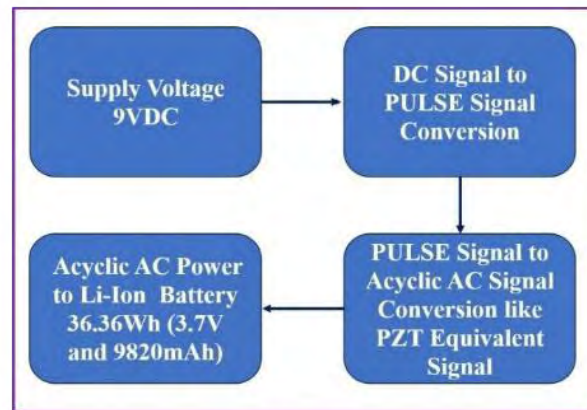


Fig. 5.24 The conceptual framework of the SEHP Emulator.

5.6.1 Design and Simulation of SEHP Emulator

The mathematical model for generating electricity for the SEHP for different levels of bike riders with constant weight, around 160lbs, including a bike with a bike rider, is expressed below:

$$P_{SEHP} = W \times D \times P \times Pl \times AP \quad (5.8)$$

Where,

P_{SEHP} = The power produced from SEHP (W/Sec), Wh= No of wheels (pcs), D= Average Distance (feet/sec), P= No of PZT cell, Pl= No of Pulse (pcs), and AP= Average power per Pulse.

TABLE 5.6

SEHP GENERATED POWER ANALYSIS BASED ON SPEED

<i>Biker Level</i>	<i>Speed (mph)</i>	<i>Wh (pcs)</i>	<i>D (feet/Sec)</i>	<i>P (pcs)</i>	<i>Pl (pcs)</i>	<i>AP (mW/Pulse)</i>	<i>P_{IXSEHP} (W/Sec)</i>
Beginner	8-12	2	14.6	6	2	14	4.9
Intermediate	12-18	2	20.5	6	2	14	6.8
Advanced	18-25	2	29.3	6	2	14	9.8

Based on the findings in Table 5.6, a novice cyclist with around 160 lbs consistent weight on a SEHP generates 4.9 Watts per second (W/Sec) for the beginner-level speed. An intermediate cyclist produces 6.8 W/Sec, while advanced riders reach 9.8 W/Sec. This data highlights the connection between skill level, speed, and power output for the same weight applied on the SEHP, which is vital for sustainable energy research and applications. Based on the SEGP experimental data, an electronic module called the SEHP emulator is designed and analyzed by using Proteus software, as shown in Fig. 5.25-5.26. In Fig. 5.26, the red signal represents the pulse signal, the blue signal is the output signal added to capacity, and the yellow signal is the charging signal on the Li-ion battery. The mathematical model for designing the SEHP Emulator for different levels of bike riders (around 160 lbs) is expressed below:

$$\text{Pulse} = \frac{1.44}{(R_1 + 2R_2) \times C} \quad (5.9)$$

$$D = \frac{T_1}{T} \quad (5.10)$$

Where,

Pulse= the no of time press on the SEGP (Hz), D= The duty cycle of the generating Pulse.

The SEHP emulator's simulation data are described in Table 5.7, considering three biker skill levels: beginner, intermediate, and advanced. The parameters include a consistent resistance of 1 k Ω (R_1), variable resistance levels (203.3 k Ω for beginners, 147 k Ω for intermediates, and 102.2 k Ω for advanced) as R_2 , a constant capacitance of 0.1 μ F (C), and increasing pulse frequency with skill level (354.024 Hz for beginners, 489.15 Hz

for intermediates, and 703.2 Hz for advanced). The duty cycle (D) remains relatively consistent at around 50%.

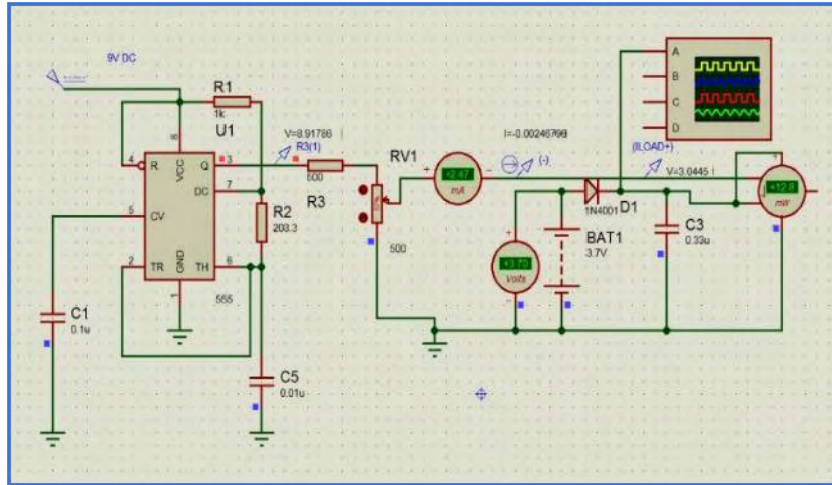


Fig. 5.25 Schematic of a SEHP Emulator.

TABLE 5.7

SEHP EMULATOR ANALYSIS

<i>Biker Level</i>	Beginner	Intermediate	Advanced
Speed (mph)	8-12	12-18	18-25
R ₁ (kΩ)	1	1	1
R ₁ (kΩ)	203.3	147	102.2
C (uF)	0.1	0.1	0.1
Pulse (Hz)	354.024	489.15	703.2
D ₁ (%)	50.1	50.1	50.2
Voltage (volt/Pulse)	3.7	3.7	3.7
Current (mA/Pulse)	2.47	2.47	2.47
P _{SEHP} (mW/Pulse)	12.8	12.8	12.8
TP _{SEHP} (W/Sec)	4.57	6.26	9.2
Li-ion Battery Voltage (V)	3.8	3.8	3.8
36Wh Battery Fully Charging time from SEGP (min)	131.2	95.8	65.2



Fig. 5.26 The Output Signal of a SEHP Emulator like SEGP.

Voltage and current per Pulse are constants at 3.7 V and 2.47 mA, respectively. Power per Pulse (P_{SEHP}) is consistent at 12.8 mW, while the total power per second (TP_{SEHP}) increases with skill level (4.57 W/Sec for beginners, 6.26 W/Sec for intermediates, and 9.2 W/Sec for advanced) for the same around 160 lbs. weight. A Li-ion battery voltage of 3.70 V and signal (yellow color in Fig. 5.26), the corresponding fully charging times from the SEHP are included for each skill level, 131.2 minutes for beginners, 95.8 minutes for intermediates, and 65.2 minutes for advanced, for 160 lbs of weight applied on the SEHP.

5.6.2 Prototype and Results of SEHP Emulator

Based on the SEHP emulator simulation, a SEHP prototype was developed in the lab with a 36Wh lithium battery, as shown in Fig. 5.27. The tested data are analyzed in Table 5.17. Furthermore, different levels of the SEHP signal are shown in Fig. 5.28-5.30. The SEHP emulator's Prototype data are presented in Table 5.8, focusing on three distinct biker skill levels: beginner, intermediate, and advanced. The key parameters encompass a

consistent resistance value of $1\text{ k}\Omega$ (R_1), variable resistance levels ($203.3\text{ k}\Omega$ for beginners, $147\text{ k}\Omega$ for intermediates, and $102.2\text{ k}\Omega$ for advanced) as R_2 and a constant capacitance of $0.1\text{ }\mu\text{F}$ (C). Pulse frequency increases with skill level (356.47 Hz for beginners, 485.15 Hz for intermediates, and 715 Hz for advanced).

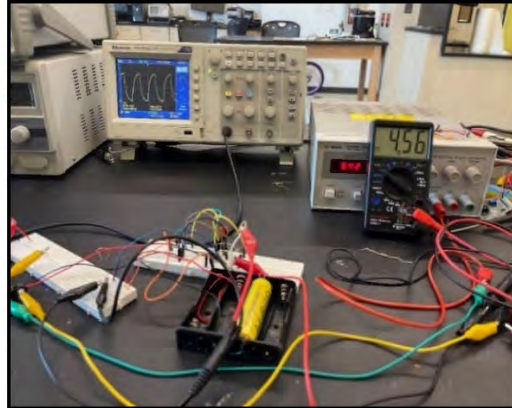


Fig. 5.27 Prototype of SEHP Emulator.

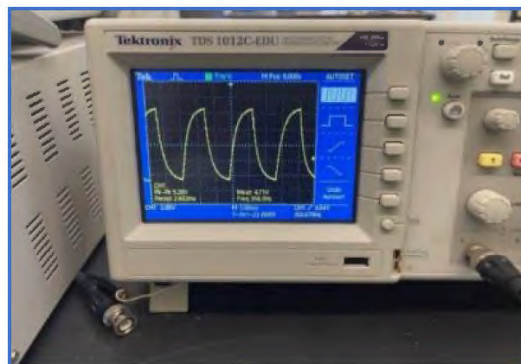


Fig. 5.28 Beginner level the SEHP Emulator Signal like SEGP.

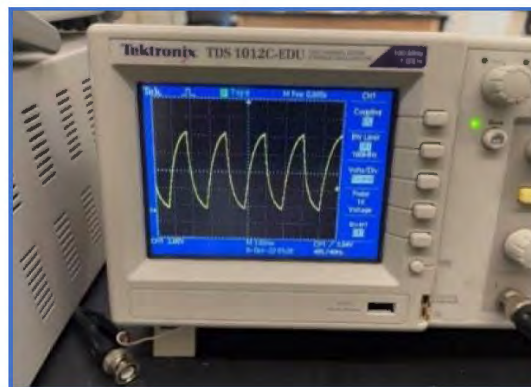


Fig. 5.29 Intermediate level of the SEHP Emulator Signal like SEGP.

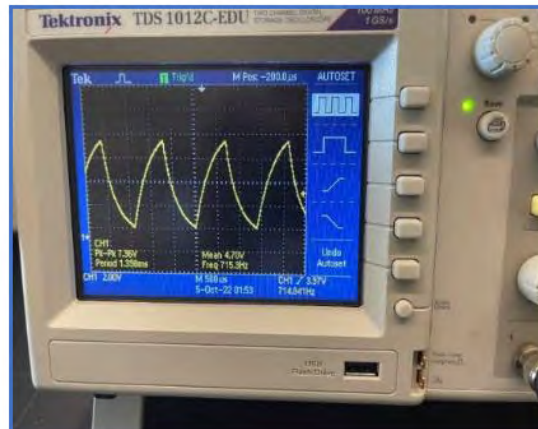


Fig. 5.30 Advanced level the SEHP Emulator Signal like SEGP.

The duty cycle (D) remains consistently at around 50%. Both the supply voltage and emulator output voltage are set at 9 volts, while the emulator output current is constant at 2.5 mA. P_{SEHP} is uniform at 11.75 mW, and the TP_{SEHP} exhibits an ascending trend with skill level (4.19, 5.71, & 8.41 W/Sec for beginners, intermediates, and advanced). A Li-ion battery voltage of 3.8 V and the corresponding full charging times from the SEHP are included for each skill level, 143 minutes for beginners, 105 minutes for intermediates, and 71.34 minutes for advanced.

TABLE 5.8
PROTOTYPE SEHP EMULATOR ANALYSIS

<i>Biker Level</i>	Beginner	Intermediate	Advanced
R_1 (k Ω)	1	1	1
R_1 (k Ω)	203.3	147	102.2
C (μ F)	0.1	0.1	0.1
Pulse (Hz)	356.47	485.15	715
D (%)	50.1	50.1	50.1
Supply Voltage (volt/Pulse)	9	9	9
Emulator Output Voltage (mA)	4.7	4.7	4.7
Emulator Output Current (mA)	2.5	2.5	2.5
P_{SEHP} (mW/Pulse)	11.75	11.75	11.75
TP_{SEHP} (W/Sec)	4.19	5.71	8.41
Li-ion Battery Voltage (V)	3.8	3.8	3.8
36Wh Battery Full Charging time from SEHP (min)	143	105	71.34

5.7 Summary

This chapter explored various prototypes and developments to advance sustainable energy generation technologies. It began with a prototype of a detailed analysis of PZT cells' characteristics through different layers. Additionally, the chapter delved into materials analysis for the development of EGP and presents a prototype of SEGP with varying specifications. Furthermore, the chapter included a comprehensive failure analysis of the SEGP system. It also discussed the development of a DSCS, an Emulator for the SEGP system. This chapter provides insights into cutting-edge technologies and methodologies to enhance energy generation sustainability, efficiency, and resilience.

CHAPTER 6

POTENTIAL APPLICATIONS & TECHNO-ECONOMIC ANALYSIS

This chapter explores various ways of utilizing and analyzing SEGP systems, focusing on innovative solutions such as combining SEGP technologies with existing PV system forms such as Hybrid (PV-SEGP) Grid-tie EWC Microgrid Systems. These microgrid systems' design and potential deployment locations are discussed, followed by an examination of how SEGPs are combined with solar panels and how they operate together. Furthermore, a system that utilizes solar power for rainwater purification is presented for water purification. The economic aspects of SEGPs and Hybrid Grid-tie EWC Microgrid Systems are analyzed to determine their cost-effectiveness and benefits. Stability analyses and case studies related to these grid-tie microgrid systems are also conducted [94]-[107].

6.1 Hybrid (PV-SEGP) Grid-tie EWC Microgrid System

A hybrid EWC grid-tie microgrid system using roadside is proposed for smart cities and rural communities. This system includes advanced features such as mobile and e-bike charging, rain/tap water purification, and a photovoltaic (PV) system on a roof. A SEGP is also designed to generate sustainable energy for bike lanes. A smart energy storage and management system has been developed to maximize the utilization of the energy generated from both the hybrid PV and SEGP systems, as illustrated in Fig. 6.1. A grid extension is also required to connect the system to a Utility grid. The EWC System has a 1-mile distance to assess a novel research initiative that employs a hybrid energy source. This project involves installing four 50 W_p PV panels, a total of 200 W_p panels on the

system's rooftop for two hubs, and laying out 1056 pieces of Sustainable Energy Generating Pads (SEGP) along the road's bike lane. Each unit of SEGP is 5 feet long and 4 feet wide. One thousand fifty-six units of SEGP will cover a distance of 5250 feet or 1 mile.

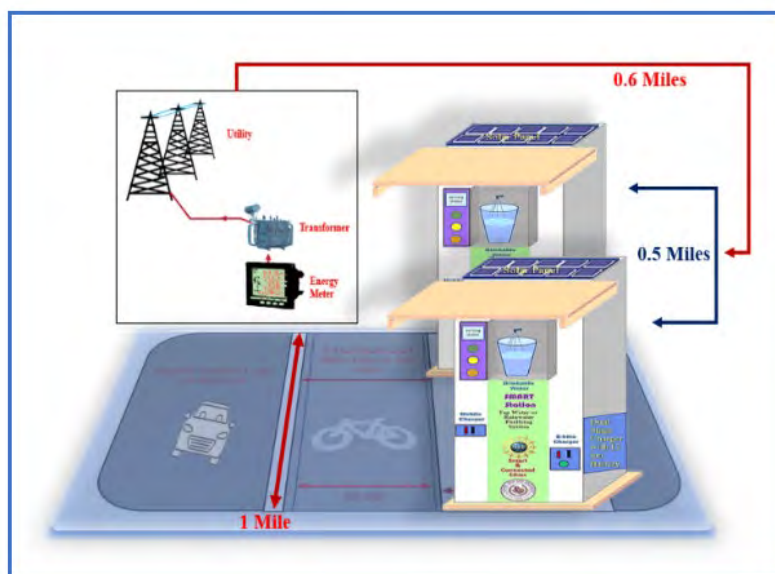


Fig. 6.1 Proposed Configuration of the EWC System

TABLE 6.1

PROPOSED EWC SYSTEM

Items	Hybrid EWC System	
	Capacity	Quantity
PV	50 W _p	4 panels
SEGP	5 feet	1056 PCs
e-Bike	300 Wh	2 PCs
Water Pump (DC)	48 Wh	2 PCs
Mobile	33.4 Wh	20 PCs
Pump for Water Purification	100 Wh	200 liter/day
1 st -stage Li-ion Battery	90W	2PCs
2 nd -stage Li-ion Battery	5 kW	2 PCs
Step-Up Transformer	5 kW	1 Pcs
Grid Extension	5 kW	1 Pcs

Table 6.1 shows the specifications of the EWC system, such as energy generating sources, storage, required loads, and their rating, capacity, and quantity. The system includes 200 W_p PV panels, 1-mile long SEGP, two e-bike chargers in two hubs (300 Wh each), ten mobile phone chargers for each station (16.7 Wh each), two water purification pump for two hubs (100 Wh for 200 liters/day), and two stages of Li-ion batteries (90W for the first stage and 5kW for the second stage) for two hubs as well to ensure reliability.

6.2 Proposed Site of the Hybrid PV-SEGP Grid-tie EWC Microgrid System

Prairie View A&M University, located at latitude 30.5.7 N and longitude 95.59.2 W, has been chosen as the site for resource data analysis and installing the SEGP system. Two EWC multifunctional stations are positioned along the route, with each station approximately 0.5 miles apart. The SEGP is integrated into the bike lanes starting from the main entrance of PVAMU and extending to the library, continuing to the University Village, covering a total distance of approximately 1 mile. A 0.6-mile grid extension also connects the SEGP system to the PVAMU Center Substations. This layout is depicted in Fig. 6.2, illustrating the seamless integration of the SEGP system along the specified route within the university campus. The site was chosen due to its strategic location within PVAMU, specifically the main entrance leading to the library and near the University Village. This area sees heavy foot traffic as it is frequented by students, faculty, and staff using e-bikes and regular bikes, especially those residing in the Prairie Dormitory and private residential areas close to the University Village. Texas, as a whole, is conducive to solar power systems like the SEGP due to its favorable environmental conditions.

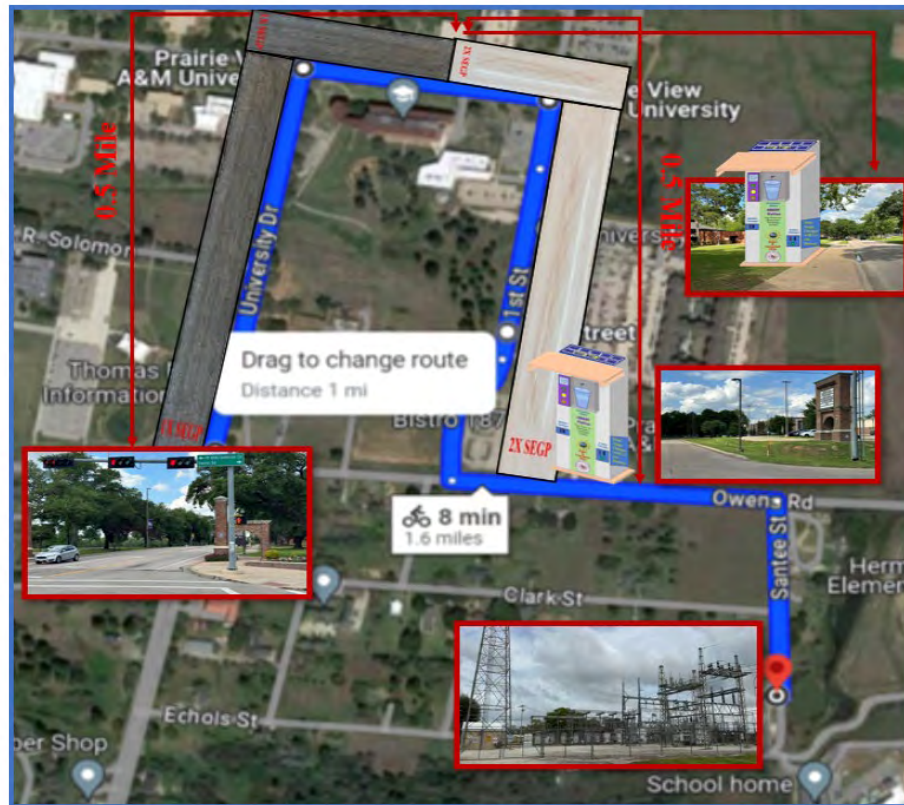


Fig. 6.2 Proposed Project Site at PVAMU.

According to NASA's solar radiation data, Texas receives an average of 5.6 kWh/m²/day of solar radiation, making it an excellent location for PV systems. The high usage of e-bikes and bikes within the campus community, the convenient location near key facilities and residential areas, and the favorable solar conditions in Texas make this site ideal for establishing the EWC system in Prairie View.

6.3 Design and Prototype of a Solar PV-Based Rainwater Purification System

A prototype portable solar-powered CRO rainwater filtration system was developed in the SMART Center at PVAMU, shown in Fig. 6.3. The system component specifications are shown in Table 6.2. The system had two solar panels, and each panel produced 30 W_p. The electricity produced was stored in a lithium-ion battery. The battery had a capacity of 12 volts and 10 A. The system had three water tanks. The tanks are a

rainwater collection tank, a fresh drinking water storage tank, and a water tank for pressure control. Two sensors were set up in the rainwater collection tank to sense and determine the water collection and level of water.

TABLE 6.2

THE PV-CRO SYSTEM COMPONENT SPECIFICATIONS

Items	Specifications	Quantity
1. Solar Panel	30 Wp	2 Pcs
2. Charge Controller	12 VDC and 20 Ah	1 Pcs
3. Battery	12 V and 10Ah	1 Pcs
4. Low Power Pump	12 VDC and 4Ah	1 Pcs
5. Relay Valve	12 VDC and 0.2-0.4 A	3 Pcs
6. Pressure Sensor	Range (0-60 psi)	1 Pcs
7. Water Sensor	Analog sensor	4 Pcs
8. Microcontroller	Arduino Nano	1 Pcs
9. Water Reservoir	1 Gallon	3 Pcs
10. PET Module	Range (0-30 psi)	1 Pcs
11. CRO Filter	Range (20-50 TDS)	1 Pcs
12. Transistor	Npn	4 Pcs
13. Resistor	10 Kohm	4 Pcs
14. Diode	1N4001	4 Pcs
15. Led	Blue	1 Pcs
16. Water Tap	-----	1 Pcs

Two other sensors were established in the drinking water tank to determine the water level and the pump's operation. A CRO filter was used to filter the rainwater into drinking water. A low-powered, high-pressure 12 VDC pump was used to complete the filtration process, and three control valves were used to control the water. A PET module was established to reduce the system pressure. A pressure sensor was established in the system to measure the system pressure. If the pressure of the system is higher than 55 psi, the microcontroller will stop the pump's operation. A coded program and an algorithm are developed for the system's microcontroller to collect the sensor's data, valves, and pump operations and make the system fully automated and contactless. This portable water

filtration system merges cutting-edge technology with a user-friendly design, ensuring safe, efficient, and continuous water purification even in off-grid scenarios.

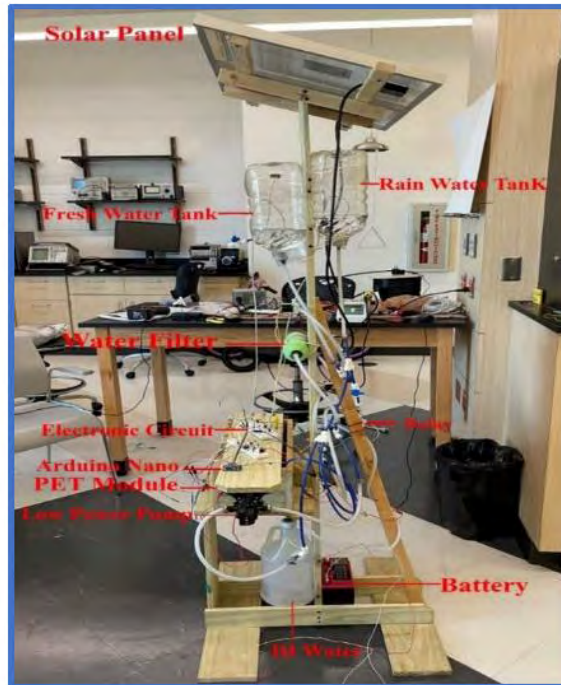


Fig. 6.3 The Prototype Portable Solar-powered CRO Rainwater Filtration System.

6.4 Prototype of SEGP System

The prototypes of 2 generations of SEGPs (SEGP_{1X} and SEGP_{2X}) are discussed in Chapters 5 and 7.

6.5 Economic Analysis of the SEGPs

The Tables comprehensively analyze the costs and components involved in the SEGP. The analysis covers pad specifications, gradient cladding, fabric, energy transport wire process, and the cost of preparation and installation, culminating in total and final costs per square foot, as described in Tables 6.3 to 6.6.

TABLE 6.3

COST ANALYSIS OF SEGPS (A).

SEGP						
Pad Width ft	Pad Length ft	Total Area sqft	# PZT/sqft	Total Pzt	Cost/PZT \$	Total \$
6	328	1968	36	70848	\$0.12	\$8,501.76
6	328	1968	36	70848	\$0.16	\$11,335.68
6	328	1968	36	70848	\$0.20	\$14,169.60
6	328	1968	36	70848	\$0.24	\$17,003.52

TABLE 6.4

COST ANALYSIS OF SEGPS (B).

Gradient Cladding					Fabric		
Liquid 1	Liquid #2	Liquid #3	Cost/gal \$	Total \$	Canvas	Felt	Cost \$
3	0.25	0.25	\$40.00	\$140.00	7,872	3,936	\$350.00
3	0.25	0.25	\$40.00	\$140.00	7,872	3,936	\$350.00
3	0.25	0.25	\$40.00	\$140.00	7,872	3,936	\$350.00
3	0.25	0.25	\$40.00	\$140.00	7,872	3,936	\$350.00

TABLE 6.5

COST ANALYSIS OF SEGPS (C).

Energy Transport Wire Process				Cost of Prep and Installation \$		
Mesh Wiring ft	IC Matrix	Solder Joints	Total Cost \$	Pad Prep	Testing	Deploy
1000	70848	425088	\$4,209.18	\$8,200.00	\$820.00	\$820.00
1000	70848	425088	\$4,209.18	\$8,200.00	\$820.00	\$820.00
1000	70848	425088	\$4,209.18	\$8,200.00	\$820.00	\$820.00
1000	70848	425088	\$4,209.18	\$8,200.00	\$820.00	\$820.00

TABLE 6.6

COST ANALYSIS OF SEGPS (D).

Total Cost/sqft			Final Summary Cost/sqft \$		
Pad	Prep/Deploy	Grand	Pad	Prep/Deploy	Complete \$
\$13,200.94	\$9,840.00	\$23,040.94	\$6.71	\$5.00	\$11.71
\$16,034.86	\$9,840.00	\$25,874.86	\$8.15	\$5.00	\$13.15
\$18,868.78	\$9,840.00	\$28,708.78	\$9.59	\$5.00	\$14.59
\$21,702.70	\$9,840.00	\$31,542.70	\$11.03	\$5.00	\$16.03

For a pad measuring 6 feet in width and 328 feet in length, covering a total area of 1968 square feet, the costs vary based on the cost per PZT, with the total PZT count remaining constant at 70,848. The cost breakdowns are as follows: \$8,501.76 for \$0.12 per PZT, \$11,335.68 for \$0.16 per PZT, \$14,169.60 for \$0.20 per PZT, and \$17,003.52 for \$0.24 per PZT. The gradient cladding component involves 3 units of Liquid 1, 0.25 units of Liquid #2, and 0.25 units of Liquid #3 at a cost of \$40 per gallon, totaling \$140. The fabric component includes 7,872 canvas and 3,936 units felt units, costing \$350.00 each. The energy transport wire process encompasses 1,000 feet of mesh wiring, 70,848 IC matrices, and 425,088 solder joints, totaling \$4,209.18. Consistent preparation and installation costs include \$8,200 for pad preparation, \$820 for testing, and \$820 for deployment. The total cost per square foot, combining both the pad and preparation/deployment, is \$23,040.94 for \$0.12 per PZT, \$25,874.86 for \$0.16 per PZT, \$28,708.78 for \$0.20 per PZT, and \$31,542.70 for \$0.24 per PZT. The final summary costs per square foot, combining pad and preparation/deployment costs, are \$11.71, \$13.15, \$14.59, and \$16.03, respectively. Based on the cost analysis, the first option stands out as the most cost-effective solution, with a cost per square foot of \$6.71 for the pad and a complete cost of \$11.71 per square foot. It offers significant savings while maintaining all necessary functionalities, making it the optimal choice for implementation.

6.6 Technoeconomic Analysis of Hybrid Grid-tie EWC Microgrid System

The techno-economic analysis of the EWC microgrid system is divided into two scenarios: the microgrid system and the grid-tie microgrid system.

6.6.1 Techno-economic Analysis of Islanded Microgrid-based Hybrid EWC System

The EWC microgrid system is proposed in a 1-mile distance location at the PVAMU Campus, where 2 multi-service hubs within a 0.5-mile distance with a PV system on the rooftop of these hubs, and both generations of SEGPs are established in the bike lane of the road in this selected 1-mile for the technical analysis. It is observed that the average solar radiation in Prairie View, Texas, is around 5.6 kWh/m²/day. It is assumed that around 200 bikes or e-bikes run an average of 2 hours per day at the University on weekdays, but the number of bikes or e-bikes is reduced by half during the weekends. So, the generation from the SEGP_{1X} and SEGP_{2X} are discussed in Table 6.7.

Energy generation from PV systems is discussed in the following equations:

$$P_{pv/day} = (Capacity_{pv} \times Avg \text{ Solar Radiation}) \quad (6.1)$$

$$P_{pv/year} = (P_{pv/day} \times 365) \quad (6.2)$$

$$TP_{pv/project} = \frac{\{P_{pv/year} \times Project \text{ life} \times (100 - \frac{degradation \ factor}{100})\}}{1000} \quad (6.3)$$

Where: $P_{pv/day}$ = Energy generation from PV system per day (Wh), $Capacity_{pv}$ = Total Capacity of the PV System (W_p), $P_{pv/year}$ = Energy generation from PV system per year (Wh), $TP_{pv/project}$ = The total project's energy generation from the PV system (kWh/project life) and the standard commercial PV panel degradation factor is 20% for 10 years.

Energy generation from SEGP_{1X} systems is discussed in the below equations:

$$P_{SEGP1X/bike} = (OP \times 3600) \times \frac{(S_{Bike} \times 1.46 \times 24 \times PP_{1X})}{3600} \quad (6.4)$$

$$P_{SEGP1X/day} = P_{SEGP1X/bike} \times N_b \quad (6.5)$$

$$P_{SEGP1X/year} = \{(5 \times P_{SEGP1X/day}) + P_{SEGP1X/day}\} \times 52 \quad (6.6)$$

$$TP_{SEGP1X/project} = \frac{\{P_{SEGP1X/year} \times Project\ life \times (100 - \frac{degradation\ factor}{100})\}}{1000} \quad (6.7)$$

Where: $P_{SEGP1X/bike}$ = Energy generation from SEGP_{1X} system per bike (Wh), OP = number of hour bike runs per day (hour), S_{Bike} = Speed of the running bike (mph), PP_{1X} = Energy generation per cell of the prototype SEGP_{1X} System (W), $P_{SEGP1X/day}$ = Energy generation from SEGP_{1X} system per day (Wh), N_b = number of bike runs per day (Pcs). $P_{SEGP1X/year}$ = Energy generation from the SEGP_{1X} system per year (Wh), $TP_{SEGP1X/project}$ = The total project's energy generation from the SEGP_{1X} system (kWh/project life) and the standard commercial PV panel degradation factor is 30% for 10 years.

Energy generation from SEGP_{1X} systems is discussed in the below equations:

$$P_{SEGP2X/bike} = (OP \times 3600) \times \frac{(S_{Bike} \times 1.46 \times 24 \times PP_{2X})}{3600} \quad (6.8)$$

$$P_{SEGP2X/day} = P_{SEGP2X/bike} \times N_b \quad (6.9)$$

$$P_{SEGP2X/year} = \{(5 \times P_{SEGP2X/day}) + P_{SEGP2X/day}\} \times 52 \quad (6.10)$$

$$TP_{SEGP2X/project} = \frac{\{P_{SEGP2X/year} \times Project\ life \times (100 - \frac{degradation\ factor}{100})\}}{1000} \quad (6.11)$$

Where: $P_{SEGP2X/bike}$ = Energy generation from SEGP_{2X} system per bike (Wh), PP_{2X} = Energy generation per cell of the prototype SEGP_{2X} System (W), $P_{SEGP2X/day}$ = Energy

generation from SEGP_{2X} system per day (Wh), $P_{SEGP_{2X}/year}$ = Energy generation from the SEGP_{2X} system per year (Wh), $TP_{SEGP_{2X}/project}$ = The total project's energy generation from the SEGP_{2X} system (kWh/project life) and the standard commercial PV panel degradation factor is 20% for 10 years.

TABLE 6.7

TECHNICAL ANALYSIS OF THE EWC MICROGRID SYSTEM

Sources	Quantity	Capacity (unit)	Total Capacity	Operation time	Total Generation
PV	4 PCs	50 W _p	200 W _p	5.6 hr/day	1120 Wh/day
SEGP _{1X}	1056 PCs	5 foot	5280 foot	2 hr/day	1962.24 Wh/day
SEGP _{2X}	1056 PCs	5 foot	5280 foot	2 hr/day	3083.52 Wh/day
Hybrid (PV & SEGP _{1X}) System Generation (kWh/day)					3.08
Hybrid (PV & SEGP _{2X}) System Generation (kWh/day)					4.20
Sources	Quantity	Capacity (unit)	Total Capacity	Round trip Efficiency	Total Usable
1 st Stage Li-ion Battery	2 PCs	18V, 90Wh	180 Wh	90%	162 Wh/day
2 nd -Stage Li-ion Battery	2 PCs	12V, 5000Wh	10000 Wh	95%	9500 Wh/day
Total Usable Energy from Hybrid (PV & SEGP _{1X}) System					2.68 kWh/day
Total Usable Energy from Hybrid (PV & SEGP _{2X}) System					3.57 kWh/day
Items	Quantity	Capacity (unit)	Total Capacity	Operation time (full charge)	Total Demand
e-Bike	2 PCs	300 Wh	600 Wh	1	0.60 kWh/day
Mobile	20 PCs	16.7 Wh	334 Wh	1	0.33 kWh/day
Water Pump	2 PCs	100 Wh	200 Wh	1	0.20 kWh/day
Total Energy Demand from the proposed system					1.13 kWh/day
Total Excess Energy from Hybrid (PV & SEGP _{1X}) System					1.55 kWh/day
Total Excess Energy from Hybrid (PV & SEGP _{2X}) System					2.44 kWh/day

The technical analysis of the EWC Microgrid System evaluates the energy generation and storage capabilities of a hybrid system, combining two scenarios: a Hybrid (PV and SEGP_{1X}) microgrid system and a Hybrid (PV and SEGP_{2X}) microgrid system. The PV system, with 4 panels of 50 W_p each, generates 1120 Wh/day. SEGP_{1X} and SEGP_{2X},

each with 1056 units covering 5280 feet or 1 mile, generate 1962.24 Wh/day and 3083.52 Wh/day, respectively. The hybrid systems produce 3.08 kWh/day (PV & SEGP_{1X}) and 4.20 kWh/day (PV & SEGP_{2X}). Energy storage is managed by Li-ion batteries, providing 180 Wh at 90 % efficiency and 10000 Wh at 95% efficiency, resulting in 2.68 kWh/day usable energy from the SEGP_{1X} hybrid and 3.57 kWh/day from the SEGP_{2X} hybrid. Daily energy demand includes 0.60 kWh for two e-bikes, 0.33 kWh for 20 mobile devices, and 0.20 kWh for two water pumps, totaling 1.13 kWh/day. This leaves an excess of 1.55 kWh/day from the SEGP_{1X} hybrid system and 2.44 kWh/day from the SEGP_{2X} hybrid system, as shown in Fig. 6.4, indicating a surplus of energy available for additional uses such as more e-bike charging and water purification. In the future, extensions of this system could supply the excess electricity to the Utility via a Grid-tie microgrid system.

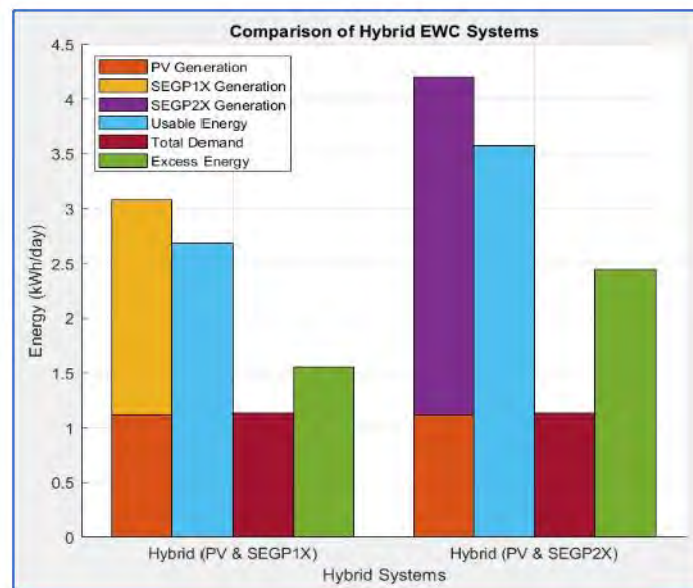


Fig. 6.4 Comparison of Hybrid EWC Microgrid System.

The project's life cycle assessment (LCA) is conducted by the following information and equations below:

The following information about this project is required to assess it. PL = Proposed project lifetime (year), FL = Financial loan (%), DP = Down payment (%), LP = Loan period (year), RC = Replacement cost (\$), CI = Compound Interest (%), PI = Possible inflation (%), OP = Overall expected profit (%), DR = Overall discount rate (%)

$$II_{PV} = CI_{PV} + PCC_{PV} + PBC_{PV} + CCC_{PV} \quad (6.12)$$

Where: II_{PV} = Initial Investment Cost for PV system (\$), CI_{PV} = Capital Investment for PV system (\$), PCC_{PV} = Power Conversion Cost for PV system (\$), PBC_{PV} = Plant Balancing Cost for PV system (\$), CCC_{PV} = Construction and Commissioning Cost for PV system (\$).

$$II_{SEGP1X} = CI_{SEGP1X} + PCC_{SEGP1X} + PBC_{SEGP1X} + CCC_{SEGP1X} \quad (6.13)$$

Where: II_{SEGP1X} = Initial Investment Cost for SEGP_{1X} system (\$), CI_{SEGP1X} = Capital Investment for SEGP_{1X} system (\$), PCC_{SEGP1X} = Power Conversion Cost for SEGP_{1X} system (\$), PBC_{SEGP1X} = Plant Balancing Cost for SEGP_{1X} system (\$), CCC_{SEGP1X} = Construction and Commissioning Cost for SEGP_{1X} system (\$).

$$II_{SEGP2X} = CI_{SEGP2X} + PCC_{SEGP2X} + PBC_{SEGP2X} + CCC_{SEGP2X} \quad (6.14)$$

Where: II_{SEGP2X} = Initial Investment Cost for SEGP_{2X} system (\$), CI_{SEGP2X} = Capital Investment for SEGP_{2X} system (\$), PCC_{SEGP2X} = Power Conversion Cost for SEGP_{2X} (\$), PBC_{SEGP2X} = Plant Balancing Cost for SEGP_{2X} system (\$), CCC_{SEGP1X} = Construction and Commissioning Cost for SEGP_{2X} system (\$).

$$II_{batt} = CI_{batt} + PCC_{batt} + PBC_{batt} + CCC_{batt} \quad (6.15)$$

Where: II_{batt} = Initial Investment Cost for battery system (\$), CI_{batt} = Capital Investment for battery system (\$), PCC_{batt} = Power Conversion Cost for battery system(\$), PBC_{batt} = Plant Balancing Cost for battery system (\$), CCC_{SEGP1X} = Construction and Commissioning Cost for battery system (\$).

$$BL = \frac{LC_{BT} \times C_B \times \frac{RT_E}{100}}{GH_{EWC/year}} \quad (6.16)$$

Where: BL = Battery lifetime (year), LC_{BT} = Life cycle of the Battery, C_B = Capacity of the Battery (kW), RT_E = Round trip efficiency of the batteries (%), $GH_{EWC/year}$ = Generation of Hybrid EWC Energy per year (kWh).

$$II_{conv} = CI_{conv} + PCC_{conv} + PBC_{conv} + CCC_{cov} \quad (6.17)$$

Where: II_{cov} = Initial Investment Cost for conversion system (\$), CI_{conv} = Capital Investment for conversion system (\$), PCC_{conv} = Power Conversion Cost for conversion system (\$), PBC_{conv} = Plant Balancing Cost for conversion system (\$), CCC_{conv} = Construction and Commissioning Cost for battery system (\$).

$$II_{wp} = CI_{wp} + PCC_{wp} + PBC_{wp} + CCC_{wp} \quad (6.18)$$

Where: II_{wp} = Initial Investment Cost for water purification (\$), CI_{wp} = Capital Investment for water purification (\$), PCC_{wp} = Power Conversion Cost for water purification (\$), PBC_{wp} = Plant Balancing Cost for water purification (\$), CCC_{wp} = Construction and Commissioning Cost for water purification (\$).

$$II_{utility} = CI_u + PCC_u + PBC_u + CCC_u \quad (6.19)$$

Where: $II_{utility}$ = Initial Investment Cost for Utility (\$), CI_u = Capital Investment for Utility (\$), PCC_u = Power Conversion Cost for Utility (\$), PBC_u = Plant Balancing Cost for Utility (\$), CCC_u = Construction and Commissioning Cost for Utility (\$).

$$TII_1 = \sum II \quad (6.20)$$

$$TII_2 = \sum II \quad (6.21)$$

Where: TII_1 = Total project's initial investment for Hybrid (PV & SEGP_{1X}) system (\$), TII_2 = Total project's initial investment for Hybrid (PV & SEGP_{2X}) system (\$), $\sum II$ = Summation of all sources of initial investment of the project (\$)

$$FLA_1 = TII_1 \times \frac{FL}{100} \quad (6.22)$$

$$FLA_2 = TII_2 \times \frac{FL}{100} \quad (6.23)$$

Where: FLA_1 = Total financial loan amount for Hybrid (PV & SEGP_{1X}) system (\$), FLA_2 = Total financial loan amount for Hybrid (PV & SEGP_{2X}) system (\$),

$$TRC = \sum \left\{ RC_{Sources} \times \left(\frac{PL}{Lifetime_{Sources}} \right) \right\} \quad (6.24)$$

Where: TRC = Total replacement cost (\$), $RC_{Sources}$ = Replacement cost for all sources (\$), $Lifetime_{Sources}$ = Lifetime of all sources (\$).

$$TOM = [\sum (OM_{Sources} + MC_{Sources})] \times (PL) \quad (6.25)$$

Where: TOM = Total operational and maintenance cost replacement cost (\$), $OM_{Sources}$ = Operation and maintenance cost per year for all sources (\$), $MC_{Sources}$ = Miscellaneous cost per year for all sources (\$).

$$TCP = \left[(TII + TOM + TMC) + \left\{ \left(FLA \times \left(1 + \frac{CL}{100} \right)^{LP} \right) \right\} + \left\{ (TII + TOM + TMC) \times \frac{PI}{100} \right\} \right] \quad (6.26)$$

Where: TCP = Total cost of the project (\$).

$$LCOE = \frac{TCP}{TUE_{EWC}} \quad (6.27)$$

Where: LCOE = Total levelized energy cost per kWh of the project (\$), TUE_{EWC} = Total usable energy from the EWC.

$$EPP = TCP \times \frac{OP}{100} \quad (6.28)$$

Where: EPP = Estimated overall project profit (\$).

$$ROI_F = \frac{TCP}{Revenue_{selling} \times 365} \quad (6.29)$$

$$ROI_D = \frac{TCP}{Revenue_{selling} \times \frac{DR}{100} \times 365} \quad (6.30)$$

Where: ROI_F = Return on investment on flat selling rate (year), ROI_D = Return on investment on discount selling rate (year).

The economic analysis is conducted based on equations 6.1 - 6.31, as written above, described in Tables 6.8 & 6.9. The EWC Microgrid System evaluates various components, including the Hybrid₁ (PV & SEGP_{1X}) System and Hybrid₂ (PV & SEGP_{2X}) System, the CRO system, and different stages of Li-ion batteries along with a dual-stage charging system. Each component is assessed for its capacity, lifetime, capital costs, annual

operation and maintenance (O&M) costs, replacement costs, and miscellaneous expenses. The overall project analysis for the Hybrid EWC Microgrid System over a 10-year time frame at PVAMU Campus, Texas, USA, includes several key economic and operational metrics.

TABLE 6.8

ECONOMICAL ANALYSIS OF THE EWC MICROGRID SYSTEM

Items	PV	SEGP _{1X}	SEGP _{2X}	CRO System	1 st -stage Li-ion Battery	2 nd -stage Li-ion Battery	Dual-Stage Charging System
Capacity	200 W _p	5280 foot long	5280 foot long	2PCs	18V, 180Wh	12V, 10kWh	2 Pcs
Lifetime	20 year	5 year	5 year	10 year	3 year	5 year	10 year
Capital	\$1000	\$31680	\$26400	\$500	\$30	\$2000	\$100
PCC	\$0	\$0	\$0	\$0	\$0	\$0	\$0
PBC	\$0	\$0	\$0	\$0	\$0	\$0	\$0
CCC	\$1000	\$5000	\$5000	\$500	\$20	\$100	\$50
O&M	\$10/year	\$200/year	\$200/year	\$100/year	\$0	\$0	\$0
Replacement	0	\$25000	\$20000	\$0	\$60	\$1600	\$0
Miscellaneous	\$10/year	\$100/year	\$100/year	\$100/year	\$0	\$0	\$0
Total Cost	\$2200	\$64680	\$54400	\$3000	\$130	\$3700	\$100

The project is funded through a 70% loan with a 6.5% compound interest rate and considers a possible inflation rate of 4% and a discount rate of 15%. Total initial investment (TII) for both systems scenarios (EWC₁ and EWC₂) are \$73,810 and \$63,530, respectively, while the total cost of the projects (TCP₁ & TCP₂) are \$173,896.36 for EWC₁ and \$149,676.68 for EWC₂. Over ten years, EWC₁ and EWC₂ will produce 7336.5 kWh and 10424.4 kWh of usable energy, respectively, and purify a total of 1,460,000 liters of water. The LCOE for EWC₁ is \$23.70/kWh and \$14.36/kWh for EWC₂. Water purification costs are \$0.011/liter for EWC₁ and \$0.008/liter for EWC₂. E-bike charging costs from EWC₁

and EWC_2 are \$6.95 and \$4.24 per e-bike, respectively, while mobile charging costs are \$0.39/mobile for EWC_1 and \$0.24/mobile for EWC_2 .

TABLE 6.9

OVERALL PROJECT ANALYSIS FOR HYBRID EWC MICROGRID SYSTEM

Project Time Frame	10 years		
Project Location	PVAMU Campus, Texas, USA		
Project Loan	70%		
Compound Interest	6.5 %		
Load Period	10 years		
Possible Inflation	4%		
Discount Rate	15%		
TII_1	\$73810		
TII_2	\$63530		
TCP_1	\$173896.36		
TCP_2	\$149676.68		
Production	Day	Year	10 Year
Usable EWC Energy ₁	2.68 kWh	978.2 kWh	7336.5 kWh
Usable EWC Energy ₂	3.57 kWh	1303.05 kWh	10424.4 kWh
Total Water Purification	400 liter	146000 liter	1460000 liter
$LCOE_1$	\$23.70/kWh		
$LCOE_2$	\$14.36/kWh		
Water Purification Cost from EWC_1	\$0.011/liter		
Water Purification Cost from EWC_2	\$0.008/liter		
e-bike Charging Cost from EWC_1	\$6.95/e-bike		
e-bike Charging Cost from EWC_2	\$4.24/e-bike		
Mobile Charging Cost from EWC_1	\$0.39/mobile		
Mobile Charging Cost from EWC_2	\$0.24/mobile		
Consumer	Selling Price	Total Revenue	
e-bike Charging (4/day)	\$2.00/e-bike	\$29200	
Mobile Charging (20/day)	\$0.25/mobile	\$18250	
Drinking Water (400L/day)	\$0.25/liter	\$365000	
Total Revenue of The Hybrid EWC System	\$412450		
ROI_F for EWC_1	4.22 year		
ROI_D for EWC_1	4.95 year		
ROI_F for EWC_2	3.63 year		
ROI_D for EWC_2	4.27 year		

The total revenue generated from e-bike charging (\$2.00/e-bike, 4/day), mobile charging (\$0.25/mobile, 20/day), and drinking water sales (\$0.25/liter, 400 L/day) amounts to \$412,450 over the project duration. The ROI for EWC₁ is 4.24 years (fixed rate) and 4.95 years (discounted rate), while for EWC₂, it is 3.63 years (fixed) and 4.27 years (discounted). This comprehensive analysis highlights the financial viability and sustainability of the hybrid EWC microgrid system, emphasizing its capacity to generate substantial revenue and achieve a favorable ROI within the projected time frame.

6.6.2 Techno-economic Analysis of Grid-tie Microgrid-based Hybrid EWC System

The extension of this proposed EWC microgrid system has been upgraded to a grid-tie EWC microgrid system by a 0.6-mile extension to the EWC microgrid system with the exact 1-mile location connected to the PVAMU's central utility substation at the PAMU. The main purpose of this upgrade of the EWC microgrid system is to sell the excess electricity to the Utility. The detailed technical analysis of the grid-tie microgrid system is described in Table 6.10.

Available excess energy from Hybrid systems is discussed in the following equations:

$$UP_{HP/day} = (EE_H \times \frac{IE}{100} \times \frac{TE}{100}) \quad (6.31)$$

Where: $UP_{HP/day}$ = Available Energy in the Utility from the EWC system per day (kWh), EE_H = Excess Electricity from the EWC Hybrid System, IE = Inverter efficiency (%), TE = Transformer efficiency (%). The standard efficiency of the on-grid inverter available is around 90%, and that of the transformer is around 95%.

TABLE 6.10

TECHNICAL ANALYSIS OF THE GRID-TIE EWC MICROGRID SYSTEM

Sources	Quantity	Capacity (unit)	Total Capacity
Inverter	1 PCs	5 kW	5 kW
Grid Extension	1 PCs	0.6 mile	0.6 mile
Step Up Transformer	1 PCs	5 kW	5 kW
Utility	1 PCs	5 kW	5 kW
Electricity Supply to the Utility from Hybrid (PV & SEGP _{1X}) System			1.33 kWh/day
Electricity Supply to the Utility from Hybrid (PV & SEGP _{2X}) System			2.09 kWh/day

Fig. 6.5 and Table 6.10 present a technical analysis of the Grid-tie EWC microgrid System, specifying its components and their respective capacities. The system features one inverter with a capacity of 5 kW, a grid extension measuring 0.6 miles, and a utility component also rated at 5 kW. Additionally, the system includes hybrid energy sources, with the Hybrid (PV & SEGP_{1X}) system supplying 1.33 kWh/day to the utility and the Hybrid (PV & SEGP_{2X}) system contributing 2.09 kWh/day. This analysis highlights the microgrid's capacity to integrate renewable energy sources efficiently and supply electricity to the Utility. Table 6.11 discussed the economic analysis of the EWC grid-tie microgrid system for a 5 kW capacity over a 10-year lifetime, revealing a total cost of \$28,000. The capital investment required is \$10,000, covering essential components such as cable extensions and switchgear.

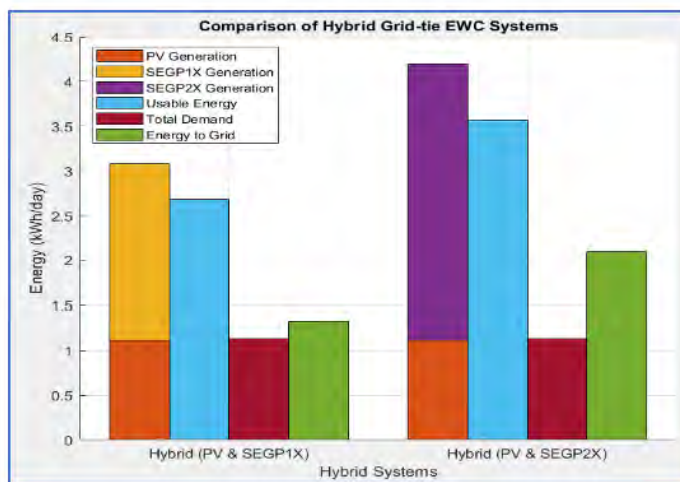


Fig. 6.5 Comparison of Hybrid Grid-tie EWC Microgrid System.

The system incurs additional costs of \$2,000 for PCC (inverter), \$5,000 for PBC (transformer), and \$5,000 for CCC. Annual operation and maintenance (O&M) expenses are estimated at \$500, with miscellaneous costs adding \$100 annually. Notably, no replacement costs are required for the 10-year project in this analysis. The overall project analysis for the hybrid grid-tie EWC microgrid system compares EWC_{g1} and EWC_{g2} configurations described in Table 6.12. The total initial investment (TII) is \$101,810 for EWC_{g1} and \$91,530 for EWC_{g2}, while the total grid-tie system capital costs (TCP₁ & TCP₂) are \$239,853.08 and \$215,644.68, respectively.

TABLE 6.11

ECONOMICAL ANALYSIS OF THE EWC GRID-TIE MICROGRID SYSTEM

Items	Utility
Capacity	5 kW
Lifetime	10 year
Capital	\$10000
PCC	\$2000
PBC	\$2000
CCC	\$5000

O&M	\$500/year
Replacement	0
Miscellaneous	\$100/year
Total Cost	\$28000

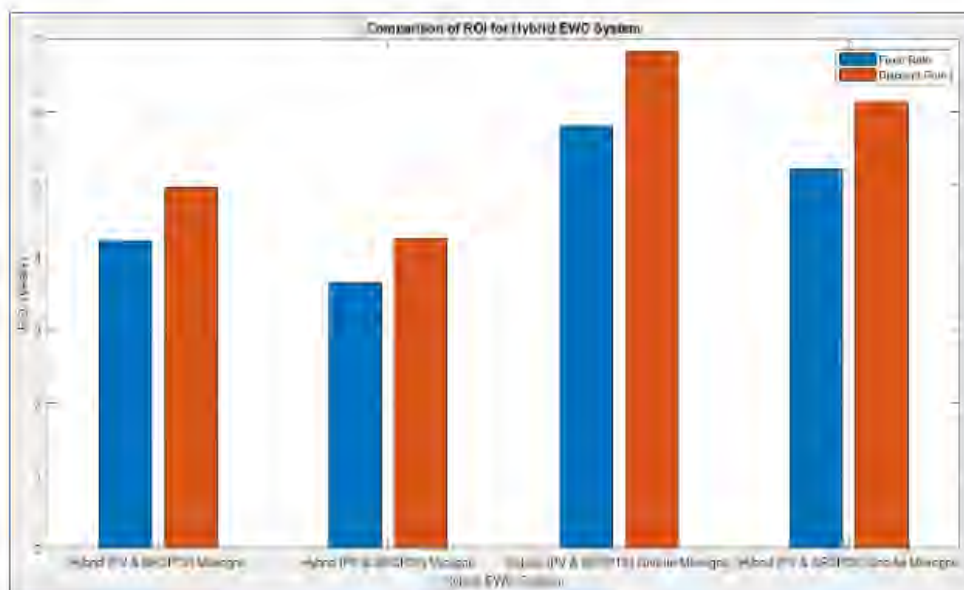


Fig. 6.6 Overall System's ROI Comparison.

The LCOE is significantly different between the two, with EWC_{g1} at \$32.69/kWh and EWC_{g2} at \$20.68/kWh. Revenue from selling excess energy is 0.146/kWh to the Utility is \$708.76 for EWC_{g1} and \$1,113.76 for EWC_{g2} , contributing to total revenues of \$413,158.76 and \$413,563.76, respectively. The ROI is evaluated both on a fixed rate and discounted rate, showing EWC_{g1} with an ROI_F of 5.80 years and ROI_D of 6.83 years, while EWC_{g2} shows a more favorable ROI_F of 5.21 years and ROI_D of 6.13 years, as shown in Figure 6.6.

TABLE 6.12
OVERALL PROJECT ANALYSIS FOR HYBRID GRID-TIE EWC MICROGRID
SYSTEM

TII_{g1}	\$101810	
TII_{g2}	\$91530	
TCP_{g1}	\$239853.08	
TCP_{g2}	\$215644.68	
$LCOE_{g1}$	\$32.69/kWh	
$LCOE_{g2}$	\$20.68/kWh	
Consumer	Selling Price	Total Revenue
Excess energy to utility _{g1}	\$0.146/kWh	\$708.76
Excess energy to utility _{g2}	\$0.146/kWh	\$1113.76
Total Revenue of The Hybrid Grid-tie EWC ₁ System	\$413158.76	
Total Revenue of The Hybrid Grid-tie EWC ₂ System	\$413563.76	
ROI_F for EWC _{g1}	5.80 year	
ROI_D for EWC _{g1}	6.83 year	
ROI_F for EWC _{g2}	5.21 year	
ROI_D for EWC _{g2}	6.13 year	

6.7 Stability Analysis of Grid-Tie Hybrid EWC Microgrid System

An IEEE 15-bus AC-DC EWC microgrid system is designed using Etap software, as shown in Fig. 6.7. The system consists of two energy-generating stations (EWC Station 1 and EWC Station 2), various DC and AC busbars, converters, inverters, and AC and DC loads. EWC System 1 consists of a 1X-SEGP 1 energy-generating swing source with an output voltage of 0.11 kV and a generated power of 1.54 kW. This output is connected to AC to DC charger 1, which converts 0.11 kV to 24V and forwards it to DC busbar 1 (24V rating). DC busbar 1 transfers energy to DC busbar 2 through DC circuit breaker 18. DC

busbar 2 is connected to an 18.5V, 90Wh 1st-stage battery, where the energy is stored. Once the battery is fully charged from the 1X-SEGP 1 generated energy, it transfers energy to DC busbar 3 through DC-to-DC converter 2, which converts 18V to 12V. DC busbar 3 stores energy in a 12V Main storage battery rated at 5 kW. DC busbar 3 is connected to DC busbar 4 through DC circuit breaker 16, maintaining a voltage of 12V. A PV source (PV 1) with a rating of 100Wp produces 38.5V and is connected to a DC-DC converter 1, which converts 40V to 12V, transferring the PV energy to DC busbar 4. DC busbar 4 serves as the combined connection point for all sources in EWC System 1. EWC System 2 consists of a 2X-SEGP 2 energy-generating swing source with an output voltage of 0.11 kV and a generated power of 2.20 kW. This output is connected to AC to DC charger 2, which converts 0.11 kV to 24V and forwards it to DC busbar 5 (24V rating). DC busbar 5 transfers energy to DC busbar 6 through DC circuit breaker 25. DC busbar 6 is connected to an 18.5V, 90Wh 1st-stage battery, where the energy is stored. Once the battery is fully charged from the 2X-SEGP2 generated energy, it transfers energy to DC busbar 7 through DC-to-DC converter 4, which converts 18V to 12V. DC busbar 7 stores energy in a 12V Main storage battery rated at 5 kW. DC busbar 7 is connected to DC busbar 8 through DC circuit breaker 26, maintaining a voltage of 12V. A PV source (PV 2) with a rating of 100Wp produces 38.5V and is connected to a DC-DC converter 3, which converts 40V to 12V, transferring the PV energy to DC busbar 8. DC busbar 8 serves as the combined connection point for all sources in EWC Station 2. The two EWC stations are connected through a DC busbar network. DC busbar 4 (from EWC 1) and DC busbar 8 (from EWC 2) are connected to DC busbar 9, which is located 0.25 miles between them, a total of 0.5 miles, and connected via cable 9 and cable 28, forming a complete microgrid system. The Hybrid

EWC microgrid system has been updated to a Grid-tie microgrid system with a 0.6-mile extension from the DC busbar 9 to connect to the utility. As a result, it forms an IEEE 15 bus AC-DC Hybrid Microgrid System. The extension consists of an inverter, cable, step-up transformer, switchgear, and utility connection. Inverter 3 is connected to DC busbar 9 and converts 12 V DC energy to 110 V AC energy, which is then connected to AC Busbar 5 through a 0.6-mile cable (cable 9). AC busbar 5 is linked to AC Busbar 6 via switchgear and a step-up transformer (T3) with a rating of 0.11/11 kV, 10 KVA. AC Bus 6 is connected to the substation for utility purposes. DC Busbar 4 Connected to a Water Pump1 (12V, 0.03HP) as a DC load. It also connects to a DC to AC Inverter 1, which converts 12V to 0.11kV and connects to AC Busbar 1 (0.11 kV rating). AC Busbar 1 is connected to Phone Charger 4 (0.11 kV, 60 VA). AC Busbar 3 via cable 17. AC Busbar 3 is connected to e-bike charger 1 (0.11 kV, 250 VA). DC Busbar 8: Connected to a Water Pump 2 (12 V, 0.03 HP) as a DC load. It also connects to a DC to AC Inverter 2, which converts 12 V to 0.11 kV and connects to AC Busbar 2 (0.11 kV rating). AC Busbar 2 is connected to Phone Charger 2 (0.11 kV, 120 VA). AC Busbar 4 via cable 24. AC Busbar 4 is connected to e-bike charger 2 (0.11 kV, 300 VA). This configuration ensures efficient energy distribution and utilization across the microgrid, effectively supporting various loads and energy storage components. Following this setup, the following case studies (6.7.1-6.7.2) are conducted to determine the stability of the grid-tied Hybrid EWC microgrid system: unbalanced load flow and voltage stability. The complete system is analyzed by the following equations below:

The bus admittance matrix Y_{bus} is constructed using the impedance values of the transmission lines. Each element of Y_{bus} is given by:

$$Y_{ij} = \begin{cases} \sum_{k \neq i} \frac{1}{Z_{ik}} & \text{if } i = j \\ -\frac{1}{Z_{ij}} & \text{if } i \neq j \end{cases} \quad (6.32)$$

Here, Z_{ij} is the impedance between buses i and j .

AC Power Flow Equations: The power flow equations for each bus i in an AC network are:

$$P_i = V_i \sum_{j=1}^n V_j (G_{ij} \cos \theta_{ij} + B_{ij} \sin \theta_{ij}) \quad (6.33)$$

$$Q_i = V_i \sum_{j=1}^n V_j (G_{ij} \sin \theta_{ij} - B_{ij} \cos \theta_{ij}) \quad (6.34)$$

where:

- P_i and Q_i are the active and reactive power injections at bus i , respectively.
- V_i and V_j are the voltage magnitudes at bus i and j , respectively.
- G_{ij} and B_{ij} are the conductance and susceptance between buses i and j .
- θ_{ij} is the voltage angle difference between buses i and j .

DC Load Flow Analysis: The DC power flow equation for bus i is given by:

$$P_{iDC} = V_{iDC} \sum_{j=1}^n V_{jDC} \frac{1}{R_{ij}} \quad (6.35)$$

where:

- P_{iDC} is the active power injection at bus i in the DC system.
- V_{iDC} and V_{jDC} are the voltage magnitudes at bus i and j in the DC system.
- R_{ij} is the resistance between buses i and j in the DC system.

For each DC bus i :

$$\text{DCPowerBalance: } P_{DC,i} = V_{DC,i} \sum_{j=1}^m (V_{DC,j} G_{DC,ij}) \quad (6.36)$$

where $G_{DC,ij}$ is the conductance between DC buses i and j .

For each converter k connecting AC bus i and DC bus j :

$$\text{PowerBalance: } P_{AC,i} = \eta_k P_{DC,j} \quad (6.37)$$

where η_k is the efficiency of the converter.

The Jacobian matrix J is composed of four submatrices:

$$J = \begin{bmatrix} J_{11} & J_{12} \\ J_{21} & J_{22} \end{bmatrix} \quad (6.38)$$

where:

$$J_{11} = \frac{\partial P}{\partial \theta} \quad J_{12} = \frac{\partial P}{\partial V} \quad (6.39)$$

$$J_{21} = \frac{\partial Q}{\partial \theta} \quad J_{22} = \frac{\partial Q}{\partial V} \quad (6.40)$$

Elements of J_{11} :

$$\frac{\partial P_i}{\partial \theta_j} = \begin{cases} -V_i V_j (G_{ij} \sin \theta_{ij} - B_{ij} \cos \theta_{ij}), & i \neq j \\ V_i \sum_{k=1}^n V_k (G_{ik} \sin \theta_{ik} - B_{ik} \cos \theta_{ik}), & i = j \end{cases} \quad (6.41)$$

Elements of J_{12} :

$$\frac{\partial P_i}{\partial V_j} = \begin{cases} V_i (G_{ij} \cos \theta_{ij} + B_{ij} \sin \theta_{ij}), & i \neq j \\ \sum_{k=1}^n V_k (G_{ik} \cos \theta_{ik} + B_{ik} \sin \theta_{ik}) + 2G_{ii} V_i, & i = j \end{cases} \quad (6.42)$$

Elements of J_{21} :

$$\frac{\partial Q_i}{\partial \theta_j} = \begin{cases} -V_i V_j (G_{ij} \cos \theta_{ij} + B_{ij} \sin \theta_{ij}), & i \neq j \\ -\sum_{k=1}^n V_i V_k (G_{ik} \cos \theta_{ik} + B_{ik} \sin \theta_{ik}), & i = j \end{cases} \quad (6.43)$$

Elements of J_{22} :

$$\frac{\partial Q_i}{\partial V_j} = \begin{cases} V_i (G_{ij} \sin \theta_{ij} - B_{ij} \cos \theta_{ij}), & i \neq j \\ \left(\sum_{k=1}^n V_k (G_{ik} \sin \theta_{ik} - B_{ik} \cos \theta_{ik}) - 2B_{ii} V_i \right), & i = j \end{cases} \quad (6.44)$$

The Jacobian matrix J for the Newton-Raphson method in an AC/DC microgrid combines both AC and DC power flow equations:

$$J = \begin{bmatrix} \frac{\partial P_i}{\partial V_i} & \frac{\partial P_i}{\partial \theta_i} & 0 & 0 \\ \frac{\partial Q_i}{\partial V_i} & \frac{\partial Q_i}{\partial \theta_i} & 0 & 0 \\ 0 & 0 & \frac{\partial P_{DC,i}}{\partial V_{DC,i}} & 0 \\ 0 & 0 & 0 & \frac{\partial P_{DC,j}}{\partial P_{AC,i}} \end{bmatrix} \quad (6.45)$$

The Newton-Raphson method is commonly used to solve the non-linear power flow equations. The iterative solution involves:

$$\begin{bmatrix} \Delta P \\ \Delta Q \end{bmatrix} = J^{-1} \begin{bmatrix} P_{\text{mismatch}} \\ Q_{\text{mismatch}} \end{bmatrix} \quad (6.46)$$

Where: J is the Jacobian matrix of partial derivatives of the power flow equations.

The Newton-Raphson method is used for unbalanced load flow analysis. The iterative steps are as follows:

1. Initialize bus voltages and angles (V and θ).
2. Calculate the mismatch in active and reactive power (P_{mismatch} and Q_{mismatch}).

3. Formulate the Jacobian matrix (J) of partial derivatives of the power flow equations.
4. Solve for the correction vector Δ using $\Delta = J^{-1}[P_{\text{mismatch}} \quad Q_{\text{mismatch}}]^T$.
5. Update bus voltages & angles (V and θ) using

$$V_{\text{new}} = V_{\text{old}} + \Delta V \text{ and } \theta_{\text{new}} = \theta_{\text{old}} + \Delta \theta.$$
6. Repeat steps 2-5 until convergence criteria are met.

Once converged, calculate the power losses in the system:

$$P_{\text{loss}} = \sum_{i=1}^n \sum_{j=1}^n V_i V_j (G_{ij} \cos \theta_{ij} + B_{ij} \sin \theta_{ij}) \quad (6.49)$$

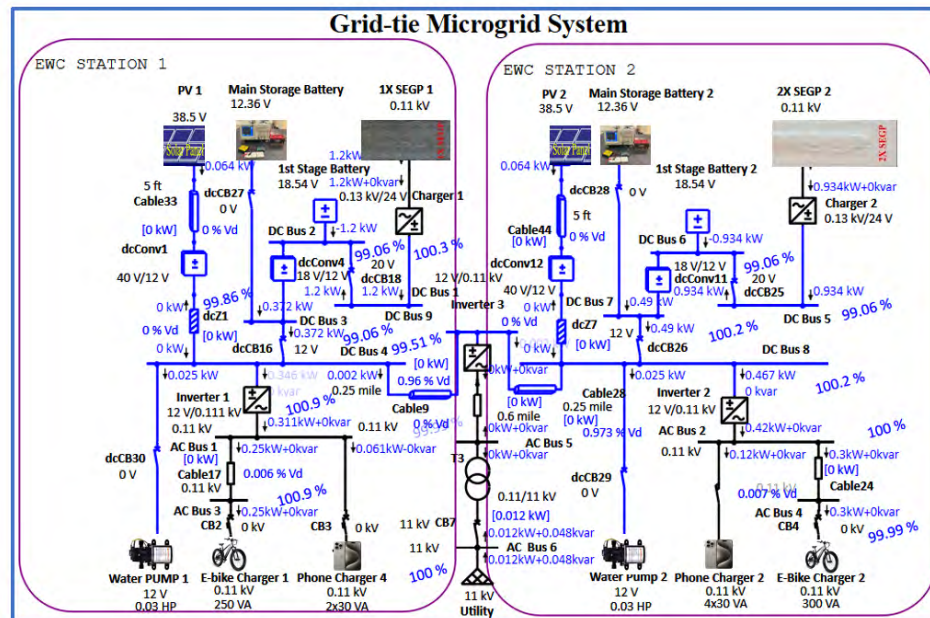


Fig. 6.7 Grid-Tie EWC Microgrid System.

6.7.1 Case Study 1: Unbalanced load flow analysis of Grid-tie EWC Microgrid System

Based on the proposed Grid-tie Hybrid EWC Microgrid system and equations 7.32 to 7.50, the unbalanced load flow analysis is conducted using ETAP software, as shown in

Figure 6.8. This analysis demonstrates that bus voltage stability ranges from 98% to 100%, thereby minimizing energy loss. Chargers are experiencing overvoltage and under-voltage conditions; a dual-stage smart energy charging system is utilized to maximize lower-generation SEGPS energy utilization. Table 6.13 highlights the operational status of critical components within the system. The critical report reveals that both instances of the 1st Stage Battery are showing negative power, indicating potential energy discharge. Additionally, both Charger 1 and Charger 2 are experiencing overload conditions in both AC and DC modes, with currents significantly exceeding their rated limits. Specifically, Charger 1 shows an overload with an AC current of 8.903 amps (160.9% of its rating) and a DC current of 71.875 amps (150% of its rating), while Charger 2 shows an overload with an AC current of 11.148 amps (167.3% of its rating) and a DC current of 93.750 amps (150% of its rating).

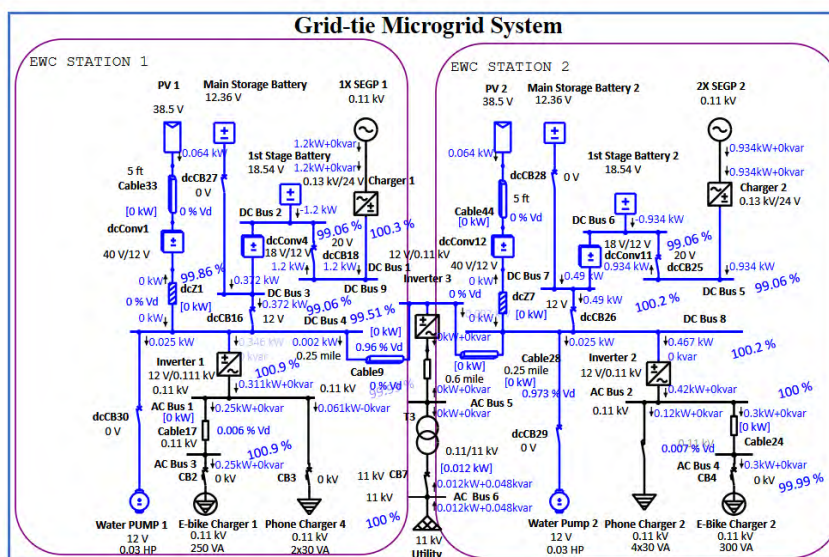


Fig. 6.8 Analysis of Unbalanced Load Flow of Grid-tie EWC Microgrid System.

These conditions suggest a risk of system instability or potential damage to the chargers. The marginal report indicates concerns regarding voltage levels, with 2X SEGPs

2 experiencing overvoltage conditions at 110.0 units consistently across all operating conditions. This highlights the need for improved voltage regulation mechanisms to protect connected devices and ensure system reliability. Addressing these critical and marginal issues is essential to prevent further damage, ensure system stability, and maintain operational safety.

TABLE 6.13

ANALYSIS OF UNBALANCED LOAD FLOW OF GRID-TIE EWC MICROGRID SYSTEM

<u>Critical Report</u>										
Device ID	Type	Condition	Rating/Limit	Unit	Operating A	Operating B	Operating C	%Op. A	%Op. B	%Op. C
1st Stage Battery	Battery	Negative Power	0.000	KW	-1.542	0.000	0.000	0.0	0.0	0.0
1st Stage Battery 2	Battery	Negative Power	0.000	KW	-2.124	0.000	0.000	0.0	0.0	0.0
Charger 1	Charger	Overload(AC)	5.533	Amp	8.903	8.903	8.903	160.9	160.9	160.9
Charger 1	Charger	Overload(DC)	47.917	Amp	71.875	0.000	0.000	150.0	0.0	0.0
Charger 2	Charger	Overload(AC)	6.662	Amp	11.148	11.148	11.148	167.3	167.3	167.3
Charger 2	Charger	Overload(DC)	62.500	Amp	93.750	0.000	0.000	150.0	0.0	0.0

<u>Marginal Report</u>										
Device ID	Type	Condition	Rating/Limit	Unit	Operating A	Operating B	Operating C	%Op. A	%Op. B	%Op. C
2X SEGP 2	Bus	Over Voltage						110.0	110.0	110.0

6.7.2 Case Study 2: Voltage Stability Analysis of Grid-tie EWC Microgrid System

Voltage stability analysis is conducted on the grid-tie microgrid system, as shown in Fig. 6.9. It is observed that voltage stability in this grid-tie EWC microgrid system is completely stable at 99-100%. The Hybrid EWC microgrid system has evolved into a Grid-tie microgrid system, extending 0.6 miles to connect with the utility from DC busbar 9, creating an IEEE 15 bus AC-DC Hybrid Microgrid System.

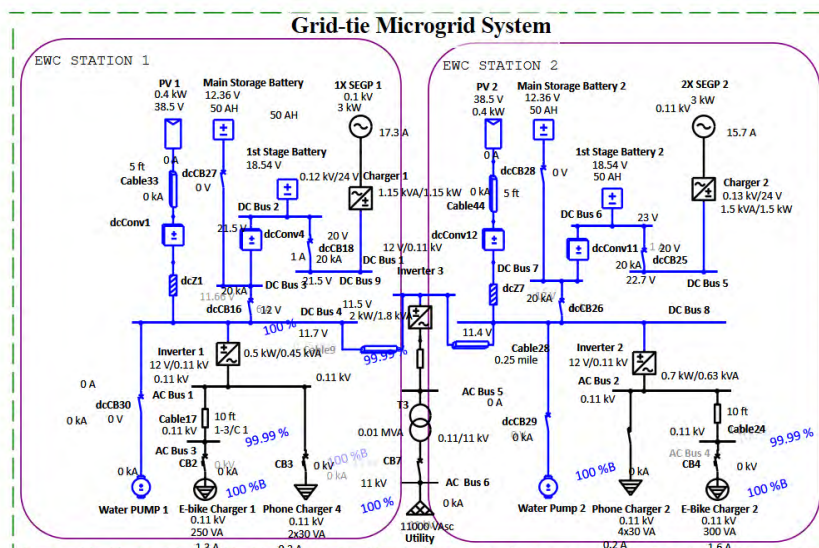


Fig. 6.9 Analysis of Voltage Stability of Grid-tie EWC Microgrid System.

This extension incorporates crucial components such as an inverter, cable, step-up transformer, switchgear, and utility connection. Inverter 3 plays a key role by converting 12 V DC energy to 110 V AC energy, establishing a link to AC Busbar 5 through a 0.6-mile cable (cable 9). AC Busbar 5 further connects to AC Busbar 6 via switchgear and a step-up transformer (T3, 0.11/11 kV, 10 KVA), eventually integrating with the substation for utility purposes. The system's performance metrics indicate that solar generation stands at 0.172226659 kWh, AC generation at 0.498051416 kWh, and battery discharging at 0.362575372 kWh, resulting in a system generation of 0.15269871 kWh. The demand is divided into AC demand of 0.098835917 kWh and DC demand of 0.00673077 kWh, summing up to a system demand of 0.105566687 kWh, with total energy loss at 0.047132023 kWh. The unbalanced load flow analysis in Case Study 1 reveals bus voltage stability ranging from 98-100 %, effectively minimizing energy loss. However, this analysis also brings attention to overvoltage and under-voltage issues in chargers,

necessitating the implementation of a dual-stage smart energy charging system to optimize their performance. Case Study 2 confirms the system's voltage stability within a range of 99-100 %, which ensures consistent and reliable operation.

6.8 Summary

This chapter examines the grid-tie microgrid-based hybrid EWC system, focusing on its technical and economic dimensions. The comprehensive techno-economic evaluation of Hybrid EWC systems for roadside facilities reveals a promising approach to tackling global challenges like freshwater scarcity, the energy crisis, and decarbonization. It assesses both microgrid and grid-tie microgrid systems under two scenarios: (PV and SEGP_{1X}) and (PV and SEGP_{2X}), highlighting their financial viability and sustainability despite the high initial investment compared to existing systems. The economic analysis explores various components' capacities, lifetimes, costs, and revenue streams, including e-bike charging fees, energy sales to utilities, and purified water sales. The EWC systems generate substantial revenue over the project duration, with significant contributions from e-bike charging, mobile charging, and drinking water sales, offering a comprehensive view of the project's financial performance.

CHAPTER 7

RESULTS AND DISCUSSIONS

The results and discussion chapter synthesizes the outcomes from extensive design simulations and prototype developments discussed in preceding chapters. By delving into sustainable energy generation technologies, this Chapter aims to unveil the insights gleaned from simulations and experimental assessments. It offers a comprehensive understanding of the technical performance of the developed prototypes and analyzed systems. Through critical discussions and in-depth analysis of results, this chapter strives to uncover actionable insights that can steer future research directions, inform policy decisions, and facilitate the practical implementation of sustainable energy-water-community integration solutions [94]-[107].

7.1 Analysis of PZT Cells Characteristics

The experimental analysis of the AEH is distributed across three subsections below, covering the outcomes of the 1X, 2X, and 3X layers of AEH based on the data obtained from the prototype models developed in the previously discussed section 5.1.

7.1.1 The experimental outcome of the 1X-Layer of AEH

The energy output of the single-layer thin film PZT cell in the Experimental AEH system (Fig. 7.1 and 7.2) is evaluated through the analysis of data from various samples. As detailed in Table 7.1, the average voltage is calculated, and the resulting generated energy is determined. The calculations for determining the data are shown below. This model observed that every single hit on the thin-film PZT by the lever took 7.5 milliseconds. Based on these observations, the following equations are used to determine

the accumulated energy from the 1X layer AEH over an hour. Thin film PZT cell produced a triangular signal, So calculating the average voltage from the triangle signal is

$$V_{avg1} = \frac{V_{peak1}}{2} \quad (7.1)$$

$$T_{cycle} = T_{active} \quad (7.2)$$

$$T_{cycle/s} = \frac{T_{cycle}}{1000} \quad (7.3)$$

$$V_{active} = V_{avg1} \times (T_{active} \times 1000) \quad (7.4)$$

$$V_{avg1/cycle} = \frac{V_{active}}{T_{cycle/s}} \quad (7.5)$$

$$P_{1L} = \frac{(V_{avg1/cycle})^2}{R} \quad (7.6)$$

$$E_{1L} = P_{1L} \times \text{time} \quad (7.7)$$

Where: V_{avg1} = Average voltage of the 1X Layer of AEH (V), V_{peak1} = Peak voltage of the 1X layer of AEH (V), T_{cycle} = Total active cycle in AEH (ms), T_{active} = Active time duration is 7.5 in AEH (ms), $T_{cycle/s}$ = Total active cycle in AEH (s), V_{active} = voltage contribution on the active time of the 1X layer of AEH (V), $V_{avg1/cycle}$ = Average voltage per cycle (V), P_{1L} = Power generated from the 1X layer of AEH (W), E_{1L} = Energy generated from the 1X layer of AEH (Wh).

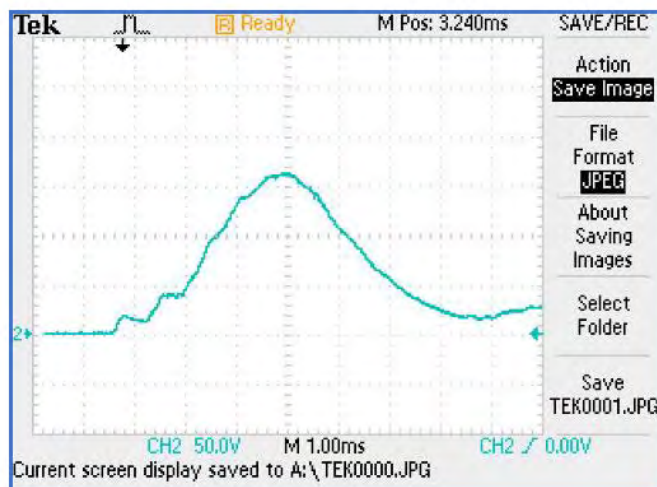


Fig. 7.1 The 1X-Layer of AEH Energy Analysis (random sample 1).

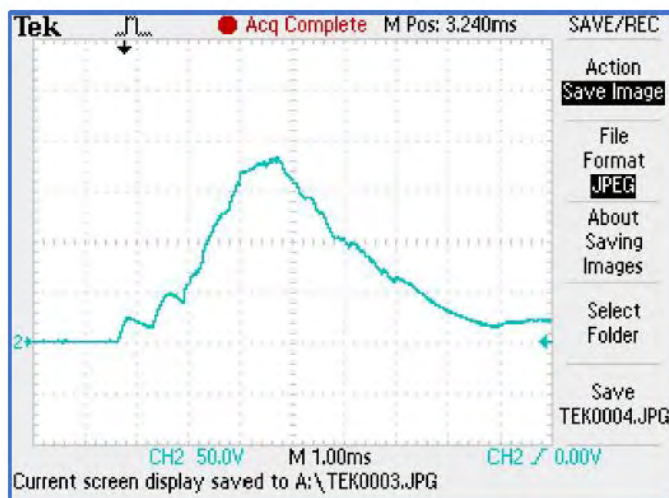


Fig. 7.2 The 1X-Layer of AEH Energy Analysis (random sample 2).

Based on the experimental data obtained from the oscilloscope and using this equation of the 1X Layer of AEH analysis from Table I reveals consistent trends across the samples, with the thin-film PZT diameter maintained at 25 mm and the thickness at 0.5 mm and a uniform 40 N force applied. The experiments maintained a 10 k Ω resistor, with a 0.33 μ F capacitor and a 7.5 ms time duration. Peak voltages ranged from 152 V to 175 V, while average peak voltages varied slightly from 161.50 V. Power outputs ranged from 0.56 W to 0.77 W. Overall, the average voltage and power for the 1X Layer of AEH were

approximately 80.55 V, respectively, indicating stable and reliable energy generation. Based on Table 7.2, the power output of a 1X layer of AEH is produced at 0.65 W, and energy is produced at 0.64 Wh in an hour.

TABLE 7.1

RESULT ANALYSIS OF 1X-LAYER OF AEH

<i>1X Layer</i>	<i>Thin-Film PZT (mm)</i>	<i>Force (N)</i>	<i>Resistor (kΩ)</i>	<i>Time Duration (ms)</i>	<i>Peak Voltage (V_{peak1})</i>	<i>Average Voltage (V_{avg1})</i>
Sample 1	25	40	10	7.5	160	80
Sample 2	25	40	10	7.5	170	85
Sample 3	25	40	10	7.5	175	87.5
Sample 4	25	40	10	7.5	155	77.5
Sample 5	25	40	10	7.5	167	83.5
Sample 6	25	40	10	7.5	152	75
Sample 7	25	40	10	7.5	154	77
Sample 8	25	40	10	7.5	157	78.5
Sample 9	25	40	10	7.5	153	76.5
Sample 10	25	40	10	7.5	168	84
Average	25	40	10	7.5	161.1	80.55

TABLE 7.2

ENERGY GENERATION FROM 1X-LAYER OF AEH.

<i>AEH</i>	<i>$V_{avg1/cycle}$ (V)</i>	<i>P_{1L} (W)</i>	<i>E_{1L} (Wh)</i>
<i>1X Layer</i>	80.55	0.64	0.64

7.1.2 The experimental outcome of the 2X-Layer of AEH

The energy produced by the 2X Layer thin film PZT cell within the Experimental AEH system (as shown in Fig. 7.3 and 7.4) is assessed by analyzing data from multiple

samples. The average voltage is computed according to Table 7.3, and subsequently, the energy generated is determined from this calculation. Based on these observations, the following equations are used to determine the accumulated energy from the 2X layer AEH over an hour. Thin film PZT cell produced a triangular signal, So calculating the average voltage from the triangle signal is

$$V_{avg2} = \frac{V_{peak2}}{2} \quad (7.8)$$

$$V_{avg2/cycle} = \frac{V_{active}}{T_{cycle/s}} \quad (7.9)$$

$$P_{2L} = \frac{(V_{avg2/cycle})^2}{R} \quad (7.10)$$

$$E_{2L} = P_{2L} \times \text{time} \quad (7.11)$$

Where: V_{avg2} = Average voltage of the 2X Layer of AEH (V), V_{peak2} = Peak voltage of the 2X layer of AEH (V), $V_{avg2/cycle}$ = Average voltage per cycle (V), P_{2L} = Power generated from the 2X layer of AEH (W), E_{2L} = Energy generated from the 2X layer of AEH (Wh).

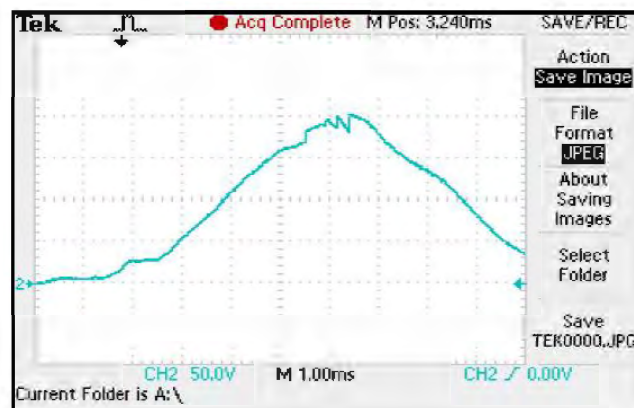


Fig. 7.3 The 2X-Layer of AEH Energy Analysis (random sample 1).

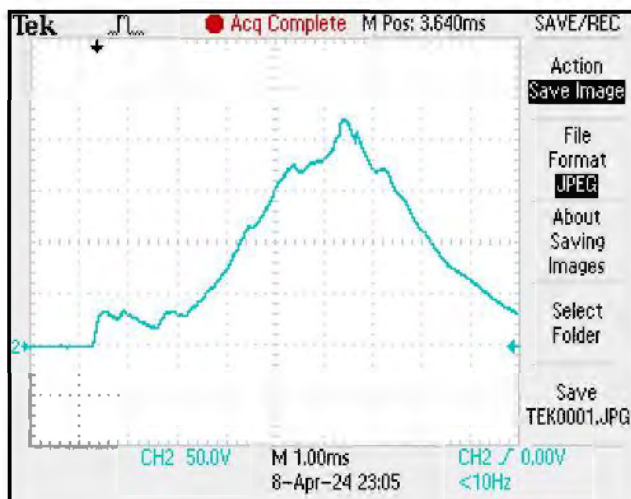


Fig. 7.4 The 2X-Layer of AEH Energy Analysis (random sample 2).

TABLE 7.3

RESULT ANALYSIS OF 2X-LAYER OF AEH.

<i>2X Layer</i>	<i>Thin-Film PZT (mm)</i>	<i>Force (N)</i>	<i>Resistor (kΩ)</i>	<i>Time Duration (ms)</i>	<i>Peak Voltage (V_{peak2})</i>	<i>Average Voltage (V_{avg2})</i>
Sample 1	25	40	5	7.5	200	100
Sample 2	25	40	5	7.5	210	105
Sample 3	25	40	5	7.5	220	110
Sample 4	25	40	5	7.5	225	112.5
Sample 5	25	40	5	7.5	220	110
Sample 6	25	40	5	7.5	204	102
Sample 7	25	40	5	7.5	205	102.5
Sample 8	25	40	5	7.5	215	107.5
Sample 9	25	40	5	7.5	200	100
Sample 10	25	40	5	7.5	210	105
Average	25	40	5	7.5	210.9	105.45

TABLE 7.4

ENERGY GENERATION FROM 2X-LAYER OF AEH.

AEH	$V_{avg2/cycle}$ (V)	P_{2L} (W)	E_{2L} (Wh)
2X Layer	105.45	2.22	2.22

Based on the data analysis provided in Table 7.3 for the 2X Layer of the AEH system, two of the 1X Layer of thin film PZT on top of one another, consistent trends can be observed across the samples. The thin-film PZT diameter was maintained at 25 mm and the thickness at 1 mm, with a constant force of 40 N applied. The experimental setup included a 5 k Ω resistor, a 0.33 μ F capacitor, and a 7.5 ms time duration. Across the samples, the peak voltages ranged from 200 V to 225 V, with an average peak voltage of approximately 210.9 V. Based on Table 7.4, the power output of a 2X layer of AEH is produced at 2.22 W, and energy is produced at 2.22 Wh in an hour.

7.1.3 The experimental outcome of the 3X-Layer of AEH

The energy output from the 3X Layer of thin-film PZT cells in the Experimental AEH system, which comprises three 1X layers of thin-film PZT cells set up consecutively, as shown in Fig. 7.5 and 7.6, is evaluated through the analysis of data collected from various samples.

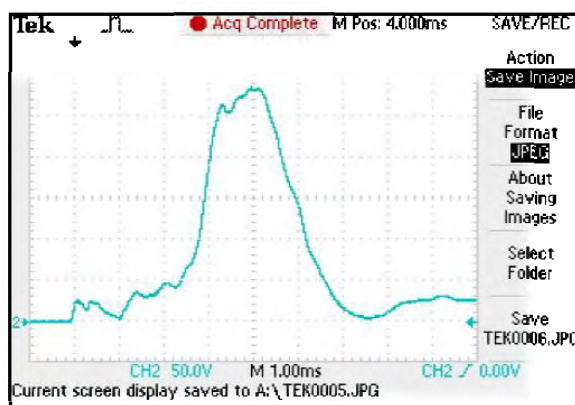


Fig. 7.5 The 3X-Layer of AEH Energy Analysis (random sample 1).

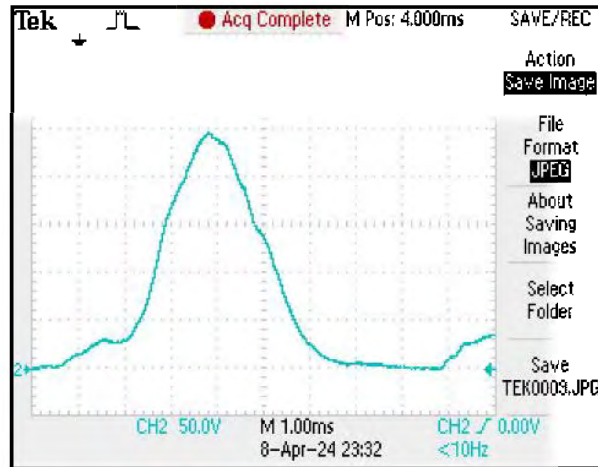


Fig. 7.6 The 3X-Layer of AEH Energy Analysis (random sample 2).

The average voltage is calculated using the data presented in Table 7.5, and subsequently, the generated energy is determined based on this calculation. The calculations for determining the data are shown below. The thin-film PZT cell produced a triangle signal, So calculating the Average voltage from the triangular signal is

$$V_{avg3} = \frac{V_{peak3}}{2} \quad (7.12)$$

$$V_{avg3/cycle} = \frac{V_{active}}{T_{cycle/s}} \quad (7.13)$$

$$P_{3L} = \frac{(V_{avg3/cycle})^2}{R} \quad (7.14)$$

$$E_{3L} = P_{3L} \times \text{time} \quad (7.15)$$

Where: V_{avg3} = Average voltage of the 3X Layer of AEH (V), V_{peak3} = Peak voltage of the 3X layer of AEH (V), $V_{avg3/cycle}$ = Average voltage per cycle (V), P_{3L} = Power generated from the 3X layer of AEH (W), E_{3L} = Energy generated from the 3X layer of AEH (Wh).

Based on the data analysis provided in Table 7.5 for the 3X Layer of the AEH system, where three 1X layers of thin-film PZT are stacked on top of one another, consistent trends are evident across the samples. The thin-film PZT maintains a diameter of 25 mm and a thickness of 1.5 mm, with a constant force of 40 N applied. The experimental setup includes a 3.3 k Ω resistor, a 0.33 μ F capacitor, and a 7.5 ms time duration. Across the samples, peak voltages range from 235 V to 250 V, with an average peak voltage of approximately 242.3 V. The average voltage output for the 3X Layer is around 121.15 V. Based on Table 7.6, the power output of a 3X layer of AEH is produced at 2.22 W, and energy is produced at 2.22 Wh in an hour.

TABLE 7.5

RESULT ANALYSIS OF 3X-LAYER OF AEH.

<i>3X Layer</i>	<i>Thin-Film PZT (mm)</i>	<i>Force (N)</i>	<i>Resistor (kΩ)</i>	<i>Time Duration (ms)</i>	<i>Peak Voltage (V_{peak3})</i>	<i>Average Voltage (V_{avg3})</i>
Sample 1	25	40	3.3	7.5	235	117.5
Sample 2	25	40	3.3	7.5	240	120
Sample 3	25	40	3.3	7.5	245	122.5
Sample 4	25	40	3.3	7.5	250	125
Sample 5	25	40	3.3	7.5	237	118.5
Sample 6	25	40	3.3	7.5	242	121
Sample 7	25	40	3.3	7.5	248	124
Sample 8	25	40	3.3	7.5	238	119
Sample 9	25	40	3.3	7.5	243	121.5
Sample 10	25	40	3.3	7.5	245	122.5
Average	25	40	3.3	7.5	242.3	121.15

TABLE 7.6

ENERGY GENERATION FROM 3X-LAYER OF AEH.

<i>AEH</i>	$V_{avg3/cycle} (V)$	$P_{3L} (W)$	$E_{3L} (Wh)$
<i>3X Layer</i>	121.15	4.45	4.45

In summary, Tables 7.2, 7.4, and 7.6 reveal a significant increase in energy generation. For the 1X layer of AEH, the average voltage per cycle is 80.55 V, generating a power of 0.64 W and an energy output of 0.64 Wh. When the layer configuration is increased to 2X, the average voltage per cycle rises to 105.45 V, with a significant increase in power output to 2.22 W and an energy generation of 2.22 Wh. The 3X layer configuration further boosts these tables, with an average voltage per cycle of 121.15 V, producing 4.45 W of power and 4.45 Wh of energy. Comparing the percentage increases in energy generation from the 1X to 2X layer, the energy increases by approximately 246.88 %. From the 2X to 3X layer, the energy increases by approximately 100.45 %. From the 1X to 3X layer, the energy increases by approximately 595.31 %, as shown in Fig 7.7.

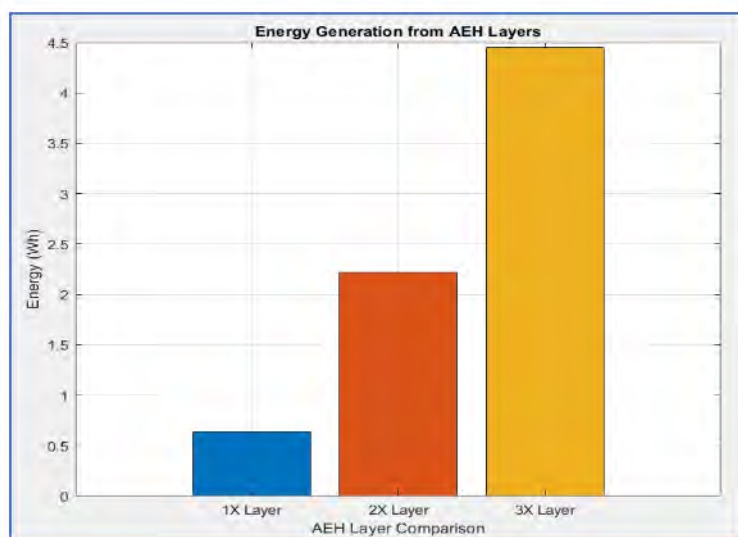


Fig. 7.7 Comparison of AEH Layers.

7.1.4 Comparing PZT Energy Vs. PV Energy

In this section, AEH system data have been compared with solar panel data available in the market to determine the possibility and effectiveness of thin-film PZT as a future alternative energy generation source. DATA obtained from the manufacturer's 100 W PV panel specifications indicate that PV_{max} is calculated as $20.4 \text{ V} \times 4.91 \text{ A} = 100 \text{ W}$ under maximum light conditions. However, in practical use with an MPPT system, the actual maximum power obtained is $\text{Real } PV_{max} = 0.825 \times P_{max} = 82.5 \text{ Wh}$ at maximum light, as shown in Fig. 7.7 of the plot.

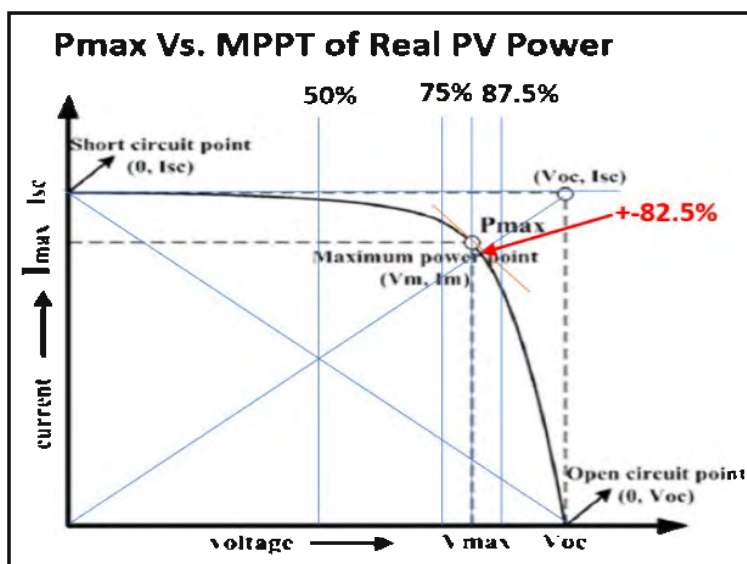


Fig. 7.7 Analysis of Solar Panel.

Based on this, the following results are derived for the 100 W_p PV panel:

$$\text{Total Area} = 17.22 \text{ square feet} \quad (7.16)$$

$$E_{Wh/foot} = \frac{PV_{capacity}}{PV_{max}} = 4.79 \text{ (Wh)} \quad (7.17)$$

Where: $E_{Wh/foot}$ = Energy generation from per square inch PV panel (Wh), $PV_{capacity}$ = PV panel capacity (W_p), PV_{max} = MPPT energy generation (Wh).

The data in Table 7.7 compares the energy generation capabilities of a silicon-based PV panel and various configurations of thin-film PZT energy harvesters (AEH) based on layers. The PV panel, with an energy generation of 4.79 Wh per square foot and an operational time of 4-8 hours per day, produces a maximum daily energy output ranging from 19.16 Wh to 38.32 Wh. In contrast, the 1X-layer AEH produces 0.64 Wh per square foot and can operate continuously for 24 hours, resulting in a maximum daily energy output of 15.36 Wh. Increasing the layers enhances the AEH's performance: the 2X-layer configuration generates 2.22 Wh per square foot, yielding 53.28 Wh per day, while the 3X-layer configuration produces 4.45 Wh per square foot, resulting in 106.8 Wh per day. An assumed 4X-layer configuration would generate 8.90 Wh per square foot, achieving a substantial 213.6 Wh per day. This comparison illustrates that while PV panels have higher energy density per hour, the continuous operation of AEH layers, especially in multi-layer configurations, can surpass the daily energy output of PV panels,

TABLE 7.7

COMPARISON OF THIN-FILM PZT ENERGY VS. PV PANEL ENERGY

Sources	Energy Wh/ Square-foot	Maximum Operation/day (hour)	Maximum Energy (Wh/day)	Reasonable Operation/day (hour)	Projected Energy (Wh/day)
PV Panel	4.79	4-8	19.16 - 38.32	4-8	19.16 - 38.32
PZT1L	0.64	24	15.36	2-4	1.28-2.56
PZT2L	2.22	24	53.28	2-4	4.44-8.88
PZT3L	4.45	24	106.8	2-4	8.90-17.8

7.2 Analysis of Sustainable Energy Generating Pad (SEGP) System

Based on the 12 developed energy-generating pads, three of those pads are analyzed in the sections below.

7.2.1 Analysis of Energy Generating Pad (EGP)

A seven-layered, 3-foot EGP power system was developed successfully, as shown in Fig. 7.12. A bike rider repeatedly ran on the EGP to determine the pad's quality and reliability. A 7.5 k Ω load was used for the test. The average voltage of the three-foot EGP produced 68 VDC by the pressure from a rider of 142 lbs (including the bike weight), and the pad's power was 661.53 mW/s from each PZT strip. The results of these tests are shown in Table 7.8. It was found that when the bike was running at the speed of 2 mph (2.93 fps), the output voltage of the pad was 28 VDC. In contrast, when the speed was 5 mph (7.33 fps), the voltage was 68 VDC. When the speed was 7 mph (10.27 fps), the voltage increased to approximately 85 VDC, as shown in Fig. 7.8. The test data are shown in Table 7.9. The relationship between the speed and the output voltage was obtained based on this. The EGP would be placed outdoors on the actual bike lane. Based on the general solution, the average speed of 15 mph (22 fps) would produce 130 VDC. As a result, more power can be generated at higher bike speeds. So, significant improvement in energy generation is achievable by an improved EGP, which will be the next step in this project. Currently, all materials in the EGP layers are not 100% hydrophobic.

TABLE 7.8

THE EXPERIMENTAL OUTCOME ON THE BIKE LANE EGP

Items	Specifications & Results
EGP Length	3 Feet
Output Voltage	68 VDC average at 5 mph
EGP Layers	7
Tested load	7.5 k Ω
Total weight of the bike with rider	142 pounds
Speed of the running bike	2-7 mph
Power of each DCPR strip	66.53 mW/s

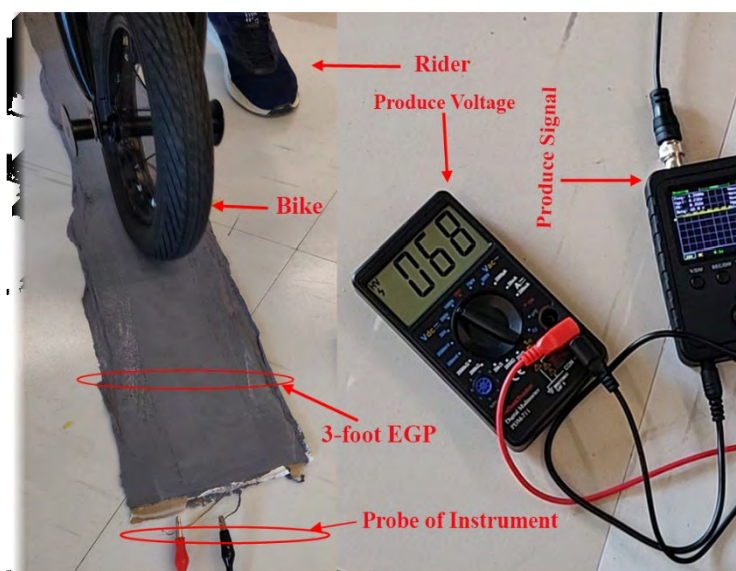


Fig. 7.8 A Three-Foot EGP is tested in the Lab.

The general solution of impact produced by speed and the output voltage from the EGP by running the bike in the lab was found as follows:

$$EGP_V = 0.0162X_{fps}^3 - 0.7765X_{fps}^2 + 15.656X_{fps} - 11.452 \quad (7.18)$$

where: EGP_V = the EGP rail voltage (VDC)

X_{fps} = The speed of the bike (fps).

Various tests were done to identify the performance of the prototype SEGP and compare the differences between the simulation and the prototype model. The experimental results of the prototype SEGP are described in Table 7.9. The weight of the test bike rider was about 148 lbs, but the SEGP can sustain up to 400 lbs. The biker's speed on the SEGP is between 3 to 10 mph. The SEGP was tested repeatedly. The voltage found from these tests was between 68 to 90 VDC. The average produced voltage of the SEGP is shown in Fig. 7.9 from a run of a bike.

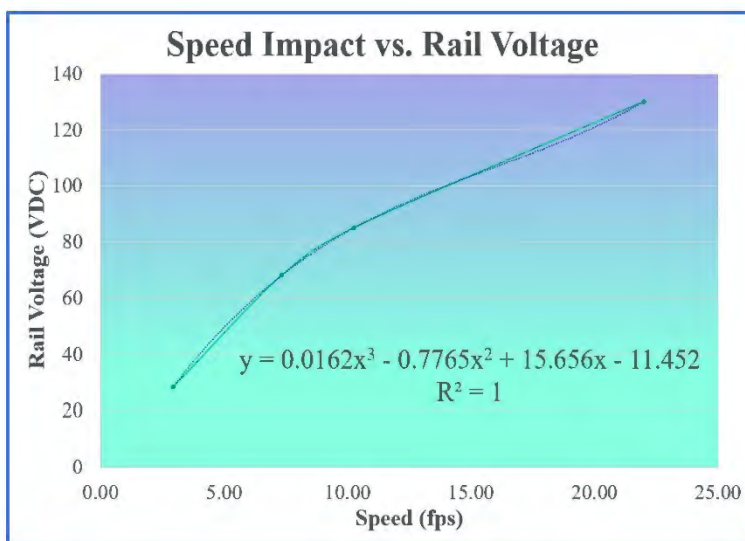


Fig. 7.9 The Relationship Between Speed and the Voltage Generation.

TABLE 7.9

TESTING RESULTS ON THE RUNNING BIKE UNDER THE EGP.

Speed		Rail Voltage
Fps	Mph	
2.93	2	28.2
7.33	5	68
10.27	7	85

TABLE 7.10

RESULT ANALYSIS OF THE SEGP

<i>Items</i>	<i>Quantity</i>	<i>Unit</i>
SEGP length	60	Inch
SEGP Layers	7	Pcs
The total weight (bike & rider)	148	Lbs
Running bike speed	3 – 10	Mph
Produced Voltage	68 – 90	VDC
Produced Current	0.17 - 0.26	mA
Produced Power	0.35 – 0.72	Watt/sec/ride

The produced current was found to be between 0.17 to 0.27 mA. Several sets of tests were conducted on the SEGP. Test results are available in Table 7.11. When the speed is low at around 3 mph, the power generation is low at around 0.35 Watts/sec/ ride. When speed is around 8 mph, the SEGP power is around 0.61 Watts/sec/ride. At the highest tested speed of 10 mph, the generation is the highest at around 0.72 Watts/sec/ride. The speed versus power generation curve is shown in Fig. 7.10.

TABLE 7.11

TESTED RESULTS ON THE RUNNING SEGP

<i>Speed (mph)</i>	<i>Voltage (VDC)</i>	<i>Current (mA)</i>	<i>Power (Watt/sec/ride)</i>
3.00	68	0.17	0.35
5.00	73	0.20	0.44
6.00	76	0.21	0.49
7.00	80	0.22	0.55
8.00	85	0.23	0.61
10.00	90	0.26	0.72

The general solution of impact produced by speed and the output power from the EGP by running the bike in the lab was found to be:

$$EGP_P = 0.0044X_{mph}^3 - 0.0441X_{mph}^2 + 0.1973X_{mph} + 0.1833 \quad (7.19)$$

where: EGP_p = The produced Power (Watt)

X_{mph} = The speed of the bike (mph).

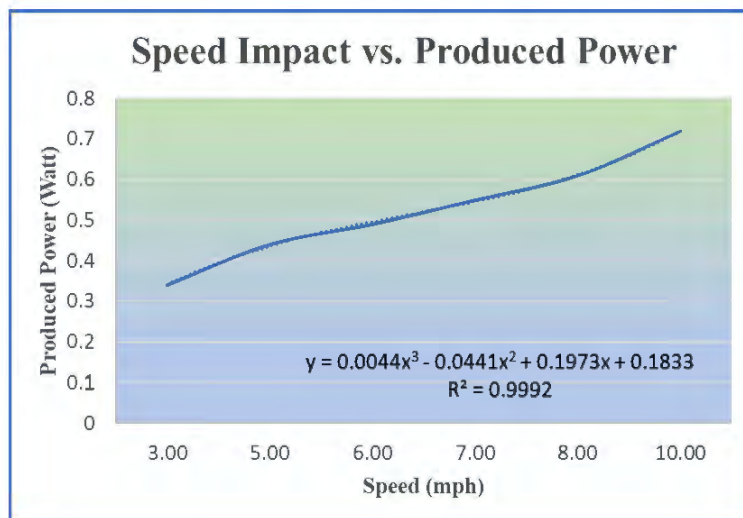


Fig. 7.10 The correlation between speed vs. power generation from the SEGP.

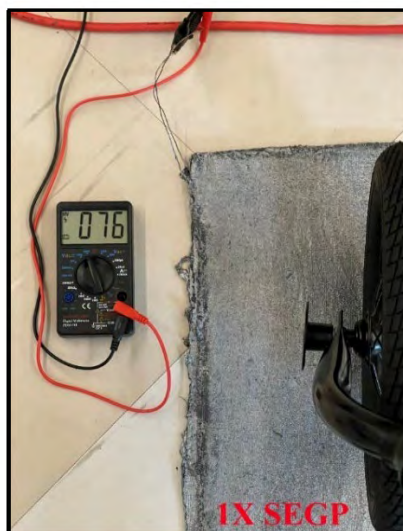
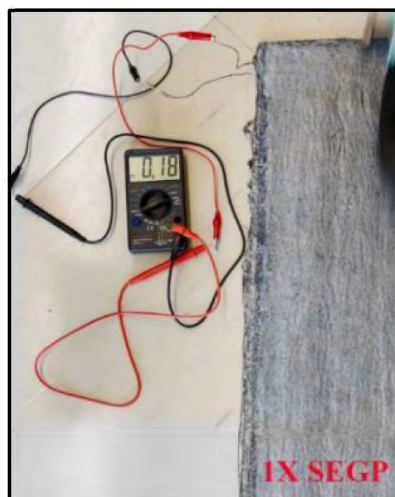
7.2.2 Analysis of Sustainable Energy Generating Pad₁ (SEGP_{1X})

In this section, the experimental findings can be briefly summarized as follows, as well as mentioned in Table 7.12. The SEGP_{1X} prototype was consistently tested and performed using the bike within the 10-12 mph speed range, underscoring its suitability for lightweight vehicle applications (bike). The prototype demonstrated robust operation within a weight range of 150-160 lbs. Voltage measurements within the 68-76 V range, as shown in Fig. 7.11. This highlights the prototype's adequate capacity to generate electrical potential. The system has a reliable current of about 0.16-0.18 mA of the PZT cells employed in the prototype, as shown in Fig. 7.12.

TABLE 7.12

PROTOTYPE TESTING ANALYSIS OF SEGP_{1X}.

Type	Speed (mph)	Weight (lbs)	Voltage (V)	Current (mA)	Power (W/ride)
PZT Cell	10-12	150-160	68-76	0.16-0.18	0.011-0.014
SEGP- 5 feet	10-12	150-160	68-76	4.8-5.4	0.33-0.41

Fig. 7.11 Voltage Testing on the Prototype of SEGP_{1X}.Fig. 7.12 Current Testing on the Prototype of SEGP_{1X}.

The prototype exhibited a power output ranging from 0.011 W to 0.014 W during the operation where 70 % of the thin film PZT Cell is active, confirming its practical capability to convert mechanical energy to electrical energy. The 5-foot SEGP prototype displayed a power output ranging from 0.33 W/ride to 0.41 W/ride during operation, described in Table 7.12.

7.2.3 Analysis of Sustainable Energy Generating Pad₂ (SEGP_{2X})

The experimental analysis encompasses the evaluation of the 5-foot SEGP_{2X} prototype: The SEGP_{2X} prototype consistently demonstrated performance within the 10-12 mph speed range, validating its suitability for bike applications. Table 7.13 illustrates how the prototype maintained reliability and stability by operating effectively within a weight range of 150-160 lbs, including the bike and rider.



Fig. 7.13 Current Testing on the Prototype of SEGP_{2X}.



Fig. 7.14 Voltage Testing on the Prototype of SEGP_{2X}.

TABLE 7.13

PROTOTYPE ANALYSIS OF SEGP_{2X}.

<i>Type</i>	<i>Speed (mph)</i>	<i>Weight (lbs)</i>	<i>Voltage (V)</i>	<i>Current (mA)</i>	<i>Power (W/ride)</i>
PZT Cell	10-12	150-160	82-85	0.22-0.26	0.018-0.022
SEGP- 5 feet	10-12	150-160	82-85	6.60-7.80	0.54-0.67

Voltage measurements consistently fell within the 82-85 V range, confirming the prototype's efficiency in generating electrical potential, as shown in Fig. 7.13. Steady current readings of 0.22-0.26 mA underscored the PZT cells' current output reliability within the prototype, As described in Table. 7.13. Averaging these values yielded an energy of 20.04 mW from each PZT collected per ride. During operation, the 5-foot SEGP_{2X} prototype exhibited a substantial power output ranging from 0.54 W/ride to 0.67 W/ride, confirming its practical capacity to transform mechanical energy for real-world applications.

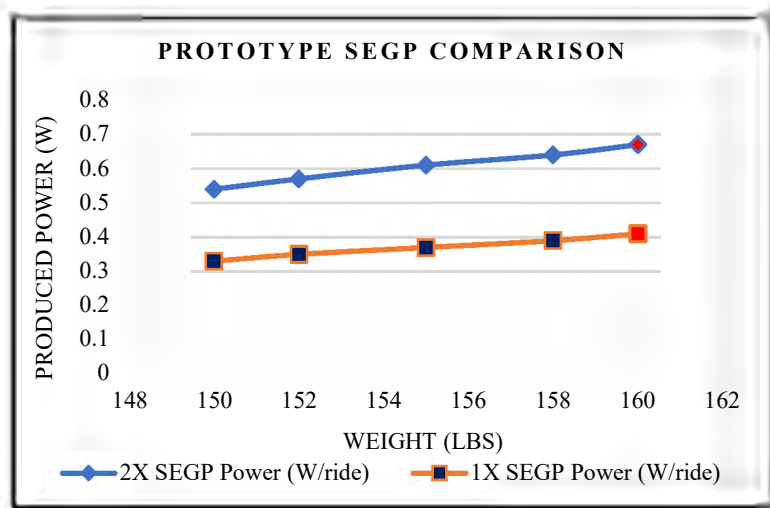


Fig. 7.15 Prototype Result Comparison for Both the SEGP.

The multiple linear regression equation for the given data from Tables 7.12 & 7.13 is:

$$P_{1XSEHP} = 0.0076w - 0.8153 \tag{7.20}$$

$$P_{2XSEHP} = 0.0126w - 1.3543 \tag{7.21}$$

Where: Weight (lbs) is the independent variable (w). Prototype 1X-SEGP Power (W/ride) is the dependent variable (P_{1XSEHP}). Prototype 2X-SEGP Power (W/ride) is the dependent variable (P_{2XSEHP}). This model explains a high proportion of the variability in weight based on 1X and 2X-SEGP Power.

TABLE 7.14

EXPECTED GENERATION ANALYSIS FROM SEGP_S

Speed Level	Running Bike/day	Riding time (hr)	Distance Cover (mile)	TP _{1XSEGP} (kWh/day)	TP _{2XSEGP} (kWh/day)
	1	0.5	5	0.00102	0.00210
		1	10	0.00210	0.00422
	2	0.5	5	0.00210	0.00422
		1	10	0.00422	0.00844

Beginner	10	0.5	5	0.0102	0.0210	
		1	10	0.0210	0.0422	
	100	0.5	5	0.12	0.21	
		1	10	0.21	0.42	
Intermediate	1	0.5	7.5	0.00158	0.00316	
		1	15	0.00316	0.00636	
	2	0.5	7.5	0.00316	0.00317	
		1	15	0.00636	0.00127	
	10	0.5	7.5	0.0158	0.0316	
		1	7.5	0.0316	0.0636	
	100	0.5	7.5	0.158	0.316	
		1	15	0.316	0.636	
	Advanced	1	0.5	10	0.00212	0.00422
			1	20	0.00422	0.00844
2		0.5	10	0.00422	0.01688	
		1	20	0.00422	0.00844	
10		0.5	10	0.0212	0.0422	
		1	20	0.0424	0.0844	
100		0.5	10	0.212	0.422	
		1	20	0.424	0.844	

The 1X and 2X-SEGP prototypes proved effective at 10-12 mph speeds, suitable for lightweight vehicle applications, including a bike with a rider weighing 150-160 lbs. The 2X-SEGP prototype exhibited a substantial power output advantage over the 1X SEGP (0.54 W/ride to 0.67 W/ride vs. 0.33 W/ride to 0.41 W/ride), as shown in Fig.7.15. Compared to the 5-foot SEGP, it generated even higher power output (0.54 W/ride to 0.67 W/ride). The 2X-SEGP showcased a remarkable 145%-160% power output increase over the 1X SEGP, considering the bike with the rider's Weight. At the Beginner level with 160 lbs weight, power generation varies with running time (min/day) and distance (miles), with TP_{1XSEGP} producing between 0.00102 kWh and 0.21 kWh per day and TP_{2XSEGP} ranging from 0.0021 kWh to 0.42 kWh per day. Intermediate-level with the same weight results follow a similar pattern but with longer riding times, with TP_{1XSEGP} generating between

0.00158 kWh and 0.316 kWh and TP_{2XSEHP} producing between 0.00316 kWh and 0.636 kWh per day. Advanced-level people with the same weight performance see even higher power generation, ranging from 0.00212 kWh to 0.424 kWh for TP_{1XSEGP} and from 0.00422 kWh to 0.844 kWh for TP_{2XSEGP}. The power generation is positively correlated with riding time and Distance, with the most significant power output observed at the highest speed and longest duration. The specific power output values for Total Generated Power of SEGP_{1X} (TP_{1XSEGP}) and Total Generated Power of SEGP_{2X} (TP_{2XSEGP}) at different scenarios are provided for each speed level, offering valuable insights into the energy production capabilities of these SEGP systems. Based on the real-time implementation, simulation, and prototype results, a comprehensive analysis of energy generation from SEGPs has been provided, as illustrated in Table 7.14. and Fig. 7.16 and 7.17 showed how much energy was produced from SEGP while the number of bikes with different levels of bike speed on the run for 30 minutes and an hour. The Table outlines the expected power generation from SEGPs at different speed levels: Beginner, Intermediate, and Advanced; considering various parameters, such as running time and distance covered, it is observed that at different speed levels, bikers cover more distance at the same time and produce more power output than beginner level than intermediate level that advanced level in kilowatt-hours per day for both TP_{1XSEGP} and TP_{2XSEGP} systems.

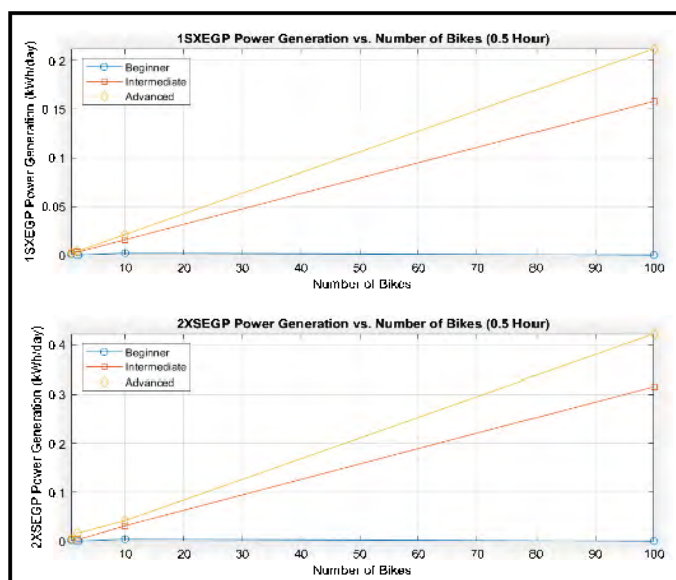


Fig. 7.16 Expected power generation Vs. No. Bike for 30 min riding.

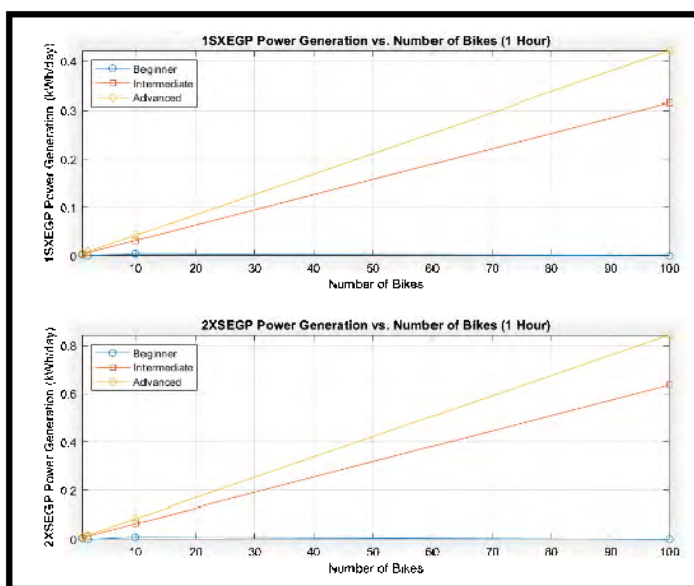


Fig. 7.17 Expected power generation Vs. No. Bike for 60 min riding.

7.3 Analysis of Dual-Stage Charge Storage and Collection System

In the lab experiment, A new type of alternative energy is used as a power source, producing a UPAP signal. After implementing the unique rectification technique, the source delivered the output voltage in the range between 60 VDC and 130 DVC, as

previously discussed in sections 4.2 and 5.5. The rectification efficiency is around 94%. The rectification electricity goes to the CCSU#1 system. The CCSU#1 collects maximum energy and immediately stores energy in the lithium-ion battery by the Storage V_{boost} . In this experiment, the delivery voltage of the CCSU#1 is 18 DVC, as shown in Fig. 7.18. However, It is not a fixed voltage, and it can change more or less depending on the supplied energy sources and the capacity of their storage system. When the Storage V_{boost} is fully charged, CCSU#2 starts operating to dump the charge from CCSU#1 by the Storage I_{boost} . In this operation, the CCSU#1 charges are delivered discretely to the large-capacity lithium-ion battery of CCSU#2 until fully charged.

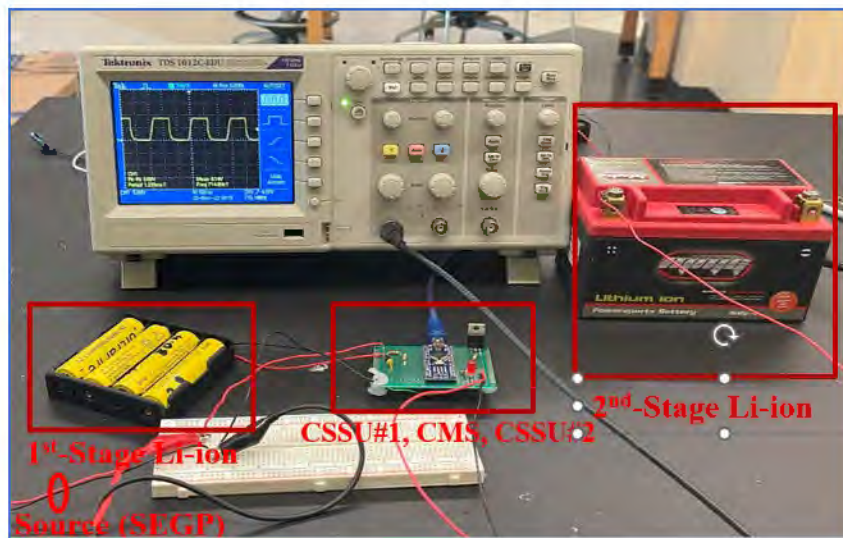


Fig. 7.18 Operational DSCS System.

The output voltage of the CCSU#2 system is 12.6 VDC. In this prototype, the reference voltage for the CMS operation is set high at 12.6 VDC and low at 6 VDC. However, all these voltage settings are changeable and can be reprogrammed in the microcontroller. If the discharging voltage falls below 6 VDC, then the CCSU#2 system turns on sleep mode to protect the storage. Fig. 7.19 shows the current and voltage

operations in the prototype DCS module. Furthermore, the auxiliary load performed by the dual-stage CCSU is conformed by CCSU#1 and CCSU#2 as they are linked to each other. When CMS finds both lithium energy storages are within acceptable operating limits and fully charged, the auxiliary load can only be turned on. Thus, energy also continues to flow from the source while the CMS turns on the auxiliary load. The auxiliary load can serve power to a dummy load, micro-grid, vehicle charging station, various appliances, etc.

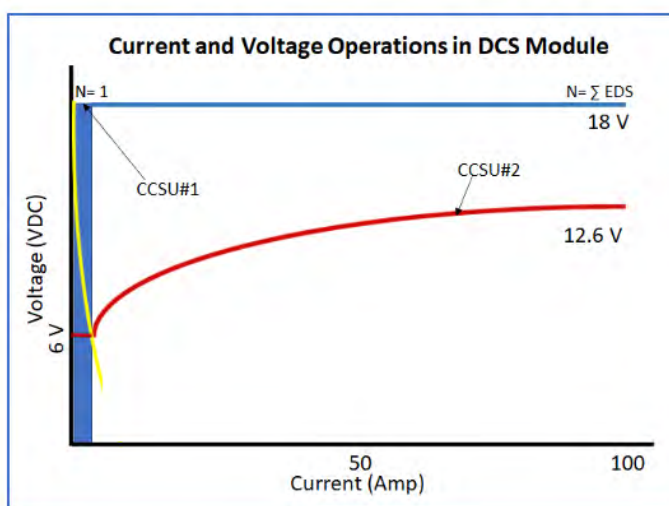


Fig. 7.19 Current and Voltage Operations in the DSCS Module.

7.3.1 Analysis of the SEGP Connected to the Lithium Batteries

The developed prototypes of SEGPs are tested in the lab. The SEGP had 18 PZT cells. During the experiment, it was found that 12 PZT Cells were active and produced electricity. This could be due to improper soldering of the voltage DC rail output. When a bike rider ran the bike repeatedly on the SEGP, it produced a voltage between 65-85 V, shown in Fig. 7.20. The produced current was between 0.15 – 0.22 mA, as shown in Fig. 7.21. The energy produced by the SEGP was, on average, 0.66 Wh/ride. Now, the Battery was fully charged by the SEGP with 50 runs of the bike (2 wheels), starting at 2.84 V, as

shown in Fig. 7.22. The battery stored energy from the SEGP and settled at 3.49 V, and the maximum reached 4.2 V after charging, as shown in Fig. 7.23.

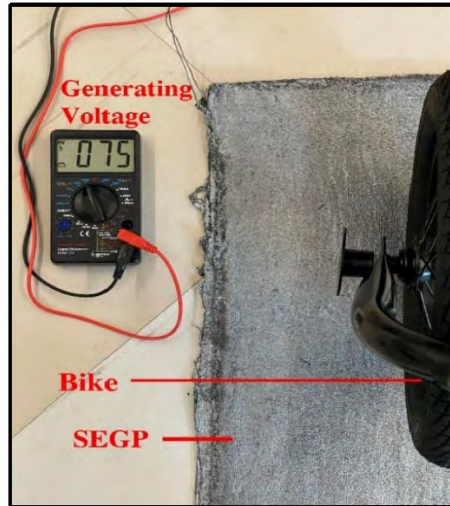


Fig. 7.20 Average generating Voltage from the SEGP.

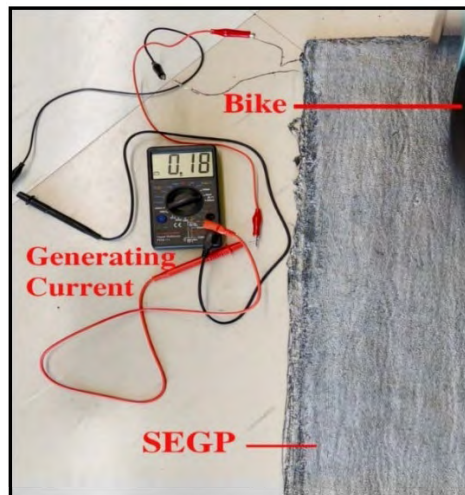


Fig. 7.21 Average generating current from the SEGP.

7.3.2 Analysis of DSCS Connected to the SEGP in Case Study 1

Case study 1 is the continuous work from section 5.5. If the produced energy is stored in Microchip technology's experimental lithium batteries' average voltage condition methods, then,

$$V_{com} = 3.223 \text{ V} \quad (7.22)$$

$$\frac{E}{50} = \frac{9.38}{50} = 187.6 \text{ mWhr/run} \quad (7.23)$$

$$= 93.8 \text{ mWhr/wheel} \quad (7.24)$$

The battery is fully charged after 50 rides. 12 active PZT cells in 5 ft of SEGP pad give:

$$E \text{ of cell per wheel} = 93.8/12 \text{ mWh} = 7.817 \text{ mWhr/cell/wheel.} \quad (7.25)$$

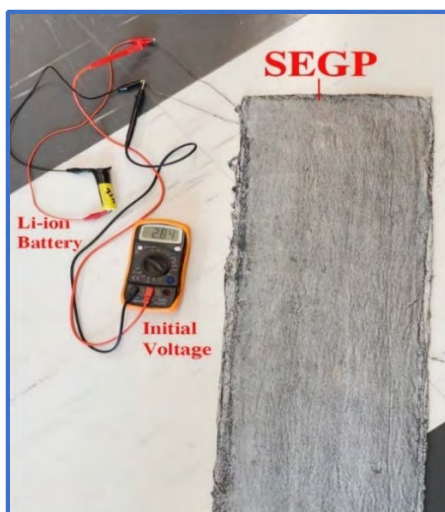


Fig. 7.22 Initial Voltage of 18650 Lithium-ion battery.



Fig. 7.23 Fully Charge of 18650 Lithium-ion battery.

7.3.3 Analysis of DSCS Connected to the SEGP in Case Study 2

This Case Study 2 is the continuation of previous work in sections 4.2 and 5.5. SEGP energy = 660 mWh/cell was tested on average. The energy was generated for 12 ms-20 ms duration of mechanical impacts of running the bike on the SEGP. So, the average estimated frequency was 60 Hz.

So, Energy from SEGP, $E = 660/60 = 11$ mWh/cell.

For produced energy stored in 18650 Samsung or Toshiba brand lithium batteries using the maximum voltage condition method, the datasheet provided this information below when compared to case study 2.

The ratio of Voltage:

$$V_{\text{ratio}} = \frac{V_{\text{max}}(\text{from Samsung or Toshiba})}{V_{\text{max}}(\text{from SEGP})} \quad (7.26)$$

$$V_{\text{ratio}} = (4.6)^2 / (4.2)^2 = 1.2$$

or 20% higher of the Samsung and Toshiba than SEGP experiments.

Similarly current, I_{ratio} increases by 1.2 or 20% because of

$$I = \frac{V}{R_{\text{batt}}} \quad (7.27)$$

Where: R_{batt} is the internal resistance.

Thus, the power or energy is increased by

$$E = V_{\text{ratio}} * I_{\text{ratio}} = 1.2 * 1.2 = 1.44 \text{ or } 44\%$$

Recalculating the results of case study 1:

$$\text{Energy of SEGP, max E-eq} = 7.817 * 1.44 \text{ mWh} = 11.256 \text{ mWh} \quad (7.28)$$

11.256 mWh is the maximum energy for the Toshiba/Samsung battery if it was charged at a max voltage = 4.6 V. So, the energy at max charging mode is 11.256 mWh, comparable to the PZT charging, which is 11 mWh/cell/wheel the 18650 at the SMART lab at PVAMU.

Thus, Performance ratio = $11.0/11.256 = 0.977$

$$= 97.7\%.$$

7.4 Projections of Energy from SEGPs for Various Locations

Based on the outcome of the prototypes developed in the lab, a comparative analysis of SEGP energy generation is conducted for different locations in Houston to determine how much energy will be generated from SEGPs. Based on estimates, approximately 5,000 bike rides occur daily in Houston, with around 1,000 of these rides being on e-bikes and the remaining 4,000 on manual bikes [110]-[111] on these Popular trails include the Heights Hike & Bike Trail, Memorial Park, and George Bush Park. On average, each trail runs 1667 bikes and e-bikes per day, and around 1800+ bikes runs in the TAMU, College Station Campus [113].

The MKT/SP Rails to Trails, also known as the Heights Hike and Bike Trail, is a scenic 4.6-mile urban trail in Houston, Texas, stretching from W 26th Street to W 7th Street and N Shepherd Drive to Hogan Street, as shown in Fig 7.24. Located in the historic Heights neighborhood, this trail offers a picturesque route featuring views of the Houston skyline and charming, oak-lined residential streets. It serves as a popular spot for walking, jogging, and cycling, providing a tranquil escape amidst the bustling city environment.



Fig. 7.24 The MKT/SP Rails to Trails.



Fig. 7.25 The Memorial Park Biking Trails.

The Memorial Park Biking Trails in Houston, Texas, offer a versatile and extensive network for cyclists, as shown in Fig. 7.25. Bicycles are permitted on various paved areas, including the Picnic Loop, the Hike-Bike Trail on the southern edge of Memorial Drive, roads, and the Outer Loop Trail. This allows for a variety of riding experiences, from leisurely loops to more extensive rides. Open daily from 5 am to 11 pm, the trails provide ample opportunity for early morning or evening rides. Located at 7575 North Picnic Lane, Houston, Texas 77007, the trails start at four miles in length, making Memorial Park a convenient and popular destination for local cyclists and visitors.

George Bush Park offers cyclists a diverse range of terrains, from open grasslands to wooded areas, catering to riders of all skill levels, as shown in Fig. 7.26. With its vast expanse and numerous trail options, the park is ideal for both extended rides and leisurely strolls, making it a popular spot for local residents and visitors seeking an active outdoor experience. Open daily from 7:00 am to 10:00 pm, the park's trails cover a length of 11.2 miles, providing ample space for exploration. Located at 16756 Westheimer Parkway, Houston, Texas, 77082, George Bush Park is a key destination for cycling enthusiasts in the region.



Fig. 7.26 George Bush Park.

Texas A&M University College Station is one of the bike-friendly campuses in the USA, and It has vast dedicated bikes over the whole campus, as shown in Fig. 7.27. Table 7.15 compares expected power generation from SEGPs on three prominent bike trails in Houston: Heights Hike & Bike Trail, Memorial Park, and George Bush Park. Each location is equipped with 1,667 bikes and employs two types of SEGP units, $SEGP_{1X}$ and $SEGP_{2X}$.

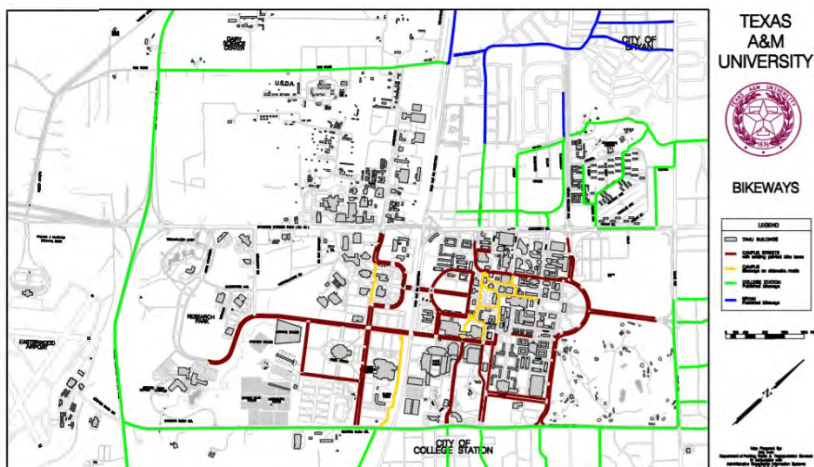


Fig. 7.27 Bike Lanes in TAMU, College Station [113].

TABLE 7.15

EXPECTED GENERATION ON THESE DIFFERENT TRAILS FROM SEGP_s

Location	No. bikes	Distance (miles)	Sources	Power (kWh/day)	Power (kWh/year)
Heights Hike & Bike Trail, Houston	1667	4.6	SEGP _{1X}	157	57,470
			SEGP _{2X}	247.42	90310.95
Memorial Park, Houston	1667	4.0	SEGP _{1X}	136.92	49974.43
			SEGP _{2X}	215.15	78531.25
George Bush Park, Houston	1667	11.2	SEGP _{1X}	383.37	139928.43
			SEGP _{2X}	602.43	219887.52
TAMU, College Station, Houston	1800	6.0	SEGP _{1X}	221.4	80811
			SEGP _{2X}	348.47	127191.55

For the Heights Hike & Bike Trail, which spans 4.6 miles, SEGP_{1X} units will generate 157 kWh/day, resulting in an annual power output of 57,470 kWh. SEGP_{2X} units, being more efficient, will produce 247.42 kWh/day, totaling 90,310.95 kWh per year. Memorial Park has a slightly shorter trail length of 4.0 miles and has lower power generation figures. SEGP_{1X} units here will generate 136.92 kWh/day, amounting to

49,974.43 kWh annually, while SEGP_{2X} units will produce 215.15 kWh/day, equating to 78,531.25 kWh per year, with its extensive 11.2-mile trail. George Bush Park significantly outperforms the other two locations in terms of power generation due to its longer distance. SEGP_{1X} units in George Bush Park will generate 383.37 kWh/day, which totals 139,928.43 kWh annually. SEGP_{2X} units in the same park will produce 602.43 kWh/day, leading to an impressive 219,887.52 kWh per year. TAMU campus has a slightly shorter trail length of 6.0 miles and has lower power generation figures. SEGP_{1X} units at TAMU will generate 221.4 kWh/day, amounting to 80,811 kWh annually, while SEGP_{2X} units will produce 348.47 kWh/day, equating to 127,191.55 kWh per year. This comparison highlights the power generation capabilities of SEGPs, Showcasing the potential of energy solutions within urban bike trails and proving the feasibility and benefits of utilizing SEGPs.

7.5 Comparison of Results

The SEGP system is completely novel and innovative compared to other existing systems available in the literature. The thin-film PZT-based SEGP system shows significant improvements compared to the most successful PEH system for the road developed, which uses a PZT stack by the University of California Merced research team [71, 114]. The PEH system utilized a 6 x 10-inch PZT stack as a unit. A 4.5 square feet PEH system equates to 12,192 thin-film PZT cells. The output with a Nissan car weight was 0.12 W/square feet/car by PEH. With the same amount of PZT stack, the thin-film-based SEGP system will have 22 units of 1X-SEGP (110 square feet) and 11 units of 2X-SEGP (55 square feet) and will produce 4-6 (0.33-67 W) times more energy than PEH, the only difference being that SEGP is limited to bike or e-bike lanes. In addition, the implementation of PZT rod or PZT stack-based PEH systems requires digging a road 12-

15 inches, which poses practical and logistical challenges. In contrast, the SEGP developed in this work does not require road damage. It can simply be placed on the road surface and secured with bitumen.

DSCS system developed in this work provides an innovative solution for fluctuating and lower energy generation systems. The literature [71, 114] shows that a significant amount of energy, around 30%, is lost from PEH's total energy due to inefficient energy collection systems. Other works [68 -69] show efficiencies of 82.8% and 88.1% [68-69]. In addition, these systems [68, 69, 71, 114] are not designed for lower-watt energy generation. The DSCS system developed in this work has a 92-95% efficiency and can be used in low-power systems.

Considering the economic perspective, the research work of the PEH tower by the University of California at Merced researchers shows that the energy generation of 1 unit of the PEH tower (4.5 feet² or 1.32 m²) was 0.42 kWh/m²/year/car. The energy generation cost is \$9,000/kW [71, 114], so the generation cost for 0.42 kWh/m²/year/car was \$3780. In order to produce the same amount of energy from SEGPs, only 15 square feet of SEGPs are required. The development cost of 15 square feet of SEGPs is less than \$300, which is 13 times less than the cost of the PEH system [71, 114].

Extensive research work was done to reduce the gap between simulation and prototype results. It was observed that in the simulation, every PZT cell received the same pressure and bending stress. Hence, each of the PZT cells produced the same energy, resulting in high energy generation in the simulation. On the other hand, in the prototypes, every PZT cell of the SEGPs does not receive the same pressure, so its power generation is lower. Another issue is that all PZT cells are active in the simulation, but in the prototype,

only 70% of the PZT cells are active due to manufacturing defects. It is suggested that this issue can be resolved by developing a mechanism to automate the manufacturing process without human touch, leading to a projected improvement in performance by 20-30%.

7.6 Summary

This chapter thoroughly examined the experimental results and analyses of various energy-generating systems. The characteristics of PZT cells were analyzed through the experimental outcomes of different AEH layers, including 1X, 2X, and 3X layers. A comparison between the energy outputs of PZT and PV systems was provided. The SEGP system was analyzed, focusing on the EGP, SEGP_{1X}, and SEGP_{2X} configurations. Additionally, the performance of a DSCS connected to SEGPs and lithium batteries was evaluated through various case studies. The chapter concluded with a discussion of potential implementation scenarios for various locations, providing comprehensive insights into the energy generation, efficiency, and practicality of these innovative SEGP technologies.

CHAPTER 8

CONCLUSIONS AND FUTURE WORKS

8.1 Conclusions

The global climate crisis underscores the urgent need to transition to renewable energy sources. As a result, research on sustainable energy-generating systems is of great importance. PZT cells can be an alternative energy-generating source. However, PZT cells have several challenges, such as their brittleness and low frequency of operation, which lead to their performance degradation. In addition, there is significant energy generation loss in PZT-based energy systems. The objectives of this work were to develop a novel sustainable energy generating pad (SEGP) as an alternative energy source utilizing a thin-film PZT cell and to prototype a dual-stage smart energy storage system for SEGP's efficient energy management.

This research work developed a SEGP for energy generation for lightweight vehicles such as bicycles and electric bikes. SEGP comprises multiple layers of thin-film PZT cells and multi-composite materials to convert mechanical vibrations into electricity. A DSCS system was developed to ensure stable operation and maximize energy storage, especially for any lower energy generating system. Twelve different types of prototypes of SEGP were developed and analyzed to identify the efficient SEGP system. The destructive and failure analysis was conducted on the SEGP_{1X} to determine the SEGP performance, efficiency, and longevity.

Additional analysis was conducted to integrate SEGP technology with existing PV systems for practical implementation purposes, creating a hybrid grid-tie microgrid system.

This system optimizes energy generation and utilization, supporting essential services such as water purification and e-charging for lightweight vehicles and mobiles, and allowing surplus energy to be sold to utility companies. The analysis demonstrated that SEGP systems, particularly when integrated with existing PV systems into hybrid grid-tie microgrid configurations, offer promising voltage stability of around 98-100% and returns on investment of 5.9-7 years on ten-year projects. This makes them economically sustainable for large-scale implementation.

The key contributions of this research are:

1. A novel SEGP system, consisting of multiple layers of thin-film PZT cells, energy collector circuits, and multi-composite material layers, was developed to effectively convert mechanical vibrations and kinetic energy from lightweight vehicles into clean electricity. Simulation studies showed that SEGP_{1X} and SEGP_{2X} could generate between 0.59–1.35 W and 1.42–3.42 W per ride, respectively. These findings were in agreement with the results of prototype testing, which had 0.33–0.41 W per ride and 0.54–0.67 W per ride for SEGP_{1X} and SEGP_{2X}, respectively. The SEGP system is completely novel and innovative compared to other existing systems. The SEGP developed in this work is less expensive than the PZT stack of other researchers [71, 114]. In addition, the developed SEGP system can be placed on a road surface and be secured with bitumen. Other the other hand, the PZT rod or PZT stack-based PEH systems require digging the road 12-15 inches, which poses practical and logistical challenges [71, 114].
2. The development of a dual-stage lithium battery charging (DSCS) system ensured efficient energy storage and stable operation. With a round-trip efficiency of

approximately 92-95%. The DSCS system is well-suited to manage the non-sinusoidal output voltage characteristic of SEGP systems, ensuring maximum generated energy storage in the lithium battery. The DSCS system provided an innovative solution for fluctuating and lower energy generation systems. The developed DSCS system had a maximum efficiency of 92-95%. Meanwhile, the efficiencies of other comparable systems are around 30% [71, 114], 82.9% [68], and 88.1% [69]. In addition, an analysis performed between the SEGP and that of the PZT stack-based PEH systems showed that the development cost of the SEGP system is less than that of the PEH system.

8.2 Future Works

Monash University Malaysia will implement the 1X-Layer of the Sustainable Energy Generating Pad (SEGP_{1X}) on its campus within the next few months. This real-world application will help assess the pros and cons of the SEGP system. Further work on the SEGP materials can reduce around 50% of the cost of SEGP production by reducing the SEGP layers, the AC-DC conversion system, and the connection wires. Developing a new hydrophobic liquid may reduce costs and increase energy-generating performance by 10-15%. The expensive hydrophobic liquid increases the cost by 10 % and lowers energy-generating performance by around 15%.

The long-term visionary goal of this technology is to convert this SEGP_{2X} bike lane to vehicle lanes with the same performance and efficiency. If it can be done, it will revolutionize energy generation worldwide. For example, after converting SEGP_{2X} to vehicle lanes and establishing it on a one-mile distance of Katy Freeway (I-10) in Houston.

According to the Texas Department of Transportation, 200,000 to 300,000 vehicles run daily on I-10 [112]. Thus, the generation will be between 78,000 to 117,000 kWh.

Future research work will focus on developing 3X layers of SEGP to achieve higher energy output, expecting a yield of six times more energy than that of the 1X layer. Successful development of the 3X layer of SEGP in the EWC system could pave the way for mass-scale implementation, transitioning from e-bike charging to Electric Vehicle (EV) charging stations.

REFERENCES

- [1] H. Zhu *et al.*, "Energy Storage in High Variable Renewable Energy Penetration Power Systems: Technologies and Applications," in *CSEE Journal of Power and Energy Systems*, vol. 9, no. 6, pp. 2099-2108, November 2023, doi: 10.17775/CSEEPES.2020.00090.
- [2] H. Jain, B. Mather, A. K. Jain and S. F. Baldwin, "Grid-Supportive Loads—A New Approach to Increasing Renewable Energy in Power Systems," in *IEEE Transactions on Smart Grid*, vol. 13, no. 4, pp. 2959-2972, July 2022, doi: 10.1109/TSG.2022.3153230.
- [3] J. Li, Z. Fang, Q. Wang, M. Zhang, Y. Li and W. Zhang, "Optimal Operation with Dynamic Partitioning Strategy for Centralized Shared Energy Storage Station with Integration of Large-scale Renewable Energy," in *Journal of Modern Power Systems and Clean Energy*, vol. 12, no. 2, pp. 359-370, March 2024, doi: 10.35833/MPCE.2023.000345.
- [4] F. Angizeh, J. Bae, J. Chen, A. Klebnikov and M. A. Jafari, "Impact Assessment Framework for Grid Integration of Energy Storage Systems and Renewable Energy Sources Toward Clean Energy Transition," in *IEEE Access*, vol. 11, pp. 134995-135005, 2023, doi: 10.1109/ACCESS.2023.3337133.
- [5] F. Z. Peng, C. -C. Liu, Y. Li, A. K. Jain and D. Vinnikov, "Envisioning the Future Renewable and Resilient Energy Grids—A Power Grid Revolution Enabled by Renewables, Energy Storage, and Energy Electronics," in *IEEE Journal of Emerging and Selected Topics in Industrial Electronics*, vol. 5, no. 1, pp. 8-26, Jan. 2024, doi: 10.1109/JESTIE.2023.3343291.
- [6] C. Jena, J. M. Guerrero, A. Abusorrah, Y. Al-Turki and B. Khan, "Multi-Objective Generation Scheduling of Hydro-Thermal System Incorporating Energy Storage With Demand Side Management Considering Renewable Energy Uncertainties," in *IEEE Access*, vol. 10, pp. 52343-52357, 2022, doi: 10.1109/ACCESS.2022.3172500.
- [7] K. M. Kabir, S. Mazumder, M. S. U. Chowdhury, M. A. Matin, M. W. U. Forhad, and A. Mallick, "Design and analysis of a grid-connected hybrid power system with constant supply for Patenga, Bangladesh," *Cogent Engineering*, vol. 7, no. 1, 2020, Art. no. 1762524. doi: 10.1080/23311916.2020.1762524.
- [8] H. Wang, A. Jasim, and X. Chen. "Energy harvesting technologies in roadway and bridge for different applications—A comprehensive review." *Applied Energy*, vol. 212, pp 1083-1094, 2018.

- [9] C. Covaci and A. Gontean, "Two-Stage Converter for Piezoelectric Energy Harvesting using Buck Configuration," 2020 IEEE 26th International Symposium for Design and Technology in Electronic Packaging (SIITME), pp. 408-411, 2020.
- [10] A. Romani, M. Filippi, and M. Tartagni, "Micropower Design of a Fully Autonomous Energy Harvesting Circuit for Arrays of Piezoelectric Transducers," in *IEEE Transactions on Power Electronics*, vol. 29, no. 2, pp. 729-739, Feb. 2014,
- [11] F. Angizeh, J. Bae, J. Chen, A. Klebnikov and M. A. Jafari, "Impact Assessment Framework for Grid Integration of Energy Storage Systems and Renewable Energy Sources Toward Clean Energy Transition," in *IEEE Access*, vol. 11, pp. 134995-135005, 2023, doi: 10.1109/ACCESS.2023.3337133.
- [12] F. Z. Peng, C. -C. Liu, Y. Li, A. K. Jain and D. Vinnikov, "Envisioning the Future Renewable and Resilient Energy Grids—A Power Grid Revolution Enabled by Renewables, Energy Storage, and Energy Electronics," in *IEEE Journal of Emerging and Selected Topics in Industrial Electronics*, vol. 5, no. 1, pp. 8-26, Jan. 2024, doi: 10.1109/JESTIE.2023.3343291.
- [13] A. N. Randriantsoa, D. A. H. Fakra, L. Rakotondrajaona, and R. Benelmir, "Research and development of a new combination of piezo-thermoelectric energy harvester systems from roadways," *Engineering Research Express*, vol. 6, no. 1, p. 015112, Mar. 2024. <https://dx.doi.org/10.1088/2631-8695/ad2d98>.
- [14] T. Zhang, L. Kong, Z. Zhu, X. Wu, H. Li, Z. Zhang, and J. Yan, "An electromagnetic vibration energy harvesting system based on series coupling input mechanism for freight railroads," *Applied Energy*, vol. 353, pt. A, pp. 122047, 2024. <https://doi.org/10.1016/j.apenergy.2023.122047>.
- [15] C. Wang, R. Zhou, S. Wang, H. Yuan, and H. Cao, "Structure optimization and performance of piezoelectric energy harvester for improving road power generation effect," *Energy*, vol. 270, pp. 126896, 2023. <https://doi.org/10.1016/j.energy.2023.126896>.
- [16] Y. Cao, J. Li, A. Sha, Z. Liu, F. Zhang, and X. Li, "A power-intensive piezoelectric energy harvester with efficient load utilization for road energy collection: Design, testing, and application," *Journal of Cleaner Production*, vol. 369, pp. 133287, 2022. <https://doi.org/10.1016/j.jclepro.2022.133287>.
- [17] H. Ouro-Koura, Z. Sotoudeh, J. Tichy, and D.-A. Borca-Tasciuc, "Effectiveness of Energy Transfer versus Mixing Entropy in Coupled Mechanical–Electrical Oscillators," *Energies*, vol. 15, p. 6105, 2022. <https://doi.org/10.3390/en15176105>.

- [18] Y. Zhang, Q. Lai, J. Wang, and C. Lü, "Piezoelectric Energy Harvesting from Roadways under Open-Traffic Conditions: Analysis and Optimization with Scaling Law Method," in *Energies*, vol. 15, no. 9, p. 1-12, 2022, doi: 10.3390/en15093395.
- [19] K. Higashikawa, W. Bian, T. Kiss and S. M. Muyeen, "Energy Efficiency Improvement of Renewable-Rich DC Microgrids by SMES Cables," in *IEEE Transactions on Applied Superconductivity*, vol. 34, no. 3, pp. 1-5, May 2024, Art no. 5700205, doi: 10.1109/TASC.2023.3349361.
- [20] Y. Ma, Z. Hu and Y. Song, "Hour-Ahead Optimization Strategy for Shared Energy Storage of Renewable Energy Power Stations to Provide Frequency Regulation Service," in *IEEE Transactions on Sustainable Energy*, vol. 13, no. 4, pp. 2331-2342, Oct. 2022, doi: 10.1109/TSTE.2022.3194718.
- [21] V. E. Wissa, A. E. Badawy and A. El-Guindy, "Fault Ride-Through in Grid-Connected DC Microgrid to Improve Microgrid and Utility Grid Performance," 2023 IEEE PES Conference on Innovative Smart Grid Technologies - Middle East (ISGT Middle East), Abu Dhabi, United Arab Emirates, 2023, pp. 1-5, doi: 10.1109/ISGTMiddleEast56437.2023.10078453.
- [22] H. Park et al., "Self-assembly of unidirectionally polarized piezoelectric peptide nanotubes using environmentally friendly solvents," *Applied Surface Science*, vol. 618, p. 156588, 2023. [Online]. Available: <https://doi.org/10.1016/j.apsusc.2023.156588>.
- [23] H. N. Chamanyeta, A. M. R. Fath El-Bab, B. W. Ikua, and E. Murimi, "Development of a varying multi-cantilever beam frequency up conversion energy harvester," *Energy Conversion and Management: X*, vol. 16, p. 100290, 2022. [Online]. Available: <https://doi.org/10.1016/j.ecmx.2022.100290>.
- [24] N. Sezer and M. Koç, "A comprehensive review on the state-of-the-art of piezoelectric energy harvesting," *Nano Energy*, vol. 80, pp. 105567, 2021. <https://doi.org/10.1016/j.nanoen.2020.105567>.
- [25] C. Chen, T.-B. Xu, A. Yazdani, and J.-Q. Sun, "A high density piezoelectric energy harvesting device from highway traffic — System design and road test," *Applied Energy*, vol. 299, p. 117331, 2021. <https://doi.org/10.1016/j.apenergy.2021.117331>.
- [26] X. Wang, Y. Ye, Z. Chen, L. Qian, and L. Liu, "A Clockless Synergistic Hybrid Energy Harvesting Technique With Simultaneous Energy Injection and Sampling for Piezoelectric and Photovoltaic Energy," in *IEEE Transactions on Circuits and Systems I: Regular Papers*, vol. 70, no. 4, pp. 1795-1804, April 2023, doi: 10.1109/TCSI.2022.3233111.

- [27] H. Xiong and L. Wang, "Piezoelectric energy harvester for public roadway: On-site installation and evaluation," in *Applied Energy*, vol. 174, pp. 101-107, 2016, doi:10.1016/j.apenergy.2016.04.031.
- [28] P. Deepak and B. George, "Piezoelectric Energy Harvesting From a Magnetically Coupled Vibrational Source," in *IEEE Sensors Journal*, vol. 21, no. 3, pp. 3831-3838, Feb. 2021, doi: 10.1109/JSEN.2020.3025216.
- [29] J. Pei, B. Zhou, and L. Lyu, "e-Road: The largest energy supply of the future?," in *Applied Energy*, vol. 241, pp. 174-183, 2019, ISSN 0306-2619, doi:10.1016/j.apenergy.2019.03.033.
- [30] S. Li, A. Roy and B. H. Calhoun, "A Piezoelectric Energy-Harvesting System With Parallel-SSHI Rectifier and Integrated Maximum-Power-Point Tracking," in *IEEE Solid-State Circuits Letters*, vol. 2, no. 12, pp. 301-304, Dec. 2019, doi: 10.1109/LSSC.2019.2951394.
- [31] C. Chen, T.-B. Xu, A. Yazdani, and J.-Q. Sun, "A high density piezoelectric energy harvesting device from highway traffic — System design and road test," in *Applied Energy*, vol. 299, p. 1-8, 2021, doi: 10.1016/j.apenergy.2021.117331.
- [32] C. Wang, J. Zhao, Q. Li, and Y. Li, "Optimization design and experimental investigation of piezoelectric energy harvesting devices for pavement." in *Applied energy*, Vol. 229, pp.18-30, 2018, doi: 10.1016/j.apenergy.2018.07.036.
- [33] J. Park, et al., "Enhancing the Performance of PZT-Based Piezoelectric Generators through Nanostructure Engineering," in *Nano Energy*, vol. 105, p. 105461, 2023.
- [34] C. H. Yang, Y. Song, M. S. Woo, J. H. Eom, G. J. Song, J. H. Kim, J. Kim, T. H. Lee, J. Y. Choi, and T. H. Sung, "Feasibility study of impact-based piezoelectric road energy harvester for wireless sensor networks in smart highways," in *Sensors and Actuators A: Physical*, vol. 261, pp. 317-324, 2017, doi: 10.1016/j.sna.2017.04.025.
- [35] Y. Zhang, Q. Lai, J. Wang, and C. Lü, "Piezoelectric Energy Harvesting from Roadways under Open-Traffic Conditions: Analysis and Optimization with Scaling Law Method," in *Energies*, vol. 15, no. 9, p. 1-12, 2022, doi: 10.3390/en15093395.
- [36] H. Yuan, S. Wang, C. Wang, Z. Song, and Y. Li, "Design of piezoelectric device compatible with pavement considering traffic: Simulation, laboratory and on-site," in *Applied Energy*, vol. 306, Part B, pp. 1-13, 2022, doi: 10.1016/j.apenergy.2021.118153.
- [37] Gupta, M. Kumar, G. Singh, and A. Chanda, "Development of a novel footwear based power harvesting system," in *e-Prime - Advances in Electrical Engineering*,

- Electronics and Energy, vol. 3, p. 1-10, 2023, doi:10.1016/j.prime.2023.100115.
- [38] G. del Castillo-García, E. Blanco-Fernandez, P. Pascual-Muñoz, and D. Castro-Fresno, "Energy harvesting from vehicular traffic over speed bumps: a review," in *Proceedings of the Institution of Civil Engineers - Energy*, vol. 171, no. 2, pp. 58-69, 2018. doi: 10.1680/jener.17.00008.
- [39] M. Gholikhani, H. Roshani, S. Dessouky, and A.T. Papagiannakis, "A critical review of roadway energy harvesting technologies," *Applied Energy*, vol. 261, 2020, Art. no. 114388. Doi: 10.1016/j.apenergy.2019.114388.
- [40] P. Tan, Y. Xi, S. Chao, D. Jiang, Z. Liu, Y. Fan, and Z. Li, "An Artificial Intelligence-Enhanced Blood Pressure Monitor Wristband Based on Piezoelectric Nanogenerator," *Biosensors*, vol. 12, p. 234, 2022. <https://doi.org/10.3390/bios12040234>.
- [41] H. Zhou, Y. Zhang, Y. Qiu, H. Wu, W. Qin, Y. Liao, Q. Yu, and H. Cheng, "Stretchable piezoelectric energy harvesters and self-powered sensors for wearable and implantable devices." In *Biosensors and Bioelectronics, 1 vol.* 168 pp. 1-20, 2020, doi: 10.1016/j.bios.2020.112569.
- [42] M. R. Kiran, O. Farrok, M. Abdullah-Al-Mamun, M. R. Islam and W. Xu, "Progress in Piezoelectric Material Based Oceanic Wave Energy Conversion Technology," in *IEEE Access*, vol. 8, pp. 146428-146449, 2020, doi: 10.1109/ACCESS.2020.3015821.
- [43] D. Ma, G. Lan, W. Xu, M. Hassan and W. Hu, "Simultaneous Energy Harvesting and Gait Recognition Using Piezoelectric Energy Harvester," in *IEEE Transactions on Mobile Computing*, vol. 21, no. 6, pp. 2198-2209, Jun. 2022, doi: 10.1109/TMC.2020.3035045.
- [44] G. D. Ram, T. Aravind, S. P. Kumar, U. Hariharan, G. Jeyachandran and G. Goutham, "Simple Piezoelectric based MEMS Energy Harvester Design and Simulation," 2022 International Conference on Automation, Computing and Renewable Systems (ICACRS), Pudukkottai, India, 2022, pp. 1-4, doi: 10.1109/ICACRS55517.2022.10029083.
- [45] J. Zhang, Y. He, C. Boyer, K. Kalantar-Zadeh, S. Peng, D. Chu, and C. H. Wang, "Recent developments of hybrid piezo-triboelectric nanogenerators for flexible sensors and energy harvesters," *Nanoscale Adv.*, vol. 3, no. 19, pp. 5465-5486, 2021. [Online]. Available: <https://doi.org/10.1039/D1NA00501D>.
- [46] L. Peng, Y. Qi, J. Liu, Y. Sun, H. Zu and X. Ru, "Contact and Non-Contact Dual-Piezoelectric Energy Harvesting System Driven by Cantilever Vibration," in *IEEE*

- Access, vol. 10, pp. 111974-111984, 2022, doi: 10.1109/ACCESS.2022.3215541.
- [47] L. Lu, W. Ding, J. Liu, and B. Yang "Flexible PVDF based piezoelectric nanogenerators." in *Nano Energy*, vol. 78 pp. 1-22, 2020, doi: 10.1016/j.nanoen.2020.105251.
- [48] S. Gareh, B. C. Kok, C. Uttraphan, K. T. Thong and A. A. Borhana, "Evaluation of piezoelectric energy harvester outcomes in road traffic applications," 4th IET Clean Energy and Technology Conference (CEAT 2016), Kuala Lumpur, Malaysia, 2016, pp. 1-5, doi: 10.1049/cp.2016.1269.
- [49] A. R. G. D. Silveira, and G. B. Daniel. "Optimization analysis of an energy harvester for smart tilting pad journal bearings considering higher vibration modes." in *Mechanical Systems and Signal Processing*, vol. 166, pp. 1-18 2022, doi: 10.1016/j.ymsp.2021.108404.
- [50] T. Li and P.S. Lee, "Piezoelectric Energy Harvesting Technology: From Materials, Structures, to Applications," *Small Struct.*, vol. 3, p. 2100128, 2022, doi:10.1002/sstr.202100128.
- [51] Gupta, M. Kumar, G. Singh, and A. Chanda, "Development of a novel footwear-based power harvesting system," in *e-Prime - Advances in Electrical Engineering, Electronics and Energy*, vol. 3, p. 1-10, 2023, doi:10.1016/j.prime.2023.100115. doi: 10.1016/j.apenergy.2019.114388.
- [52] M. F. Wasim, S. Tayyaba, M. W. Ashraf, and Z. Ahmad, "Modeling and Piezoelectric Analysis of Nano Energy Harvesters," *Sensors*, vol. 20, no. 14, p. 3931, 2020. [Online]. Available: <https://doi.org/10.3390/s20143931>.
- [53] K. K. Das, B. Basu, P. Maiti, and A. K. Dubey, "Piezoelectric nanogenerators for self-powered wearable and implantable bioelectronic devices," *Acta Biomaterialia*, vol. 171, pp. 85-113, 2023. [Online]. Available: <https://doi.org/10.1016/j.actbio.2023.08.057>.
- [54] B. Zhao, F. Qian, A. Hatfield, L. Zuo, and T.-B. Xu, "A Review of Piezoelectric Footwear Energy Harvesters: Principles, Methods, and Applications," *Sensors*, vol. 23, p. 5841, 2023. [Online]. Available: <https://doi.org/10.3390/s23135841>.
- [55] H. G. Pisharody, "An optimal design for piezoelectric energy harvesting system." In *ISGT2011-India*, pp. 244-247. IEEE, 2011.
- [56] H. Robert, and Fredric C. Fletcher. "100% clean energy: The California conundrum." *The Electricity Journal* 32, vol. 2, pp. 31-36, 2019.

- [57] L. Huicong J. Zhong, C. Lee, S.W. Lee, and L. Lin. "A comprehensive review on piezoelectric energy harvesting technology: Materials, mechanisms, and applications." *Applied Physics Reviews*, Vol. 5, Issue 4 pp.): 041306-35, 2018.
- [58] S. Nurettin, and M. Koç. "A comprehensive review on the state-of-the-art of piezoelectric energy harvesting." *Nano Energy*, Vol. 80, pp 105569-75, 2021.
- [59] C. Wang, S. Wang, Z. Gao, and Z. Song, "Effect evaluation of road piezoelectric micro-energy collection-storage system based on laboratory and on-site tests," *Applied Energy*, vol. 287, p. 116581, 2021. <https://doi.org/10.1016/j.apenergy.2021.116581>.
- [60] A. Jasim, G. Yesner, H. Wang, A. Safari, A. Maher, and B. Basily, "Laboratory testing and numerical simulation of piezoelectric energy harvester for roadway applications," *Applied Energy*, vol. 224, pp. 438-447, 2018. <https://doi.org/10.1016/j.apenergy.2018.05.040>.
- [61] C. Wang, G. Yu, H. Cao, S. Wang, and Y. Li, "Structure simulation optimization and test verification of piezoelectric energy harvester device for road," *Sensors and Actuators A: Physical*, vol. 315, p. 112322, 2020. <https://doi.org/10.1016/j.sna.2020.112322>.
- [62] B. Lafarge, S. Grondel, C. Delebarre, and E. Cattan, "A validated simulation of energy harvesting with piezoelectric cantilever beams on a vehicle suspension using Bond Graph approach," *Mechatronics*, vol. 53, pp. 202-214, 2018. [Online]. Available: <https://doi.org/10.1016/j.mechatronics.2018.06.004>.
- [63] A. Mahajan, A. Goel, and A. Verma, "A review on energy harvesting based piezoelectric system," *Materials Today: Proceedings*, vol. 43, pt. 1, pp. 65-73, 2021. <https://doi.org/10.1016/j.matpr.2020.11.210>.
- [64] H. Zhang, K. Huang, Z. Zhang, T. Xiang, and L. Quan, "Piezoelectric Energy Harvesting From Roadways Based on Pavement Compatible Package," *ASME J. Appl. Mech.*, vol. 86, no. 9, p. 091012, Sep. 2019. [Online]. Available: <https://doi.org/10.1115/1.4044140>.
- [65] A. Sherren, K. Fink, J. Eshelman, L. Y. Taha, S. Anwar, and C. Brennecke, "Design and Modeling of Piezoelectric Road Energy Harvesting," *Open Journal of Energy Efficiency*, vol. 11, pp. 24-36, 2022. [Online]. Available: <https://doi.org/10.4236/ojee.2022.112003>.
- [66] Flora Guo, "Investigating the Viability of a Piezoelectric Insole to Harvest Kinetic Energy," *Future Science Leaders Blog*, Jun. 2020. [Online]. Available: <https://www.futurescienceleaders.com/blog/2020/06/investigating-the-viability-of-a->

piezoelectric-insole-to-harvest-kinetic-energy/.

- [67] N. Zabihi and M. Saafi, "Recent Developments in the Energy Harvesting Systems from Road Infrastructures," *Sustainability*, vol. 12, no. 17, p. 6738, 2020. [Online]. Available: <https://doi.org/10.3390/su12176738>.
- [68] I. C. Chen, C. -W. Liang and T. -H. Tsai, "A Single-Inductor Dual-Input Dual-Output DC–DC Converter for Photovoltaic and Piezoelectric Energy Harvesting Systems," in *IEEE Transactions on Circuits and Systems II: Express Briefs*, vol. 66, no. 10, pp. 1763-1767, Oct. 2019, doi: 10.1109/TCSII.2019.2921349.
- [69] X. Wang *et al.*, "A Clockless Synergistic Hybrid Energy Harvesting Technique With Simultaneous Energy Injection and Sampling for Piezoelectric and Photovoltaic Energy," in *IEEE Transactions on Circuits and Systems I: Regular Papers*, vol. 70, no. 4, pp. 1795-1804, April 2023, doi: 10.1109/TCSI.2022.3233111.
- [70] H. Xiong and L. Wang, "Piezoelectric energy harvester for public roadway: On-site installation and evaluation," *Applied Energy*, vol. 174, pp. 101-107, 2016. <https://doi.org/10.1016/j.apenergy.2016.04.031>.
- [71] C. Chen, T.-B. Xu, A. Yazdani, and J.-Q. Sun, "A high density piezoelectric energy harvesting device from highway traffic — System design and road test," *Applied Energy*, vol. 299, p. 117331, 2021. [Online]. Available: <https://doi.org/10.1016/j.apenergy.2021.117331>.
- [72] S.N. Vodapally and M.H. Ali, "A Comprehensive Review of Solar Photovoltaic (PV) Technologies, Architecture, and Its Applications to Improved Efficiency," *Energies*, vol. 16, p. 319, 2023. <https://doi.org/10.3390/en16010319>.
- [73] MIT News, "Perovskite tandem cells show potential to surpass silicon in solar power production." Feb 17, 2024, Retrieved from <https://www.technologyreview.com/2024/01/08/1085124/super-efficient-solar-cells-breakthrough-technologies/>.
- [74] K.A., Bush, K. Frohna, R. Prasanna, Y.B. Cheng, & M.I. Peters, "The status and prospects of tandem perovskite solar cells." in *Nature Energy*, 5(12), 982-994, 2020.
- [75] M.A. Green, & A. Ho-Baillie, "Perovskite solar cells: the birth of a new era in photovoltaics" in *ACS Energy Letters*, 2(4), 822-830, 2017.
- [76] M. I. Sil, S. Mukherjee, and K. Biswas. "A review of energy harvesting technology and its potential applications." *Environmental and Earth Sciences Research Journal*, vol.4, issue. 2, pp 33-38, 2017.

- [77] N. Meena "Charging and discharging characteristics of Lead acid and Li-ion batteries," 2014 POWER AND ENERGY SYSTEMS: TOWARDS SUSTAINABLE ENERGY, Bangalore, India, 2014, pp. 1-3, doi: 10.1109/PESTSE.2014.6805253.
- [78] G. Lee, D.-J. Shin, Y.-H. Kwon, S.-J. Jeong, and J.-H. Koh, "Optimized piezoelectric and structural properties of (Bi,Na)TiO₃–(Bi,K)TiO₃ ceramics for energy harvester applications," *Ceramics International*, vol. 42, no. 13, pp. 14355-14363, 2016. <https://doi.org/10.1016/j.ceramint.2016.05.184>.
- [79] N. Sezer and M. Koç, "A comprehensive review on the state-of-the-art of piezoelectric energy harvesting," *Nano Energy*, vol. 80, p. 105567, 2021. <https://doi.org/10.1016/j.nanoen.2020.105567>.
- [80] S. Huang et al., "Multifunctional PVDF/CeO₂@PDA nanofiber textiles with piezoelectric and piezo-phototronic properties for self-powered piezoelectric sensor and photodetector," *Chem. Eng. J.*, vol. 482, p. 148950, 2024. <https://doi.org/10.1016/j.cej.2024.148950>.
- [81] J. P. Jiao, H. Hasni, N. Lajnef, and A. H. Alavi, "Mechanical metamaterial piezoelectric nanogenerator (MM-PENG): Design principle, modeling, and performance," *Materials & Design*, vol. 187, 2020, <https://doi.org/10.1016/j.matdes.2019.108214>.
- [82] R. De Fazio, M. De Giorgi, D. Cafagna, C. Del-Valle-Soto, and P. Visconti, "Energy Harvesting Technologies and Devices from Vehicular Transit and Natural Sources on Roads for a Sustainable Transport: State-of-the-Art Analysis and Commercial Solutions," *Energies*, vol. 16, no. 7, p. 3016, Apr. 2023. <https://doi.org/10.3390/en16073016>.
- [83] L. Gu et al., "Enhancing the current density of a piezoelectric nanogenerator using a three-dimensional intercalation electrode," *Nat. Commun.*, vol. 11, no. 1, p. 1030, Feb. 2020. <https://doi.org/10.1038/s41467-020-14846-4>.
- [84] T. Li and P.S. Lee, "Piezoelectric Energy Harvesting Technology: From Materials, Structures, to Applications," *Small Struct.*, vol. 3, p. 2100128, 2022. <https://doi.org/10.1002/sstr.202100128>.
- [85] S. Bolisetty, M. Peydayesh, and R. Mezzenga, "Sustainable technologies for water purification from heavy metals: review and analysis," *Chem. Soc. Rev.*, vol. 48, pp. 463-491, 2019. DOI: 10.1039/c8cs00493e.
- [86] P. Wei et al., "Progress in Energy Storage Technologies and Methods for Renewable Energy Systems Application," *Appl. Sci.*, vol. 13, no. 9, p. 5626, 2023.

- <https://doi.org/10.3390/app13095626>.
- [87] Y. Xiao et al., "Economic potentials of energy storage technologies in electricity markets with renewables," *Energy Storage and Saving*, vol. 2, no. 1, pp. 370-391, 2023. <https://doi.org/10.1016/j.enss.2022.10.004>.
- [88] M. Jafari, A. Botterud, and A. Sakti, "Decarbonizing power systems: A critical review of the role of energy storage," *Renewable and Sustainable Energy Reviews*, vol. 158, p. 112077, 2022. <https://doi.org/10.1016/j.rser.2022.112077>.
- [89] J. Mitali, S. Dhinakaran, and A.A. Mohamad, "Energy storage systems: a review," *Energy Storage and Saving*, vol. 1, no. 3, pp. 166-216, 2022. <https://doi.org/10.1016/j.enss.2022.07.002>.
- [90] R. Mahmud, S.M. Moni, K. High, and M. Carbajales-Dale, "Integration of techno-economic analysis and life cycle assessment for sustainable process design – A review," *J. Cleaner Prod.*, vol. 317, p. 128247, 2021. <https://doi.org/10.1016/j.jclepro.2021.128247>.
- [91] W. Ma, X. Xue, and G. Liu, "Techno-economic evaluation for hybrid renewable energy system: Application and merits," *Energy*, vol. 159, pp. 385-409, Dec. 2018. <https://doi.org/10.1016/j.energy.2018.06.101>.
- [92] S.L.Y. Lo et al., "Techno-economic analysis for biomass supply chain: A state-of-the-art review," *Renewable and Sustainable Energy Reviews*, vol. 135, p. 110164, Jan. <https://doi.org/10.1016/j.rser.2020.110164>.
- [93] F.G. Albrecht, D.H. König, N. Baucks, and R.-U. Dietrich, "A standardized methodology for the techno-economic evaluation of alternative fuels – A case study," *Fuel*, vol. 194, pp. 511-526, Apr. 2017. <https://doi.org/10.1016/j.fuel.2016.12.003>.
- [94] Kabir, K.M. & Binzaid, S., (2024, February), Performance Analysis of Multi-Composite Layered Energy Harvesting from Thin-Film PZT with Smart Charging System, in IEEE Texas Power and Energy Conference (TPEC) 2024, pp. 1-5.
- [95] Kabir, K.M. & Binzaid, S., (2024, February), Techno-Economical Evaluation of an Integrated EWeCStation Utilizing Road Infrastructure for Hybrid Energy, Drinking Water, and EV Charging Services, in IEEE Texas Power and Energy Conference (TPEC) 2024, pp. 1-5.
- [96] Kabir, K.M. & Binzaid, S., (2024, January), Impact Analysis of Lithium-ion Battery Storage System for Sustainable Energy Generating Pad Applications, in IEEE Third International Conference on Power, Control and Computing Technologies (ICPC2T) 2024, pp.1-5.

- [97] Binzaid, S. and K. M. Kabir, (2024, January), Utilization of Road Infrastructure with a Hybrid of Solar PV and SEGP Energy for Drinking Water and eBike Charging Station, in IEEE Third International Conference on Power, Control and Computing Technologies (ICPC2T) 2024, Raipur, India, Jan. 2024, pp.1-5.
- [98] Kabir, K.M., Binzaid, S., & Attia, J. O., (2022, October), Portable Solar-Powered Smart System for Reverse Osmosis Process of Drinkable Rainwater, IEEE Global Energy Conference 2022, pp. 1-5, Turkey, IEEE.
- [99] Kabir, K.M., & Binzaid, S., (2022, October), Design and Implementation of a Sustainable Energy Generating Pad for Lightweight Transportation, IEEE Global Energy Conference 2022, pp. 1-4, Turkey, IEEE.
- [100] Kabir, K. M., S. Binzaid, & J. O. Attia, "An Experimental Model and Test of a Novel Sustainable Energy Pad for BikeLane Applications Paper presented at 2022 ASEE Gulf Southwest Annual Conference, Prairie View, Texas. pp -1-6, March, 2022, <https://peer.asee.org/39161>.
- [101] K. M. Kabir, and S. Binzaid, "Enhancing Reliability and Performance of Hybrid (PV and SEGP) Energy Island Microgrid Systems for Community Modernization," 2024 3rd IEEE International Conference on Power Electronics, Intelligent Control and Energy System (ICPEICES), Delhi, India, 2024, pp. 1-4.
- [102] Kabir, K.M. & Binzaid, S., (2024, March), Exploring and Comparing Multicomposite Layers Thin-Film PZT as a Future Alternative Energy Source for Roadway Generation, IEEE Transactions on Industrial Applications. – Under Review.
- [103] Kabir, K.M. & Binzaid, S., (2023, November), Innovation of a Sustainable Energy Generating Pad from Lightweight Vehicle Applications, *Elsevier- Energy Conversion and Management:X*, vol. 22, p. 100595, 2024. doi:10.1016/j.ecmx.2024.100595
- [104] Kabir, K.M. & S. Binzaid, (2024, August), Development of an Emulator of the Sustainable Energy Harvesting Pad System on a Bike Lane for Charging Lithium Batteries, *Microelectronic Engineering* – Accepted.
- [105] K. M. Kabir, S. Binzaid, J. O. Attia, and A. Annamalai " Techno-Economical Evaluation of Hybrid Energy, Water, and Charging (EWC) Systems for Roadside Facilities," IEEE Transactions on Industrial Applications. – Under Review.
- [106] S. Binzaid and K. M. Kabir, "Technologies for dual-stage charge collection and energy storage for alternative energy sources," WO2023225473A2, Nov 23, 2023.

- [107] S. Binzaid and K. M. Kabir, "Technologies for energy generating multilayer composite material for pad application in transportation systems," WO2023225474A1, Nov 23, 2023.
- [108] Autodesk. (n.d.). Piezoelectricity. Fusion 360 Blog. [Online]. Available: <https://www.autodesk.com/products/fusion-360/blog/piezoelectricity/> [Accessed: March 21, 2024].
- [109] Retrieved from [Online] [https://www.road-bike.co.uk/articles/average-speed.php#:~:text=Average%20speed%20%2D%20indications&text=Beginner%2C%20short%20distance%20\(say%2010,\)%3A%20average%20around%2016%2D19](https://www.road-bike.co.uk/articles/average-speed.php#:~:text=Average%20speed%20%2D%20indications&text=Beginner%2C%20short%20distance%20(say%2010,)%3A%20average%20around%2016%2D19), [Accessed on October 30, 2023].
- [110] Retrieved from [Online], <https://www.houstononthecheap.com/best-biking-trails-in-houston/>, [Accessed on January 30, 2024].
- [111] Retrieved from [Online], <https://urbanoutdoors.com/houston-bike-trails/>, [Accessed on January 30, 2024].
- [112] Texas Department of Transportation, "Annual Average Daily Traffic (AADT) Maps," [Online]. Available: <https://www.txdot.gov/search-results.html?text=texas&skip=0&top=50>. [Accessed: 02-Jun-2024].
- [113] Retrieved from [Online], <https://transport.tamu.edu/Alternative/bicycles/bikeshare.aspx>, [Accessed on January 30, 2024].
- [114] J.-Q. Sun, T.-B. Xu, and A. Yazdani, "Ultra-High Power Density Roadway Piezoelectric Energy Harvesting System," California Energy Commission, Energy Research and Development Division, Electric Program Investment Charge (EPIC), Pub. No. CEC-500-2023-036, Jun. 2023. [Online]. <https://www.energy.ca.gov/sites/default/files/2023-06/CEC-500-2023-036.pdf>.

APPENDICES

Appendix A

```

% Data from Table II
P1X30m_Wh = 18.57;
P1Xh_Wh = 37.14;

% Data from Table IV
P2X30m_Wh = 72;
P2Xh_Wh = 136;

% Data from Table VI
P3X30m_Wh = 126;
P3Xh_Wh = 256;

% Prepare data for comparison plots
x_values = {'P1X30m', 'P2X30m', 'P3X30m'};
y_values_30m = [P1X30m_Wh, P2X30m_Wh, P3X30m_Wh];

x_values_h = {'P1Xh', 'P2Xh', 'P3Xh'};
y_values_h = [P1Xh_Wh, P2Xh_Wh, P3Xh_Wh];

% Convert string labels to categorical arrays for plotting
x_values_cat = categorical(x_values);
x_values_h_cat = categorical(x_values_h);

% Create comparison plots
figure;
bar(x_values_cat, y_values_30m);
xlabel('AEH Layers');
ylabel('Energy (Wh)');
title('Comparison of Energy Generation at 30 minutes for Different AEH Layers');

figure;
bar(x_values_h_cat, y_values_h);
xlabel('AEH Layers');
ylabel('Energy (Wh)');
title('Comparison of Energy Generation per hour for Different AEH Layers');

```

Appendix B

```

% Data from the table
systems = {'Hybrid (PV & SEGP1X)', 'Hybrid (PV & SEGP2X)'};
total_generation = [3.08, 4.20]; % kWh/day

```

```

usable_energy = [2.68, 3.57]; % kWh/day
total_demand = [1.13, 1.13]; % kWh/day (same for both systems)
excess_energy = [1.55, 2.44]; % kWh/day

% Component breakdown (assumed breakdown for illustration)
pv_generation = [1.12, 1.12]; % Generation from PV
segp1x_generation = [1.96, 0]; % Generation from SEGP1X
segp2x_generation = [0, 3.08]; % Generation from SEGP2X

% Combine data for stacked bar plot
generation_data = [pv_generation; segp1x_generation; segp2x_generation]';
usable_energy_data = usable_energy';
total_demand_data = total_demand';
excess_energy_data = excess_energy';

% Create figure
figure;
hold on;

% Number of systems and number of bars per group
num_systems = length(systems);
num_categories = 4; % Total Generation, Usable Energy, Total Demand, Excess Energy
bar_width = 0.2; % Width of each bar within the group

% X positions for each category
x = 1:num_systems;
x_positions = [x - 1.5*bar_width, x - 0.5*bar_width, x + 0.5*bar_width, x +
1.5*bar_width];

% Plot for Total Generation (stacked)
b1 = bar(x - 1.5*bar_width, generation_data, bar_width, 'stacked');
% Plot for Usable Energy
b2 = bar(x - 0.5*bar_width, usable_energy_data, bar_width, 'FaceColor', 'flat');
% Plot for Total Demand
b3 = bar(x + 0.5*bar_width, total_demand_data, bar_width, 'FaceColor', 'flat');
% Plot for Excess Energy
b4 = bar(x + 1.5*bar_width, excess_energy_data, bar_width, 'FaceColor', 'flat');

% Set colors for stacked bars (Total Generation)
b1(1).FaceColor = [0.8500, 0.3250, 0.0980]; % PV
b1(2).FaceColor = [0.9290, 0.6940, 0.1250]; % SEGP1X
b1(3).FaceColor = [0.4940, 0.1840, 0.5560]; % SEGP2X

% Set colors for single bars (Usable Energy, Total Demand, Excess Energy)
b2.FaceColor = [0.3010, 0.7450, 0.9330]; % Usable Energy

```

```

b3.FaceColor = [0.6350, 0.0780, 0.1840]; % Total Demand
b4.FaceColor = [0.4660, 0.6740, 0.1880]; % Excess Energy

% Set x-axis labels
set(gca, 'XTick', x, 'XTickLabel', systems);
xlabel('Hybrid Systems');
ylabel('Energy (kWh/day)');
title('Comparison of Hybrid EWC Systems');
legend([b1(1), b1(2), b1(3), b2, b3, b4], {'PV Generation', 'SEGP1X Generation',
'SEGP2X Generation', 'Usable Energy', 'Total Demand', 'Excess Energy'}, 'Location',
'NorthWest');
grid on;
hold off;

% Adjust x-axis to fit grouped bars
xlim([0.5, num_systems + 0.5]);

```

Appendix C

```

% Data from the table
systems = {'Hybrid (PV & SEGP1X)', 'Hybrid (PV & SEGP2X)'};
total_generation = [3.08, 4.20]; % kWh/day
usable_energy = [2.68, 3.57]; % kWh/day
total_demand = [1.13, 1.13]; % kWh/day (same for both systems)
energy_to_utility = [1.33, 2.09]; % kWh/day

% Component breakdown (assumed breakdown for illustration)
pv_generation = [1.12, 1.12]; % Generation from PV
segp1x_generation = [1.96, 0]; % Generation from SEGP1X
segp2x_generation = [0, 3.08]; % Generation from SEGP2X

% Combine data for stacked bar plot
generation_data = [pv_generation; segp1x_generation; segp2x_generation]';
usable_energy_data = usable_energy';
total_demand_data = total_demand';
excess_energy_data = energy_to_utility';

% Create figure
figure;
hold on;

% Number of systems and number of bars per group
num_systems = length(systems);
num_categories = 4; % Total Generation, Usable Energy, Total Demand, Excess Energy
bar_width = 0.2; % Width of each bar within the group

```

```

% X positions for each category
x = 1:num_systems;
x_positions = [x - 1.5*bar_width, x - 0.5*bar_width, x + 0.5*bar_width, x +
1.5*bar_width];

% Plot for Total Generation (stacked)
b1 = bar(x - 1.5*bar_width, generation_data, bar_width, 'stacked');
% Plot for Usable Energy
b2 = bar(x - 0.5*bar_width, usable_energy_data, bar_width, 'FaceColor', 'flat');
% Plot for Total Demand
b3 = bar(x + 0.5*bar_width, total_demand_data, bar_width, 'FaceColor', 'flat');
% Plot for Excess Energy
b4 = bar(x + 1.5*bar_width, excess_energy_data, bar_width, 'FaceColor', 'flat');

% Set colors for stacked bars (Total Generation)
b1(1).FaceColor = [0.8500, 0.3250, 0.0980]; % PV
b1(2).FaceColor = [0.9290, 0.6940, 0.1250]; % SEGP1X
b1(3).FaceColor = [0.4940, 0.1840, 0.5560]; % SEGP2X

% Set colors for single bars (Usable Energy, Total Demand, Excess Energy)
b2.FaceColor = [0.3010, 0.7450, 0.9330]; % Usable Energy
b3.FaceColor = [0.6350, 0.0780, 0.1840]; % Total Demand
b4.FaceColor = [0.4660, 0.6740, 0.1880]; % Excess Energy

% Set x-axis labels
set(gca, 'XTick', x, 'XTickLabel', systems);
xlabel('Hybrid Systems');
ylabel('Energy (kWh/day)');
title('Comparison of Hybrid Grid-tie EWC Systems');
legend([b1(1), b1(2), b1(3), b2, b3, b4], {'PV Generation', 'SEGP1X Generation',
'SEGP2X Generation', 'Usable Energy', 'Total Demand', 'Energy to Grid'}, 'Location',
'NorthWest');
grid on;
hold off;

% Adjust x-axis to fit grouped bars
xlim([0.5, num_systems + 0.5]);

```

Appendix D

```

% Given coefficients and values
av = 0.709667; % V/(lbs·mm·s)

```

```

bv = 0.00007072; % A/mm
cv = -0.00038036; % m/(V·s)
ai_base = 0.00018; % A, current at 150 lbs
ai_range = 0.00041 - 0.00018; % Range from 150 to 450 lbs
ai_max = 0.00041; % Maximum current for weights above 450 lbs

% Input variables
weight = input('Enter bike and rider weight (in lbs): ');
diameter = input('Enter PZT diameter (in mm): ');
speed = input('Enter bike speed (in mph): ');
N = input('Enter No of Cell: ');

% Set constant voltage
V = 110; % Voltage in volts

% Check if weight exceeds 450lbs
if weight > 450
    % If weight exceeds 450lbs, set voltage to zero and use the maximum current
    V = 0;
    I = ai_max;
    Pcell = 0;
    P_total = 0;

    else
    % Calculate voltage
    Vcell = av * weight + bv * diameter + cv * speed;
    Vcell2 = Vcell;

    % Calculate current using linear interpolation
    ai = ai_base + ai_range * ((weight - 150) / (450 - 150));
    Icell2 = ai*2.4;

    % Display the results
    fprintf('Voltage (Vcell): %.3f V\n', V);
    fprintf('Current (Icell): %.6f A\n', ai);
    fprintf('Voltage (Vcell2): %.3f V\n', V);
    fprintf('Current (Icell2): %.6f A\n', Icell2);

    % Calculate power generated
    Pcell = V * ai;
    fprintf('Power generated (Pcell): %.10f W\n', Pcell);
    Pcell2 = V * Icell2;
    fprintf('Power generated (Pcell2): %.10f W\n', Pcell2);

    % Calculate total power (P_1xtotal)

```

```

P_1xtotal = Pcell*N;
% Calculate total power (P_2xtotal)
P_2xtotal = Pcell2*N;

end

% Display the total power
fprintf('Total power (P_1xtotal): %.5f W\n', P_1xtotal);
% Display the 2x total power
fprintf('Total power (P_2xtotal): %.5f W\n', P_2xtotal);

```

Appendix E

```

% Input variables
PZT_diameter = input('Enter PZT diameter (in meters): ');
bike_weight_lbs = input('Enter bike and rider weight (in pounds): ');
bike_speed_mph = input('Enter bike speed (in mph): ');
C = input('Enter capacitance (in farads): '); % Capacitance in farads
dV_dt = input('Enter rate of voltage change (in volts per second): ');

% Fixed voltage
V = 110; % Voltage in volts

% Convert weight to kilograms
bike_weight_kg = bike_weight_lbs / 2.20462;

% Convert speed to meters per second
v = bike_speed_mph * 0.44704;

% Calculate radius
r = PZT_diameter / 2;

% Calculate centripetal acceleration
a = v^2 / r;

% Calculate force
F = bike_weight_kg * a;

% Calculate the piezoelectric coefficient
d = V / F;

% Calculate current
I = C * dV_dt;

```

```

% Display the results
fprintf('Force applied to PZT: %.2f N\n', F);
fprintf('Piezoelectric coefficient: %.6f V/m\n', d);
fprintf('Current: %.6f A\n', I);

% Fixed voltage
V = 110; % Voltage in volts

% Desired current
I_desired = 0.19e-3; % Current in amperes (0.19 milliAmperes)

% Input the rate of voltage change (dV/dt)
dV_dt = input('Enter rate of voltage change (in volts per second): ');

% Calculate the required capacitance
C = I_desired / dV_dt;

% Display the required capacitance
fprintf('Required Capacitance: %.10f F\n', C);

```

Appendix F

```

/*
  CRO Project solar based water purification
*/
#include <Q2HX711.h>

int sensor1Pin = A0; // select the input sensor 1
int led1Pin = 2; //rain on/pff
int sensor1Value = 0; // variable to store the value coming from the sensor

const byte MPS_OUT_pin = 3; // OUT data pin
const byte MPS_SCK_pin = 4; // clock data pin
int avg_size = 6; // #pts to average over
Q2HX711 MPS20N0040D(MPS_OUT_pin, MPS_SCK_pin); // start comm with the
HX710B

const int motor = 5;

int sensor2Pin = A1; // select the input sensor 2
int relay1 = 7; //rain on/pff

```

```

int sensor2Value = 0; // variable to store the value coming from the sensor

int sensor3Pin = A2; // select the input sensor 3
int relay2 = 8; //rain on/pff
int sensor3Value = 0; // variable to store the value coming from the sensor

int sensor4Pin = A3; // select the input sensor 4
int relay3 = 9; //rain on/pff
int sensor4Value = 0; // variable to store the value coming from the sensor
//The setup function runs once when you press reset or power the board

void setup()
{
  Serial.begin(9600); // start the serial port
  pinMode(led1Pin, OUTPUT);
  pinMode(relay1, OUTPUT);
  pinMode(relay2, OUTPUT);
  pinMode(relay3, OUTPUT);
  pinMode(motor, OUTPUT);
}

void loop()
{
  sensor1Value = analogRead(sensor1Pin);
  if (sensor1Value >= 1020) // turn the ledPin on (>= 1020 mean water sensing)
    {digitalWrite(led1Pin, HIGH);} // stop the program for <sensorValue> milliseconds;}
  else
    {digitalWrite(led1Pin, LOW); } // stop the program for for <sensorValue>
milliseconds:

  sensor2Value = analogRead(sensor2Pin);
  if (sensor2Value <= 1000) // turn the ledPin on
    {digitalWrite(relay1, LOW); // stop the program for realy 1 off
    digitalWrite(motor, LOW); } // stop the program for for motor off
  else
    {digitalWrite(motor, HIGH);}
  sensor3Value = analogRead(sensor3Pin);
  if (sensor3Value >= 1020) // water level high
    {digitalWrite(relay1, LOW); // stop the program for realy 1 off
    digitalWrite(motor, LOW); } // stop the program for for motor off
  else
    {digitalWrite(relay1, HIGH); // stop the program for realy 1 off

```



```

    digitalWrite(motor, HIGH); } // stop the program for for motor off

sensor4Value = analogRead(sensor4Pin);
if (sensor4Value <= 900) // water level low
    { //digitalWrite(relay1, HIGH); // stop the program for realy 1 off
    digitalWrite(motor, HIGH); } // stop the program for for motor off

    digitalWrite(motor, HIGH); // turn the motor on (HIGH is the voltage level)
double avg_val = 0.0; // variable for averaging
for (int i=0; i<=avg_size;i++)
    {
    avg_val += MPS20N0040D.read(); // add multiple ADC readings
    delay(50); // delay between readings
    }
avg_val /= avg_size;
Serial.println(avg_val,0); // print out the average
if (digitalRead(avg_val)<=6)
    {
    digitalWrite(motor, HIGH); // and turn on the motor
    } //
else
    { // otherwise...
    digitalWrite(motor,LOW); // and turn off the LED
    }
}

```

Appendix G

Water and Pressure sensor design code:

```

int Senpin1 = 6;
int Senpin2 = 7;
int R1 = 10000;
int R2 = 10000;
float Vo1 = 0.00;
float Vo2 = 0.00;
float Vo3 = 0.00;
float Vo4 = 0.00;
float Vw1=0.00;
float Vw2=0.00;
float Vw=0.00;
float Rw1, Rw2, Rw, Rt1, Rt2, Rt;

void setup()

```

```

{
  pinMode(Senpin1, OUTPUT); // set pin8 as output pin
  pinMode(Senpin2, OUTPUT); // set pin10 as output pin
  Serial.begin(9600);
}
void loop()
{
  float Rw1=0;
  float Rw2=0;
  float Rw=0;
  float Rt1=0;
  float Rt2=0;
  float Rt=0;
  { digitalWrite (Senpin1, HIGH);
    digitalWrite (Senpin2, LOW);
    delay(1000);
    int Samp1 = analogRead(A0);
    Vo1 = (5.0*Samp1)/1024.0;
    Rt1 = (Rw1+R2)*5.0/(Vo1);
    Rw1= Rt1-(R1+R2);
    int Samp2 = analogRead(A1);
    Vo2 = (Vo1*Samp2)/1024.0;
    Rw1=(R2*Vo1/Vo2)-R2;
    Vw1=Vo1-Vo2;
    Serial.print(" Vo1: "); Serial.print(Vo1); Serial.print(" Rw1: "); Serial.print(Rw1);
  Serial.print(" Vo2: ");
    Serial.print(Vo2); Serial.print(" Vw1: "); Serial.println(Vw1);
  }
  { digitalWrite (Senpin1, LOW);
    digitalWrite (Senpin2, HIGH);
    delay(1000);
    int Samp3 = analogRead(A1);
    Vo3 = (5.0*Samp3)/1024.0;
    int Rt2 = (Rw2+R1)*5.0/(Vo3);
    Rw2= Rt2-(R1+R2);
    int Samp4 = analogRead(A0);
    Vo4 = (Vo3*Samp4)/1024.0;
    Rw2=((R1*Vo3)/Vo4)-R1;
    Vw2=Vo3-Vo4;
    Serial.print(" Vo3: "); Serial.print(Vo3); Serial.print(" Rw2: "); Serial.print(Rw2);
  Serial.print(" Vo4: ");
    Serial.print(Vo2); Serial.print(" Vw2: "); Serial.println(Vw2);
  }
  Rw=(Rw1+Rw2)/2;
}

```

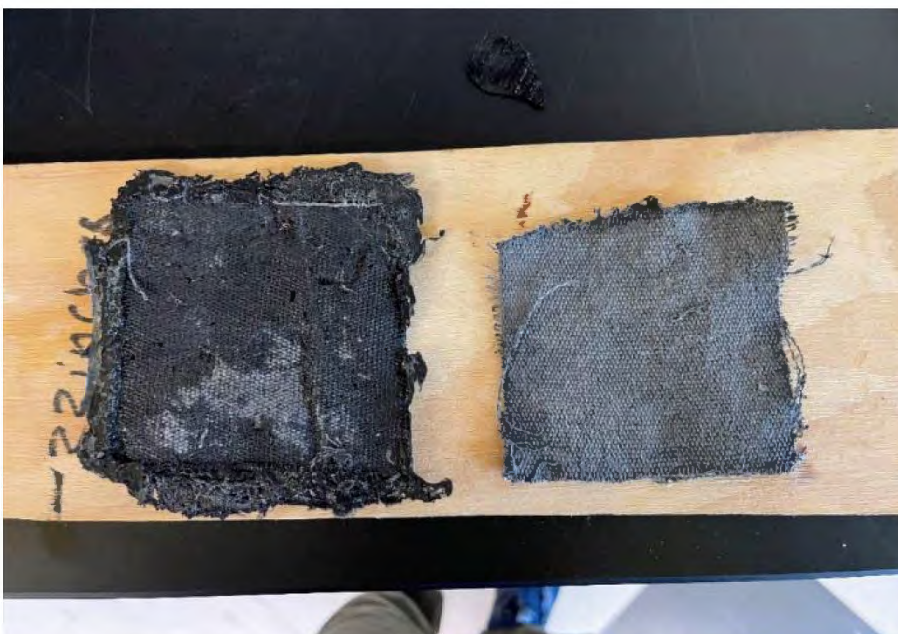
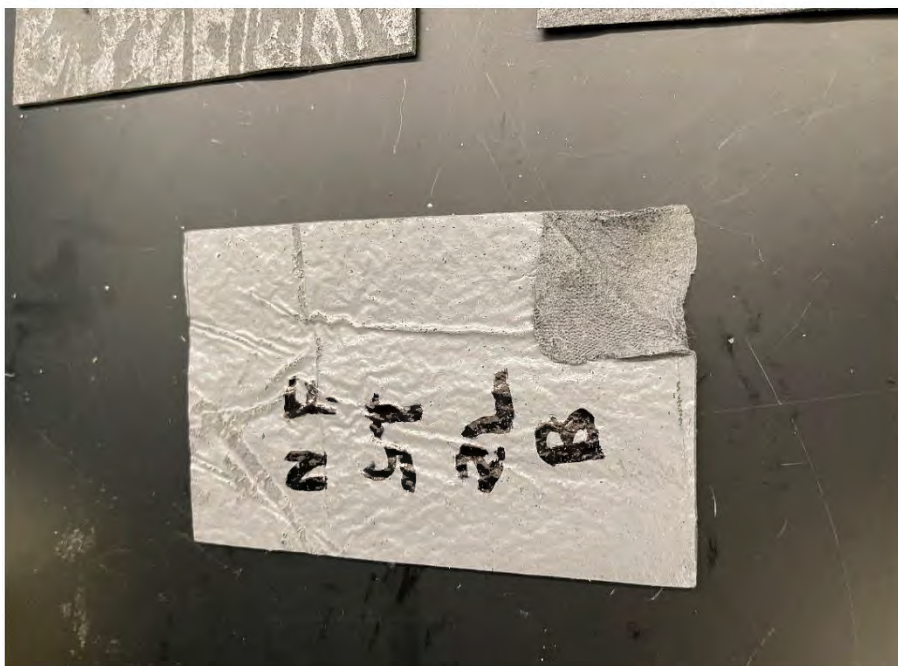
```
Vw=(Vw1+Vw2)/2;  
Serial.print(" Vw: "); Serial.print(Vw); Serial.print(" Rw: "); Serial.println(Rw);  
}
```

Appendix H

Experiment and sample testing images.

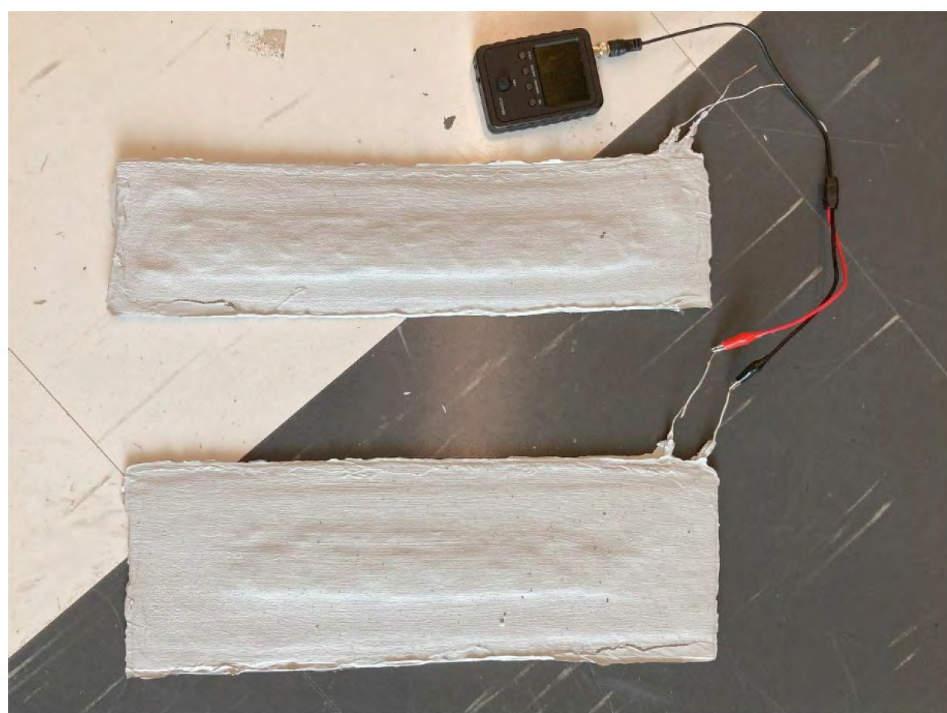
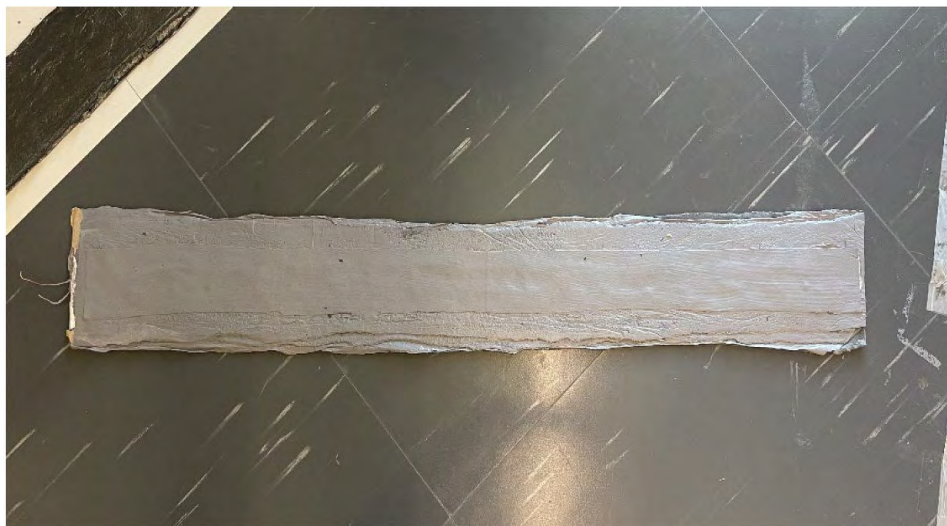


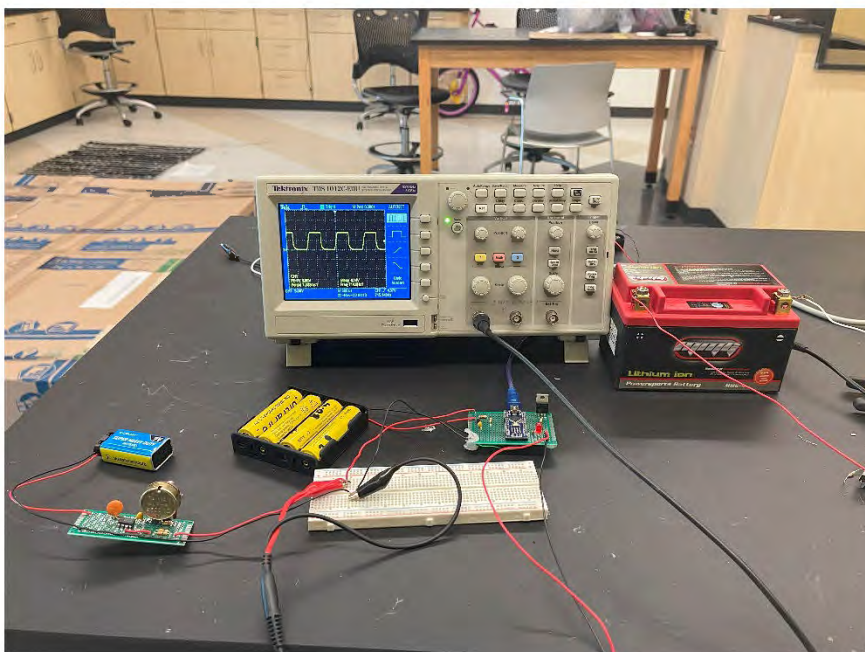
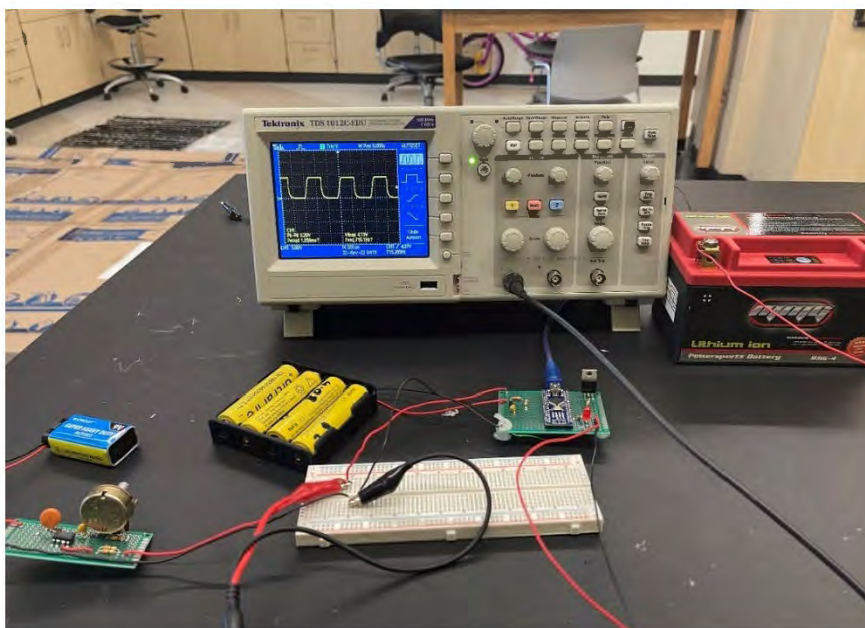


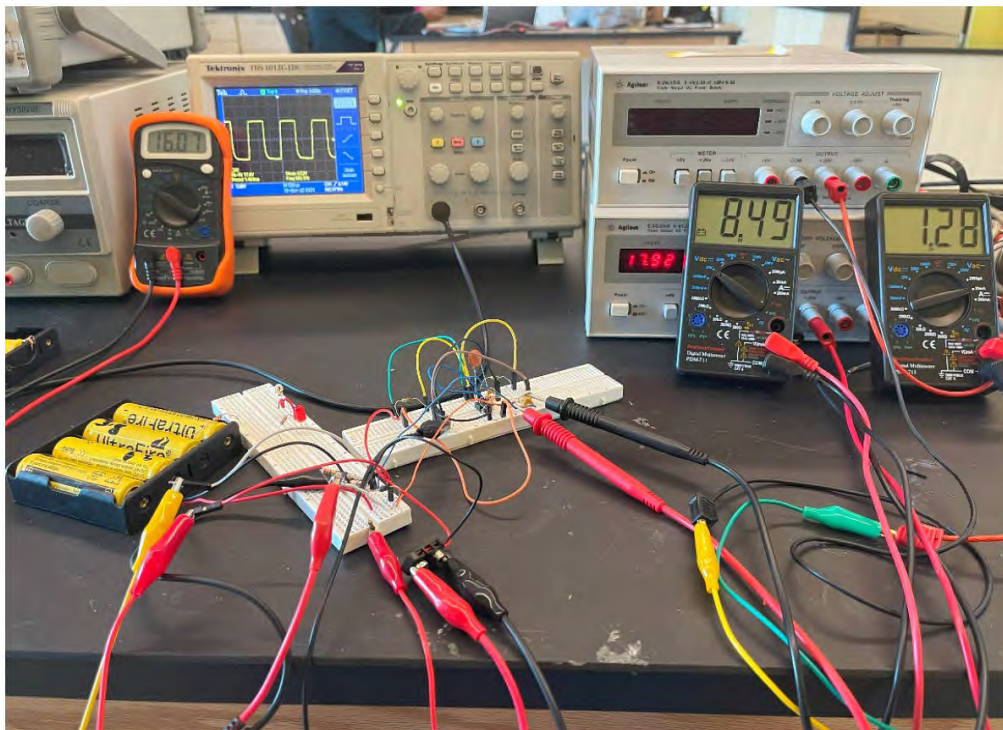
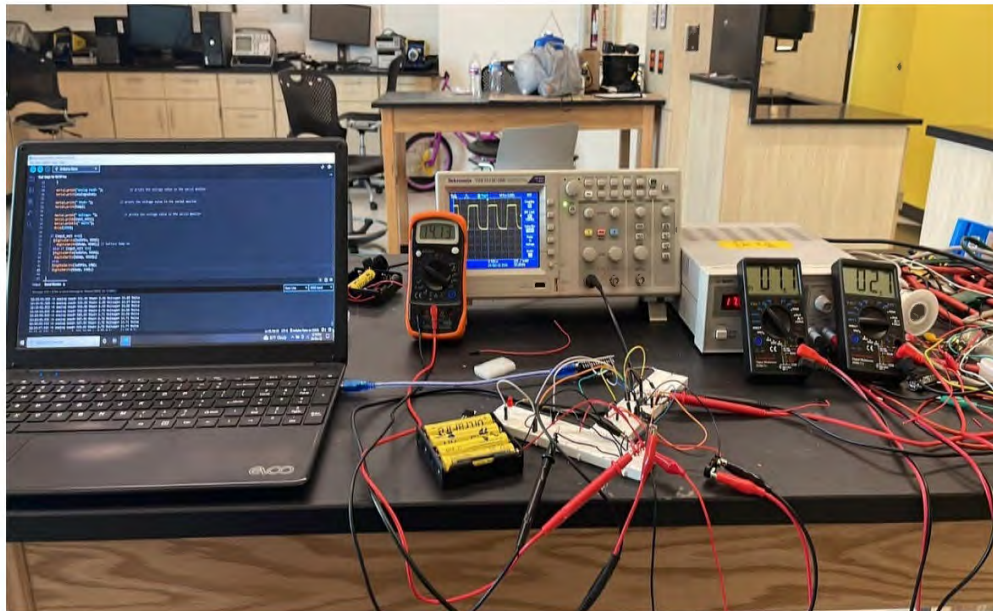












Appendix I

Matlab code:

```
% Parameters  
voltage1 = 50; % Average voltage for 7.5 ms
```

```

voltage2 = 0; % Voltage during delay (10 ms)
delay_ms = 10; % Delay duration in milliseconds

% Total time for each duration
total_time_sec = [1, 60, 30 * 60, 60 * 60];

% Initialize cell arrays to store time and voltage for each duration
time_data = cell(1, numel(total_time_sec));
voltage_data = cell(1, numel(total_time_sec));

% Generate voltage data for each duration
for i = 1:numel(total_time_sec)
    % Convert total_time_sec to milliseconds
    total_time_ms = total_time_sec(i) * 1000;

    % Calculate total time in milliseconds for one cycle
    total_time_ms_cycle = 7.5 + delay_ms;

    % Time vector for plotting
    time_data{i} = linspace(0, total_time_sec(i), total_time_ms+1);

    % Initialize voltage vector
    voltage_data{i} = zeros(1, total_time_ms+1);

    % Fill voltage vector based on the system behavior
    for t = 1:total_time_ms+1
        if mod(t, total_time_ms_cycle) <= 7.5
            voltage_data{i}(t) = voltage1;
        else
            voltage_data{i}(t) = voltage2;
        end
    end
end

% Plot voltage vs time for all durations in subplots
figure;

% Plot for 1 second
subplot(2, 2, 1);
plot(time_data{1}, voltage_data{1});
xlabel('Time (seconds)');
ylabel('Voltage');
title('Voltage vs Time (1 second)');
ylim([-5 55]); % Set y-axis limit based on voltage values
grid on;

```

```
% Plot for 1 minute
subplot(2, 2, 2);
plot(time_data{2}, voltage_data{2});
xlabel('Time (seconds)');
ylabel('Voltage');
title('Voltage vs Time (1 minute)');
ylim([-5 55]); % Set y-axis limit based on voltage values
grid on;

% Plot for 30 minutes
subplot(2, 2, 3);
plot(time_data{3}, voltage_data{3});
xlabel('Time (seconds)');
ylabel('Voltage');
title('Voltage vs Time (30 minutes)');
ylim([-5 55]); % Set y-axis limit based on voltage values
grid on;

% Plot for 1 hour
subplot(2, 2, 4);
plot(time_data{4}, voltage_data{4});
xlabel('Time (seconds)');
ylabel('Voltage');
title('Voltage vs Time (1 hour)');
ylim([-5 55]); % Set y-axis limit based on voltage values
grid on;
```

Appendix J

Etap Analysis data:

Bus Input Data

Bus					Load							
ID	kV	Sub-sys	Initial Voltage		Constant kVA		Constant Z		Constant I		Generic	
			% Mag	Ang	MW	Mvar	MW	Mvar	MW	Mvar	MW	Mvar
AC Bus 1	0.110	3	100.0	0.0								
AC Bus 2	0.110	4	100.0	0.0								
AC Bus 3	0.110	3	100.0	0.0								
AC Bus 4	0.110	4	100.0	0.0								
Bus9	0.100	1	110.0	0.0	0.001	0.000						
Bus15	0.100	2	110.0	0.0	0.002	0.000						
Total Number of Buses: 6					0.003	0.000	0.000	0.000	0.000	0.000	0.000	0.000

Generation Bus				Voltage		Generation			Mvar Limits	
ID	kV	Type	Sub-sys	% Mag	Angle	MW	Mvar	% PF	Max	Min
AC Bus 1	0.110	Swing	3	100.0	0.0					
AC Bus 2	0.110	Swing	4	100.0	0.0					
Bus9	0.100	Swing	1	110.0	0.0					
Bus15	0.100	Swing	2	110.0	0.0					
						0.000	0.000			

LOAD FLOW REPORT @ T = 60.000-

Bus		Voltage		Generation		Load		Load Flow				XFMR	
ID	kV	% Mag	Ang	MW	Mvar	MW	Mvar	ID	MW	Mvar	Amp	%PF	% Tap
AC Bus 1	0.110	134.016	0.0	0	0	0	0	AC Bus 3	0.000	0.000	0.0	100.0	
								Inverter 1	0.000	0.000	0.4	100.0	
AC Bus 2	0.110	128.171	0.0	0	0	0	0	AC Bus 4	0.000	0.000	0.0	100.0	
								Inverter 2	0.000	0.000	0.8	100.0	
AC Bus 3	0.110	134.016	0.0	0	0	0	0	AC Bus 1	0.000	0.000	0.0	100.0	
AC Bus 4	0.110	128.171	0.0	0	0	0	0	AC Bus 2	0.000	0.000	0.0	100.0	
Bus9	0.100	110.000	-8.5	0	0	0.001	0.000	1X SEGP 1	-0.001	0.000	6.0	100.0	
Bus15	0.100	110.000	-11.0	0	0	0.002	0.000	2X SEGP 2	-0.002	0.000	7.9	100.0	
1X SEGP 1	0.110	101.439	0.0	0.001	0.000	0	0	Bus9	0.001	0.000	6.0	98.9	
2X SEGP 2	0.110	102.310	0.0	0.002	0.000	0	0	Bus15	0.002	0.000	7.9	98.2	
Inverter 1	0.110	145.929	0.0	0	0	0	0	AC Bus 1	0.000	0.000	0.4	100.0	
Inverter 2	0.110	144.447	0.0	0	0	0	0	AC Bus 2	0.000	0.000	0.8	100.0	

* Indicates a voltage regulated bus (voltage controlled or swing type machine connected to it)

Indicates a bus with a load mismatch of more than 0.1 MVA

PHD RESEARCH OUTCOME & ACHIEVEMENTS

BLIND PEER REVIEW CONFERENCES	TYPE	STATUS
1. An Experimental Model and Test of a Novel Sustainable Energy Pad for Bike Lane Applications	ASEE 2022	Published
2. Design and Implementation of a Sustainable Energy Generating Pad for Lightweight Transportation	IEEE PES 2022	Published
3. Portable Solar-Powered Smart System for Reverse Osmosis Process of Drinkable Rainwater	IEEE PES 2022	Published
4. Impact Analysis of Lithium-ion Battery Storage System for Sustainable Energy Generating Pad Applications	IEEE PES IAS 2024	Published
5. Utilization of Road Infrastructure with a Hybrid of Solar PV and SEGP Energy for Drinking Water & eBike Charging Station.	IEEE PES IAS 2024	Published (received a best paper award)
6. Performance Analysis of Multi-Composite Layered Energy Harvesting from Thin-Film PZT with Smart Charging System.	IEEE PES IAS 2024	Published
7. Techno-Economical Evaluation of an Integrated EWeC Station Utilizing Road Infrastructure for Hybrid Energy, Drinking Water, and EV Charging Services.	IEEE PES IAS 2024	Published
8. Enhancing Reliability and Performance of Hybrid (PV and SEGP) Energy Island Microgrid Systems for Community.	IEEE PES IAS 2024	Published
PEER REVIEW JOURNALS	TYPE	STATUS
9. Innovation of Sustainable Energy Generating from Lightweight Vehicle Applications	Elsevier ECM	Published
10. Development of an Emulator of the Sustainable Energy Harvesting Pad System on a Bike Lane for Smart Charging of Lithium Batteries	Elsevier Micro-Electronic Engineering	Published
11. Techno-economic Evaluation of Hybrid Energy, Water, and Charging (EWC) Systems for Roadside Facilities	(TIA) IEEE Transaction	Invited, submitted, & Under Review
12. Exploring and Comparing Multicomposite Layers Thin-Film PZT as a Future Alternative Energy Source for Roadway Generation	(TIA) IEEE Transaction	Invited, submitted, & Under Review
13. Reliability & Performance Assessment of Grid-Tie Hybrid (PV and SEGP) Energy Microgrid Systems for Smart Cities	Elsevier Applied Energy	Invited, Deadline September 1, 2024
PATENTS/PCT	TYPE	STATUS
14. Technologies for energy-generating multilayer composite material for pad application in transportation systems.	WIPO	Published WO2023225474A1
15. Technologies for dual-stage charge collection and energy storage for alternative energy sources.	WIPO	Published WO2023225473A2
16. Sustainable Energy-Based Contactless Reverse Osmosis (CRO) by Low Energy Pump for Smart Portable Water Filtration System	Utility USPTO	Submitted - 04/11/2024 (US23/63458534)

CURRICULUM VITAE

Kazi Meharajul Kabir

e-mail: kkabir@pvamu.edu

<https://scholar.google.com/citations?user=FMgpJtkAAAAJ&hl=en>

PROFESSIONAL STATEMENT

A dynamic, versatile engineer and professional with 5 plus years of industrial experience in electrical substations, solar power plants, and power system software. Also, A thoughtful, ambitious researcher with 9.0 plus years of experience in research and development, design, quality improvement, electronic and sensor design, sustainable energy application development, new and novel ideas, prototype development, testing, and failure analysis, who is continuously trying to achieve the targeted goals.

EDUCATION

1. Ph.D. in Electrical Engineering, Prairie View A&M University, Texas, USA. [2024]
2. MS in Engineering (Electrical), Chittagong University of Engineering & Technology, Chittagong, Bangladesh. [2018]

JOB EXPERIENCE

1. Graduate Research Assistant at SMART Center, ECE, Prairie View A&M University, USA.
Responsibilities: Sustainable Energy Generating Pad for Bike Lane Applications funded by NSF Grant No: 2025641. [Fall 2021 to Present]
2. Power Engineer Intern at Optimization & AI Team, R&D, ETAP, Irvine, California, USA.
Responsibilities: Working on a 3MW BESS Pilot Project and Developing a BESS Analyzer and a Microgrid Optimizer. [May 2023 to Aug 2023]
3. Graduate Teaching Assistant at EECS, Texas A&M University-Kingsville, USA.
Responsibilities: Assignment Grading, Lab Instructor, Backup Lecture. [Jan to Aug 2021]
4. Project Engineer, NOBO Engineering, Chittagong, Bangladesh.
Responsibilities: Solar System Project Design, Planning, Development, Installation, and After-Sell Service. [Feb 2017 to May 2020]
5. Executive Electrical, KDS Logistic Limited, Chittagong, Bangladesh.
Responsibilities: Sub-station and Electrical Maintenance, ELD. [Aug 2015 to Jan 2017]

RESEARCH EXPERIENCE

1. M.Sc. Thesis - Design and Implementation of Solar System for Production of Potable Water in Coastal Region.
2. B.Sc. Thesis - Modeling & Simulation of Grid Connected Hybrid Power System with Photovoltaic, Wind, Battery, and Diesel Generator for Patenga, Chittagong, Bangladesh.

PATENT

1. S. Binzaid and K. M. Kabir, " Technologies for Energy Generating Multilayer Composite Material for PAD Application in Transportation Systems," WIPO- WO2023225474A1, Nov 23, 2023.
2. S. Binzaid and K. M. Kabir, " Technologies for Dual-Stage Charge Collection and Energy Storage for Alternative Energy Sources," WIPO- WO2023225473A2, Nov 23, 2023.

3. S. Binzaid and K. M. Kabir, "Sustainable Energy-Based Contactless Reverse Osmosis (CRO) by Low Energy Pump for Smart Portable Water Filtration System," USPTO provisional no- US23/63458534, Apr 11, 2023.

RESEARCH PUBLICATION

Journal Articles

1. Kabir, K. M., Matin, M. A., Mazumder, S., Chowdhury, M.S.U., Forhad, M.W.U. & Mallick, A. (2020). "Design and Analysis of a Grid-Connected Hybrid Power System with Constant Supply for Patenga, Bangladesh. ." *Cogent Engineering-Taylor & Francis*, 7(1), 1762524, pp. 1-20.2020.
2. Kabir, K. M., & Matin Bhuiyan, M. A. (2017, July). Design & simulation of hydrogen-based hybrid green power system using seawater for Cox's Bazar. *Cogent Engineering – Taylor & Francis*, 4(1),1347029. pp. 1-14.

Conference Proceedings

3. Kabir, K.M. & Binzaid, S., (2024, February), Performance Analysis of Multi-Composite Layered Energy Harvesting from Thin-Film PZT with Smart Charging System, in IEEE Texas Power and Energy Conference (TPEC) 2024, pp. 1-5.
4. Kabir, K.M. & Binzaid, S., (2024, February), Techno-Economical Evaluation of an Integrated EWeCStation Utilizing Road Infrastructure for Hybrid Energy, Drinking Water, and EV Charging Services, in IEEE Texas Power and Energy Conference (TPEC) 2024, pp. 1-5.
5. Kabir, K.M. & Binzaid, S., (2024, January), Impact Analysis of Lithium-ion Battery Storage System for Sustainable Energy Generating Pad Applications, in IEEE Third International Conference on Power, Control and Computing Technologies (ICPC2T) 2024, pp.1-5.
6. Binzaid, S. and K. M. Kabir, (2024, January), Utilization of Road Infrastructure with a Hybrid of Solar PV and SEGP Energy for Drinking Water and eBike Charging Station, in IEEE Third International Conference on Power, Control and Computing Technologies (ICPC2T) 2024, Raipur, India, Jan. 2024, pp.1-5.
7. Kabir, K.M., Binzaid, S., & Attia, J. O., (2022, October), Portable Solar-Powered Smart System for Reverse Osmosis Process of Drinkable Rainwater, IEEE Global Energy Conference 2022, pp. 1-5, Turkey, IEEE.

PROJECT

1. Design and Implementation of Sustainable Energy Generating Pad for Bike Lane Applications.
2. Innovation of A Novel Contactless Reverse Osmosis (CRO) Pump in the Application of a Smart Water Filtration System.
3. A Solar Powered Brackish Water Purification System for Coastal Region in Bangladesh.

ACHIEVEMENT

1. Best Paper Award at Third International Conference on Power, Control and Computing Technologies (ICPC2T) 2024.
2. Presented an oral and poster presentation at the NSF S&CC PI Meeting 2024.
3. Southwest I-Corps Program Certification by National Science Foundation
4. Dean Award Scholarship 2021-2024 at Prairie View A&M University.
5. Dean Award Scholarship 2020-2021 at Texas A&M University-Kingsville.